Nonlocal Dynamics in Nonlinear Biomolecular and Optical Systems

Larsen, Peter Ulrik Vingaard; Sørensen, Mads Peter

Publication date:
2006

Document Version
Publisher's PDF, also known as Version of record

Nonlocal Dynamics in Nonlinear Biomolecular and Optical Systems

Peter Vingaard Larsen

Ph.D. Thesis - 2006
Department of Mathematics
Technical University of Denmark

Title of Thesis:

Nonlocal Dynamics in Nonlinear Biomolecular and Optical Systems

Ph.D. Student:

Peter Vingaard Larsen
Department of Mathematics
Matematiktorvet, bldg. 303
Technical University of Denmark
DK-2800 Lyngby, Denmark
E-mail: P.V.Larsen@mat.dtu.dk

Supervisor:

Associate Professor, Ph.D., Mads Peter Sørensen
Department of Mathematics
Matematiktorvet, bldg. 303
Technical University of Denmark
DK-2800 Lyngby, Denmark

Co-supervisors:

Professor Peter Leth Christiansen
Department of Physics
Bldg. 307–309–312
Technical University of Denmark
DK-2800 Lyngby, Denmark

Associate Professor Ole Bang
COM • DTU
Ørsteds Plads, bldg. 345v
Technical University of Denmark
DK-2800 Lyngby, Denmark

Preface

This thesis is submitted in partial fulfillment of the requirements for obtaining the Ph.D.-degree. The work has been carried out in the period from October 2002 to November 2005, at The Department of Informatics and Mathematical Modelling, The Technical University of Denmark (Oct. 2002 to Feb. 2004) and the Department of Mathematics, The Technical University of Denmark (Feb. 2004 to Nov. 2005), with a visit to the Australian National University from October 2004 to March 2005. The work has been under the supervision of Associate Professor Mads Peter Sørensen (Department of Mathematics, DTU), Professor Peter Leth Christiansen (Department of Physics, DTU), and Associate Professor Ole Bang, (Department of Communications, Optics & Materials, COM•DTU). The Ph.D.-study was financially supported by The Technical University of Denmark and the support is most gratefully acknowledged.

Acknowledgments

First of all I would like to express my gratitude to my supervisors Associate Professor Mads Peter Sørensen, Professor Peter Leth Christiansen and Associate Professor Ole Bang. Then sincere thanks to Professor Wieslaw Z. Krolíkowski, Laser Physics Centre at the Australian National University for the hospitality and supervision during my visit there.

Also visitors to DTU have been very helpful to me, and I especially thank Professor Yuri B. Gaididei, University of Kiev, Russia and Associate Professor Juan F. Archilla, University of Seville, Spain, together with Professor Stefano Trillo, University of Ferrara and National Institute for Physics of the Matter for their collaboration.

Also Dr. Sergei F. Mingaleev, Univeristy of Karlsruhe and Dr. Darran Edmundson, ANU Supercomputer Facility for their help and advice. Associate Professor Niels Christian Albertsen, Informatics and Mathematical Modelling, DTU, Associate Professor Tom Høholdt and Professor Morten Brøns, Department of Mathematics, DTU, are acknowledged for their kind organizing skills.

Thanks to my brothers David and Philip for their help with some figures and proofreading.

Dedicated to my grandmother, Ellen Thorsen.

Peter Vingaard Larsen
January 2006

Summary

The notion of *nonlocality* in the description of physical systems is receiving an increasing amount of interest, and with good reason. Nonlocality implies that in order to describe the physical properties of a system at a given point, one cannot simply look at the values of the variables and parameters at that very point, but it is necessary to use inputs from the rest of the domain in order to understand the situation correctly. Nonlocality has been used for a broad range of problems, from molecular systems to liquid crystals. In the present work, two quite different physical systems — a model of a DNA molecule and one of a nonlinear optical crystal — are studied within a nonlocal context.

In living cells, the immensely important DNA molecule is responsible for protein processing and cell replication. Both effects require an opening of the double-stranded molecule and to facilitate this, energy localization is believed to play an important role. It is known that by introducing inhomogeneities along a model molecular chain — which could simulate the action of enzymes — localization of vibrational energy can occur and thereby facilitate DNA opening. In this work we augment a renowned existing model to include both long range dipole-dipole interaction and geometry. The geometrical features cannot be appreciated without nonlocality. With an intrinsically homogeneous molecule we are then able to observe energy localization originating only from geometrical variables through a nonlocal interaction.

Nonlinear optics is a young (the laser was invented not half a century ago), but immensely progressive fields of physics with applications to ultra-fast data processing and transmissions. Already today, fiber-optical cables are used in conventional communication systems. All-optical signal processing is not yet possible, but is a main research topic as localized quantities can act as carriers of information. One possible realization of such an entity is the so-called *X-wave*. Nonlocality can be used to describe X-waves and like phenomena and particularly to inspire a search for X-waves in materials with anomalous dispersion as well, which is not previously predicted. Numerical examples of these are suggested in the present work.

Resumé (In Danish)

Begrebet *ikke-lokalitet* nyder større og større interesse indenfor modelleringen af fysiske systemer — og med god grund. At en model er ikke-lokal betyder at for at kunne beskrive dens fysiske egenskaber i et givet punkt korrekt er det ikke tilstrækkeligt blot at betragte omstændighederne i netop dette punkt, tværtimod må en større del af modellens domæne tages i betragtning for at opnå en nøjagtig formulering. Denne idé har været anvendt i en lang række problemstillinger, fra molekylære systemer til flydende krystaller. I nærværende arbejde betragtes to ganske forskellige fysiske systemer — en model af et DNA-molekyle og en af en ikke-lineær optisk krystal — i en ikke-lokal sammenhæng.

I levende celler er det umådeligt vigtige DNA-molekyle ansvarlig for fremstilling af proteiner og celledeling. Begge disse aktiviteter kræver en åbning af molekylets to strenge og for at muliggøre dette antages det at energilokalisering spiller en væsentlig rolle. Det er velkendt at introducerede inhomogeniteter på en model af molekyl-kæden — disse kan tænkes at simulere effekten af enzymer — kan lokalisere vibrationsenergi og dermed muliggøre åbning af DNA. I dette arbejde har vi udvidet en anerkendt model til at inkludere både dipol-dipol-vekselvirkninger og geometriske forhold. Disse geometrieffekter kan ikke betragtes udenfor en ikke-lokal beskrivelse. Vi er dermed i stand til at observere energilokalisering i et grundlæggende homogent molekyle, foranlediget af en ikke-lokal beskrivelse af geometriske effekter.

Ikke-lineær optik er et nyt (det er ikke et halvt århundrede siden laseren blev opfundet), men

meget aktivt område af fysikken, med anvendelser til ultrahurtig databehandling og -transmission. Allerede i dag anvendes fiberoptiske kabler til konventionelle kommunikationssystemer. Signalbehandling udelukkende på basis af optiske processer er endnu ikke en realitet, men er et hovedområde for forskningen idet lokaliserede optiske enheder kan benyttes som informationsbærere. En mulig sådan lokaliseret størrelse er en såkaldt *X-bølge*. Ikke-lokalitet kan benyttes til at beskrive X-bølger og lignende fænomener og specielt give anledning til at søge X-lignende strukturer i materialer med anormal dispersion, hvilket ikke tidligere er observeret. I nærværende arbejde giver vi numeriske eksempler på disse.

Contents

Introductory remarks

In the description of complex physical processes, simple *linear* models are often insufficient. Linear effects simply do not fully possess the power to provide a satisfactory description of important processes in optical systems, biological systems, solid state physics, superconducting Josephson arrays, hydrodynamics, and many other subjects.

The field of nonlinear science includes *chaos theory*. One (of many) characteristics of such a system is that its status is critically depending on the its initial conditions. In contrast to linear systems, where a small change in the initial conditions results in a small change of the outcome, the behaviour of a chaotic system is unpredictable, even for small initial perturbations. A well-known metaphor is the butterfly flapping its wings in Brazil, causing a hurricane in the Mexican Gulf.

Based on this description, one may think that nonlinearity is about disorder and unpredictability. In fact, the opposite is often the case and a second branch of nonlinear research is devoted to the study of localized structures. Many linear systems are diffusive and lose information as time, space or both evolve. But inclusion of nonlinearity may counteract this effect and stable, localized structures may occur! The first example of such a *soliton* is the "wave of translation" discovered by John Scott Russell in 1834. This young Scotsman observed a travelling wave of water of about a foot in height, undistorted in shape for several miles. Such a behavior is not supported by linear equations, under which an initial wave pulse will spread out, but nonlinearity can provide a focusing effect able to balance the linear diffusion.

In this way nonlinearity has proven useful — and necessary — to properly describe various features of physical systems. Another aspect of physical modeling is a system's degree of *nonlocality*. A local system has the property that the state at one given point can be determined solely on the value of its variables and parameters at that very point. A nonlocal system, however, requires information from other points of the system to determine its value at a given point. Just as nonlinear models in general are more complex than linear, nonlocal models are in essence more complex than local. But in return they are able to give superior predictions of the system dynamics, just as nonlinearity better describe many real world phenomena.

In the present work, two different nonlocal physical systems are considered and this thesis is divided into two parts to reflect that. In Part I, energy localization in biomolecules is discussed with a nonlocal model. This is a discrete model with only one unknown, depending on one spatial and one temporal variable. Part II is about localized structures in quadratic optical materials. This is a continuous 2+1D model with 2 unknown fields and thus its description is somewhat more complicated than the previous topic.

Part I

Energy Localization in Biomolecules

1

Introduction to the DNA molecule

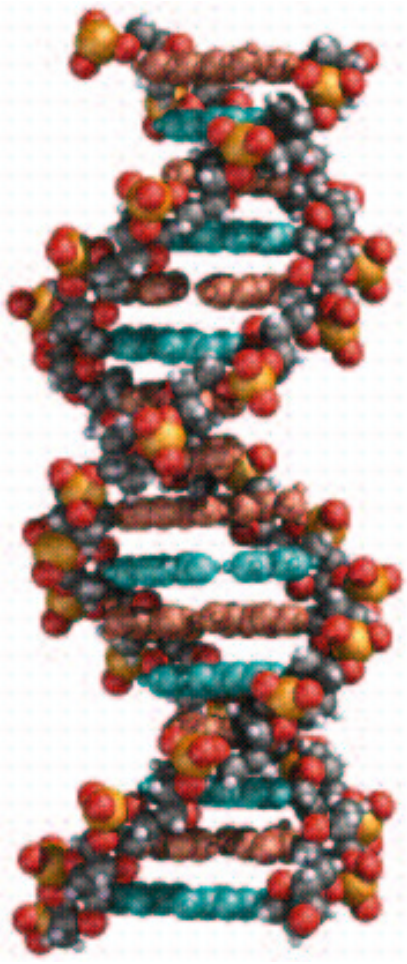

Figure 1.1: *The DNA molecule.*

The importance of the DeoxyriboNucleic Acid, better known by its acronym DNA, has been emphasized over the last few years by advances in drug design, an increasing interest in genetically modified organisms, and the humane genome project.

The DNA molecule contains all information about the structure of the body's cells and the "building blocks" to produce proteins. It is basically made up of succeeding units called *nucleotides*, of which there are only four: *adenosine* (A) and *guanine* (G) (the *purines*), and *cytosine* (C) and *thymine* (T) (the *pyrimidines*), all with a common sugar-phosphate group which connects to form the *backbone* of the molecular chain.

DNA has a remarkable double-strand helicoidal structure, discovery by Watson end Crick in 1953 [1] (earning them a Nobel prize in 1962), and is depicted in Fig. 1.1. The bases binds to each other, but due to their chemical structure, the base A can only bind to T, and C only to G. The former pair through a double hydrogen bond; the latter by a triple. See Figs. 1.2 and 1.3. There are about 3 billion base pairs in human DNA. With a separating distance of about 3.4 Å, the approximate length is about a meter! This is remarkable as it is contained in each microscopic cell core.

Because the bases are hydrophobic and the sugar-phosphate backbone is hydrophile, the strands coil to form a characteristic helicoidal shape with the help of dipole-dipole interaction. This "twisted ladder" shape, with "steps" made of *base pairs* and "railings" made of the sugar-phosphate back-bone, is the com-

mon DNA shape, but it should be noted that others occur as well. The base pair sequence — the *primary* structure — is supplemented by the twist of the DNA helix — the *secondary* structure — as well as the *tertiary* structure: The curling and wrinkling of the DNA double strand. It is noted, that it is becoming increasingly apparent that the base pair sequence alone does not explain its complex functionality sufficiently, see Refs. [2, 3, 4, 5, 6].

DNA Denaturation The DNA molecule contains all the required information on how to make *amino acids* and *proteins*, which are both single-stranded molecules also made of the bases A, T, C, and G. The body contains 20 different amino acids and these connect to form proteins (typically several hundreds are needed). The amino acids are characterized by a segment of 3 nucleotide pairs, called a *codon*. The term *gene* denotes a segment of the DNA chain that corresponds to a protein. This genetic information is copied by the RNA (ribonucleic acid) molecule (and an enzyme, RNA-polymerase), before it is transported to relevant areas of the cell. The copying is called *transcription* and to facilitate this the two base pair strands must open. This opening process is called *denaturation* and is the focus of the present work. Denaturation usually occurs in localized areas called *bubbles* of about 20 base pairs [7, 8, 9, 10], around which the two strands are twisted more.

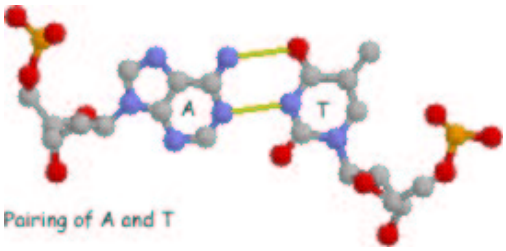

Figure 1.2: *The AT base pair.*

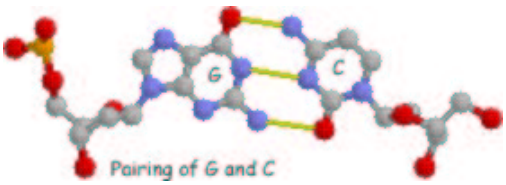

Figure 1.3: *The GC base pair.*

Denaturation obviously requires the breaking of hydrogen bonds, a process that requires energy to take place. But for the denaturation *no chemical energy* is consumed — no ATP molecules are spent. Some energy is present due to thermal fluctuations, but for the base pairs to open solely on thermal energy the temperature has to be much higher than body temperature [9].

Thus it is clear that additional effects must take place.

Modeling DNA *Enzymes* (which are also proteins) are important for numerous bodily functions and do beyond any doubt play a role in DNA denaturation. A typical metaphor is an enzyme the shape of a key, which opens the otherwise locked DNA strands, but this is obviously not a scientifically satisfying explanation. In common DNA models, the effects of enzymes have been modeled by introducing *inhomogeneities* or impurities in the chain structure. There are different ways to introduce these inhomogeneities. For instance, Refs. [11, 12, 13] have changed the mass at a given chain site (or multiple chain sites), whereas Refs. [14, 13] have introduced changes in the coupling between neighboring molecular sites. Both of these are meant to reflect the attachment of an enzyme to the DNA chain. Also, difference in the coupling between the two strands at various sites have been considered [15, 16, 17, 18]. This reflects the fact that different base pairs are bonded by different strengths: the AT base pair connects through 2 hydrogen bonds, whereas the CG base pair has 3 (see Figs. 1.2 and 1.3). Inhomogeneities originating from different inter-strand coupling may describe the different number of hydrogen bonds between the two strands. It has to some extent been experimentally verified that denaturation occurs at AT-rich sections of the DNA molecule [19, 20, 21, 22, 23], but recent work [24] also suggests that other mechanisms are involved. Also, conformational defects have been considered [25].

Furthermore, nonlinear excitations such as *solitons*, *discrete breathers*, or *intrinsic localized modes* have been drawing increasing attention over recent years and are widely believed to be responsible for several effects in molecular chains, such as charge and thermal conductivity, energy transfer and localization, etc. (see reviews in [4, 5, 26, 27, 28, 29], e.g.). In a combined effect, impurities have been shown to act as filters governing the progression of incoming excitations. An excitation travelling along an otherwise homogeneous molecular chain may exhibit both reflection, trapping and transmission from the interaction with the inhomogeneity [11, 12, 13, 14, 15, 25]. Similar effects have been observed through collisions between moving discrete breathers, thus [12, 30, 31, 32] showed how stationary large amplitude discrete breathers, on the average, absorb energy from colliding breathers of smaller amplitude. Thereby a large amplitude breather may play a role similar to that of an impurity [11].

In DNA models, an "excitation" is usually a localized increase of vibrational energy, as thermal fluctuations are always present at physiological temperatures. In this way, trapping of a moving excitation represents an local increase in energy, which may lead to the onset of denaturation. In biological environments, thermal fluctuations are always present and have been considered in Refs. [9, 22, 23, 33, 34, 35, 36, 37, 38, 39, 40, 41], e.g. In these references it was shown that solitons or discrete breathers can be generated from or exist among random thermal fluctuations.

In initial works on molecular chains, the geometrical features of the biopolymer chain were essentially neglected, but recently both long-range dipole-dipole interaction [42, 43], helicity [10, 44] and curvature [14, 45, 46, 47] have been included (as well as combinations of some of these effects [48, 49, 50, 51, 52]). It has been shown that chain curvature induces effects similar to those of impurities [45, 46, 48, 47].

The long-range dipole-dipole effects were mostly considered as parallel, which is not the normal case in biological environment. The DNA chain will temporarily uncurl in relation with opening, but this is a local and quick behavior; the molecule will wind up in itself again. Some special uncurled DNA chains may be prepared in the laboratory.

The functionality of DNA — and proteins in general — is not only determined by the base pair sequence (its primary structure), but also but the shape of the molecule [2, 3]. Therefore, special attention has been paid to models of these biological macromolecules [12, 14, 15, 26, 27, 33, 34, 35, 40, 53, 54]. A widely used model was presented by Peyrard and Bishop [55] in the context of statistical mechanics, where the solutions are shown to possess a energy localization, which is viewed as a precursor for thermal denaturation.

Aim of the present work The aim of the present work is to study the interplay between chain geometry and long-range interaction in an augmented Peyrard-Bishop model. We do this with a model describing two kinds of geometrical effects — a dipole *twist*, corresponding to the chain helicity, and chain *curvature*. This is done for two different chain geometries and two different expressions for the dipole-dipole interaction. The first one of these is very simple, but it is still capable of showing how a new mechanism for energy accumulation in the system — *funneling* — may be provided by the geometry of the chain. We study the effect using an attractive long-range interaction, and it turns out that the particular shape of the bend makes no qualitative difference. As initial conditions we use discrete breathers as well as randomly distributed fluctuations, simulating the effect of random thermal fluctuations.

Furthermore, we consider a realistic dipole-dipole long-range interaction with physically reasonable parameters, and we show how both chain curvature and twist can initiate bubble generation in the DNA molecule in two different chain configurations.

2

The augmented Peyrard-Bishop model for DNA

Biomolecules are often modeled as a lattice with point masses connected with some interaction. Standard proteins are readily described by a 1D lattice, but the more complex DNA molecule consists of two molecular strands connected. As we shall see, the renowned Peyrard-Bishop model [55] elegantly reduces the two-strand system to a single variable.

2.1 Model assumptions and terms

To be able to give a mathematically fairly straight-forward description of the DNA molecule, certain assumptions are made:

- The chain is assumed to be rigid and inextensible, so that the chain shape is fixed with constant distance, l, between base pairs. Thus no longitudinal motion is considered.
- We do not distinguish between the two sets of base pairs (*i.e.,* the AT and the GC pairs), but assume all base pairs and their bonds are identical, with masses M.
- We assume identical coupling between the strands (even though the extra H-bond in GC pair amounts to a 6 times higher value [14]).
- We assume that the DNA molecule is isolated from external interactions.

The dynamical variables of the model is the motion of the individual base pairs on each of the two strands. At the nth base pair site, these are denoted V_n and W_n, respectively[1], see Fig. 2.1. Note that the sign convention of V_n and W_n are opposite.

[1]The notation is somewhat confusing here, as V is used both for a distance and potentials, but the potentials all have a superscript, e.g. V_n^{Morse}

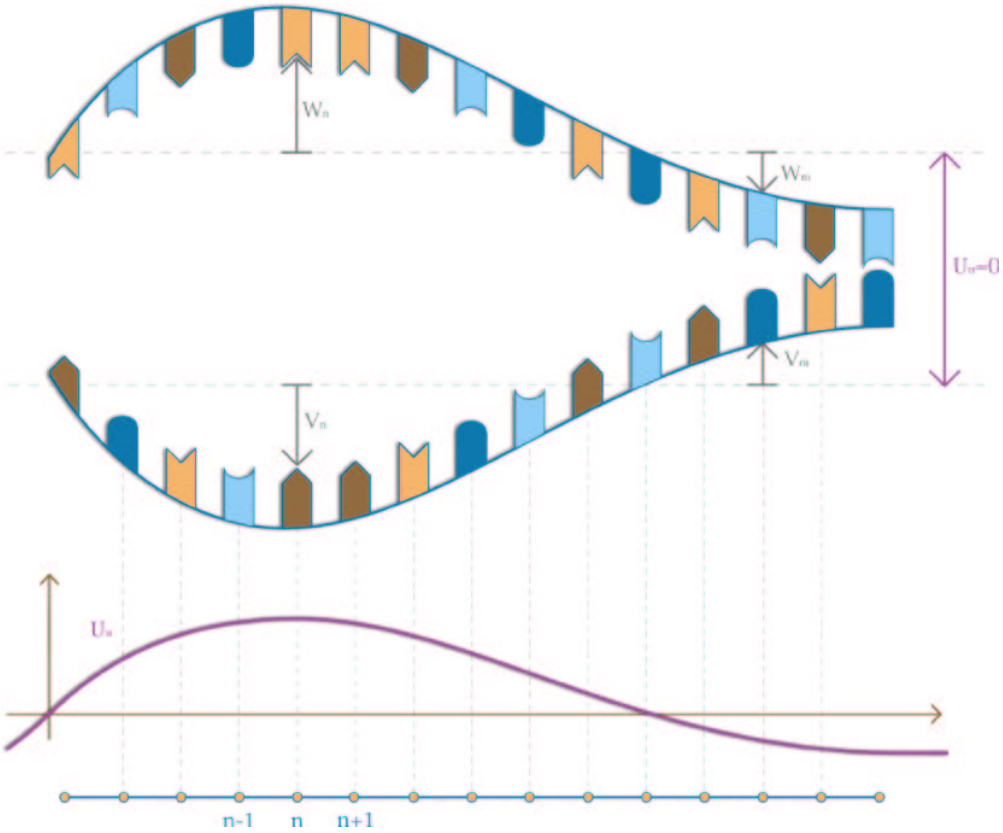

Figure 2.1: *The model DNA chain. Here, the chain is planar and the transformation from two to one variable is hinted.*

2.1.1 The Hamiltonian terms

The Hamiltonian of this system consists of a number of contributions, which will be described below.

Kinetic energy, T_n First, the nucleotides possess a kinetic energy giving for each base pair the contribution T_n:

$$T_n = \frac{M}{2}\left(\dot{V}_n^2 + \dot{W}_n^2\right), \tag{2.1}$$

with the dot denoting differentiation with respect to time. Since we restrict ourselves to exclude longitudinal motion, the kinetic energy presented in (2.1) only represents motion in the transverse dimension, between the two strands.

The mass, M, is a constant in our setting.

Stacking energy, V_n^{S} Even without longitudinal motion, the base pairs are connected to their neighbors; this is what is referred to as the stacking or the *coupling* potential. At base pair site n, it is given by

$$V_n^{\mathrm{S}} = \frac{\overline{C}}{2}\left[(V_n - V_{n-1})^2 + (W_n - W_{n-1})^2\right], \tag{2.2}$$

where we do not need to distinguish between interaction to the left neighbor and the right one. Note how the stacking potential acts as a spring between individual nucleotides on separated strands of

the molecule.

The coupling constant, $\overline{C}$, is constant in our setting, and we note that an overline indicates an unscaled, physical quantity.

Morse potential, V_n^{Morse} Atomic interaction is often described by the Morse potential (2.3), and this has also been employed in DNA dynamics as early as 1984 [56, 57]. It reads

$$V_n^{\text{Morse}} = D\left[\exp\left\{-\frac{\alpha}{\sqrt{2}}\left(W_n - V_n\right)\right\} - 1\right]^2, \tag{2.3}$$

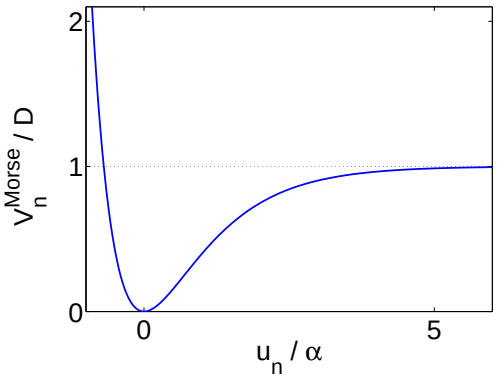

Figure 2.2: *The Morse potential, Eq. (2.3).*

where D and α are *depth* and *width* parameters, respectively. The Morse potential thus gives a recognized description of diatomic interaction, as it both models the hydrogen bond attraction for larger particle separation and a strong repulsion when the particles get closer (when this is the case, $W_n < 0$ and $V_n > 0$ (see Fig. 2.1), so the exponential term grows fast). The Morse potential is depicted in Fig. 2.2.

These features of the potential are important, but one obtains similar a behavior using e.g., the Lennard-Jones potential (2.4) to model the inter-strand on-site dynamics.

$$V_n^{\text{L-J}} = A\left[\left(\frac{B}{W_n - V_n}\right)^{12} - \left(\frac{B}{W_n - V_n}\right)^{6}\right], \tag{2.4}$$

The use of a nonlinear potential is crucial for the effects investigated here. The plateau of the Morse and Lennard-Jones potentials allows for the breaking of the hydrogen bonds in the molecule to be modeled. This is not the case for the harmonic oscillator.

These three terms, the kinetic energy, the stacking potential and the Morse potential represent the celebrated Peyrard-Bishop model of DNA dynamics [55].

We, however, add another feature to the model:

Long-range interaction, V_n^{LRI} Last, but certainly not the least, we have the long-range interaction (LRI) — which we also refer to as the *nonlocality* — described in Eqn. (2.5)

$$V_{nm}^{\text{LRI}} = \frac{1}{2}\sum_{m\neq n} \overline{J}_{nm}\left(W_n - V_n\right)\left(W_m - V_m\right) \tag{2.5}$$

This long-range term models the interaction between the dipole moment generated at the nth site and the dipole generated at the mth site. This dipole-dipole interaction is the crux of the present study. It represents the *nonlocality* of the model, because its contribution to the motion at site n is affected by the motion at *all* sites in the model chain. Notice that the term $n = m$ is excluded from the summation; this is simply because a dipole does not interfere with itself. The prefactor $\frac{1}{2}$ makes sure that the interaction between the dipoles at site n and m is only counted once.

The strength of a dipole is governed by the distance between charges, which is included through the $(W_{n,m} - V_{n,m})$ factors. The J_{nm} coefficient covers a dependence on the distance between the

nth and the mth charge. Basic electrostatics (e.g., [58]) tells us that this is an inverse cubic dependence.

Because of our assumption of a rigid chain the LRI is the *only* way the geometry of the model molecule becomes important! This aspect will be elaborated further in Sec. 3.2. The converse — that the LRI only becomes important through the inclusion of geometry — is not true. Nevertheless, due to the inverse cubic distance dependence of the LRI the dipole-dipole interaction is very small except for sites very close to each other. A curved model chain implies that the distance between given sites of the model chain can decrease, which in turns greatly amplifies the LRI strength. This effect is not restricted to rigid chains, but is also found in semi-flexible polymers [45].

In this work, two different expressions for the dipole-dipole interaction is considered. First, we consider a very crude approximation, which will give us some insight on a simplified chain geometry. Then the model is refined, both by a physically more reasonable geometry as well as a proper expression for the dipole moments.

To summarize, we have the Hamiltonian (2.6) for an infinite chain of our augmented Peyrard-Bishop (PB) model:

$$\overline{H} = \sum_n \overline{\mathcal{H}}_n = \sum_n \left\{ T_n + V_n^{\mathrm{S}} + V_n^{Morse} + V_n^{LRI} \right\}, \tag{2.6}$$

with the contributions defined in Eqs. (2.1)–(2.5) and with the *Hamiltonian density*, $\overline{\mathcal{H}}_n$, which gives the energy content at a given site.

Refining the model

The Peyrard-Bishop Hamiltonian (2.6) is not easy to attack as it is presented so far. Not only does it contain 2 independent variables, but they are also coupled. It turns out that the model is significantly simplified by the following change of variables (also done by Peyrard and Bishop [55]):

$$S_n = \frac{W_n + V_n}{\sqrt{2}} \quad \text{and} \quad U_n = \frac{W_n - V_n}{\sqrt{2}}. \tag{2.7}$$

With this, one immediately sees that the Morse potential only appears in the equation for U_n (see [59, 60] for details). The new variables S_n and U_n describe the Hamiltonian in two uncoupled equations, in-phase and out-of-phase motions, respectively. In relation to DNA denaturation, the in-phase motions are not interesting, as these do not change the distance between the DNA strands. Therefore, we can restrict ourselves to consider only the U_n variable, which quantifies the *deviation from the equilibrium distance.*

A negative U_n indicates that the nucleotide bases are closer to each other than normally and vice versa for a positive U_n, see Fig. 2.1. We have thus reduced the original 2D problem to a 1D one.

Our new Hamiltonian density becomes for an infinite chain:

$$\overline{\mathcal{H}}_n = \Big\{ \frac{M}{2}\dot{U}_n^2 + \frac{\overline{C}}{2}\left(U_n - U_{n-1}\right)^2 + D\left(e^{-\alpha U_n} - 1\right)^2 + \frac{1}{2}\sum_{m \neq n} \overline{J}_{nm} U_n U_m \Big\}, \tag{2.8}$$

Scalings To obtain a dimensionless Hamiltonian, we introduce the scalings

$$u_n = \alpha U_n, \quad t = \overline{t}/t_0, \quad H = \overline{H}/D,$$

with the time constant, t_0, given by

$$t_0 = \sqrt{\frac{M}{D\alpha^2}}$$

and the dimensionless coupling and dipole-dipole parameters

$$C = \frac{\overline{C}}{D\alpha^2} \quad \text{and} \quad J_{nm} = \frac{2\overline{J}_0}{l^3 D\alpha^2}\overline{J}_{nm},$$

where the dipole-dipole interaction between two charges of q is $\overline{J}_0 = q^2/4\pi\varepsilon_0$ [61] and where we define the dimensionless strength of the dipole-dipole interaction as

$$J_0 = \frac{2\overline{J}_0}{l^3 D\alpha^2}. \tag{2.9}$$

Furthermore, we scale the geometric length by the distance between successive base pairs, l, as $\mathbf{r}_n = \overline{\mathbf{r}}_n/l$, which means that we have

$$|\mathbf{r}_{n+1} - \mathbf{r}_n| = 1.$$

Note the scaling factor 2 in front of the LRI terms. This is because the change of variables implies

$$H_{\text{dip}} = \sum_{n=-N}^{N}\sum_{m} J_{nm}\sqrt{2}u_n\sqrt{2}u_m = 2\sum_{n=-N}^{N}\sum_{m} J_{nm}u_n u_m$$

and we obtain by simple insertion the dimensionless Hamiltonian

$$\boxed{H = \sum_n \left\{ \frac{1}{2}\left(\frac{du_n}{dt}\right)^2 + \frac{C}{2}\left(u_n - u_{n-1}\right)^2 + \left(e^{-u_n} - 1\right)^2 + \frac{1}{2}\sum_{m\neq n} J_{nm}u_n u_m \right\}.} \tag{2.10}$$

The equations of motion The non-dimensional Hamiltonian for the infinitely long chain is noted in Eq. (2.10) and it yields the derivations of motion

$$\ddot{u}_n = C\left(u_{n-1} + u_{n+1} - 2u_n\right) + 2e^{-u_n}\left(e^{-u_n} - 1\right) + \sum_{m\neq n} J_{nm}u_m, \tag{2.11}$$

where the double dots denote double differentiation with respect to time. However, when considering a chain of *finite* length, $n \in [-N, N]$, which is what we can model numerically, we see that at the ends ($n = -N$ and $n = N$), there is no neighboring base pair for the outermost pairs to interact with, and thus the Hamiltonian in these cases is special. In this case we have used *free* boundary conditions

$$\begin{aligned} u_{-N-1} &= u_{-N}, \\ u_{N+1} &= u_N. \end{aligned}$$

The derivation of the equations of motions is mostly trivial and can be found in Appendix A. Thus, we are considering a chain with the total number of sites $N_T = 2N + 1$.

These equations of motion are an augmented version of the general *Klein-Gordon* equations, which are equations of the form

$$\ddot{u}_n - \left(u_{n+1} + u_{n-1} - 2u_n\right) + f(u_n) = 0.$$

Klein-Gordon models possess *discrete breather* solutions. A discrete breather is a localized excitation which has a shape that changes periodically in time as well as it moves in space. Such a breather can be thought of as special, more complicated, type of soliton. A "classical" soliton is a more simple entity in the sense that it travels "only" with a conserved shape, whereas the breather travels with a periodically varying shape. The concepts are used rather loosely in this thesis, and also the terms "excitation" and "pulse" refer to the solution of the equations of motion.

2.1.2 Parameter values

The determination of physically reasonable parameter values for such a delicate structure as DNA is far from straight-forward. Even though the general structure has been known for more than half a century [1], dynamical experiments are difficult and the precise values of the parameters are still investigated. We use the parameter values $D = 0.04$ eV ($= 0.64 \cdot 10^{-20}$ J), $\alpha = 4.45$ Å^{-1} ($= 4.45 \cdot 10^{10}$ m^{-1}), $M = 300$ a.m.u. ($= 5.00 \cdot 10^{-25}$ kg) and the coupling parameter $\overline{C} = 0.06$ eV/Å^2 ($= 0.96$ J/m^2), which have been widely used in DNA-like models [9, 42, 52, 59].The dimensionless stacking parameter then becomes $C = 0.075$, which we use throughout the paper. We note that $\overline{C}$-values between 0.003 eV/Å^2 [55] and 31.7 eV/Å^2 [62] have been reported in the literature.

The distance between adjacent base pairs is $l = 3.4$Å and the inter-strand distance is about 20Å. This means that $u_n = 0$ corresponds to a separation of 20Å. The resulting time constant, $t_0 = 0.20$ ps, is in the picosecond range, as seen in Table 2.1.

Symbol	Parameter	Physical value
$\overline{C}$	stacking	0.96 J/m^2
D	Morse depth	0.64×10^{-20} J
α	inverse Morse width	4.45×10^{10} m^{-1}
M	base pair mass	5.00×10^{-25} kg
q	dipole charge	1.18×10^{-19} C
J_0	interaction strength	0.90×10^{-28} Jm
l	lattice constant	3.4×10^{-10} m
t_0	time constant	0.20×10^{-12} s
ε_0	dielectric constant	8.854×10^{-12} F/m
a.m.u.	atomic mass unit	1.66×10^{-27} kg
Debye	dipole charge	3.34×10^{-30} Cm

Table 2.1: *Physical parameters for the DNA molecule.*

The dipole charge The dipole moment for a given DNA base pair is given through the strength and separation of the dipole moment:

$$q = \frac{d_{\mathrm{Dip}}}{a_{\mathrm{Dip}}}.$$

The value of d_{Dip} is the most controversial one of the DNA parameters and has been explored in e.g. [42, 59, 63]. Values ranging from 2.5 to 7.2 Debye appear in the literature, and in our simulations we use the value $d_{\mathrm{Dip}} = 7.05$ Debye, as this will result in the convenient value $J_0 = 0.5$ (2.12).

The dipole length, a_{Dip}, is easier to determine and is about 2 Å. With 1 Debye $= 3.34 \times 10^{-30}$Cm, this gives a base pair charge of about $q = 1.18 \times 10^{-19}$ C. Note that both d_{Dip} and a_{Dip} are

approximate values taking into account the different hydrogen bonds within the different base pairs.

One should be careful to distinguish between the distance between base pairs — the variable u_n — and the dipole length, a_{Dip}. First, the separation between the DNA polypeptide strands is about 20 Å [2, 35], but the dipole length is only one tenth of that. This indicates that the charge distribution which generates the dipoles originates from the bases between the DNA strands — which naturally are closer to one another than the back bone strands themselves.

Second, this charge is a constant quantity, whereas the dipole moment (and the dipole length) varies through the changes in u_n. However, this has been taken into account through the distance dependence in the LRI term of Eq. (2.8) and the variation of u_n. The used values are summarized in Table 2.1.

The calculation is

$$J_0 = \frac{2\frac{q^2}{4\pi\varepsilon_0}}{l^3 D\alpha^2} = \frac{2\frac{\left(1.18\times10^{-19}C\right)^2}{4\pi 8.854\times10^{-12}\mathrm{F/m}}}{\left(3.4\times10^{-10}\mathrm{m}\right)^3\cdot 0.64\times10^{-20}\mathrm{J}\cdot\left(4.45\times10^{10}\mathrm{m}^{-1}\right)^2} = 0.5. \tag{2.12}$$

3

Introduction to geometry and dipole-dipole interactions

As briefly mentioned earlier, the geometry of the model molecule only comes into play through the long-range interactions. To introduce this effect, we initially consider a simple chain geometry with a very simple model expression for the dipole-dipole interaction. The work presented in this and the following chapter largely corresponds to Ref. [64].

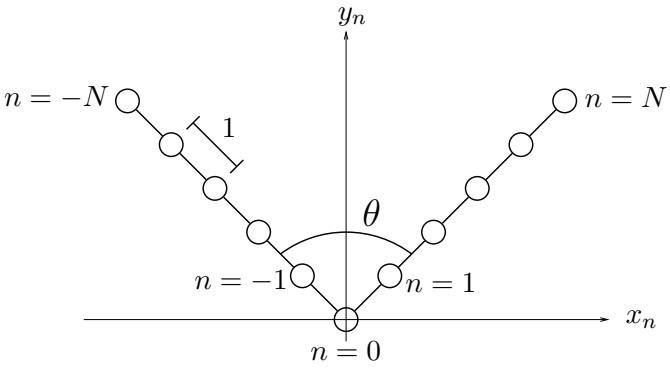

Figure 3.1: *Wedge chain with opening angle, θ.*

Chain geometry We consider the wedge shaped chain as shown in Fig. 3.1. Because of the fixed distance between the base pair sites, the position in the xy-plane of the molecules is given by

$$\mathbf{r}_n = (x_n, y_n) = (n \sin\frac{\theta}{2}, |n| \cos\frac{\theta}{2}), \tag{3.1}$$

where $\mathbf{r}_n$ is the position vector to site n, and where θ the *wedge angle*. The wedge angle is fixed in this investigation, but models with a dynamically varying angles have been considered [45].

Long-range interaction The long-range interaction (LRI) considered here is given by the coefficient

$$\boxed{J_{nm} = \frac{-J_0}{|\mathbf{r}_n - \mathbf{r}_m|^3},} \tag{3.2}$$

where J_0 is given by (2.12). Here, only the distance between base pairs is important, and we thus consider parallel "dipoles", perpendicular to the wedge plane. It springs to mind here is that the negative sign of J_{nm} indicates that the interaction between all dipoles is *attractive*, which is the opposite of how parallel electric dipoles react. However, as we shall see later, it is the *attractive* interaction that is crucial for the behavior of the molecule, and we shall use this model in a preliminary investigation of DNA dynamics.

We choose an inversely cubic distance dependence in this investigation. In fact, earlier studies of the long-range effect in curved molecular chains show that the exact form of the additional dispersion is not crucial as long as it decreases rapidly with distance [54, 51].

3.1 An interesting approximation

In the case of a straight chain with parallel dipoles, an analytical approximation can be used for the dipole-dipole interaction term and by considering the continuum limit, we are able to give an integrable version of the equation of motion. The dipole-dipole interaction may be approximated by (see Sec. B for details)

$$\sum_{m\neq n} J_{nm}u_m \approx \frac{J_0}{l^3}\left(2\zeta(3)+\frac{3}{2}\partial_n^2\right)u_n, \tag{3.3}$$

where we find the Riemann ζ-function,

$$\zeta(s)=\sum_{k=1}^{\infty}\frac{1}{k^s}.$$

The approximation is only valid for an almost straight chain and hence not very relevant when investigating geometrical effect, but what *is* interesting is that the solution to the equations of motion is of the form (consult Appendix B for details and introduction of variables)

$$2i\omega\phi^{(1)}_{\tau_1}+\left(\alpha-v^2\right)\phi^{(1)}_{\xi_1^2}+\left(\frac{30}{\alpha}-7\right)|\phi^{(1)}|^2\phi^{(1)}=0,$$

which is the nonlinear Schrödinger equation (NLS). This is remarkable, as the NLS is well-known in nonlinear optics, and we shall meet it in Part II of this Thesis. Thus, the NLS is truly a versatile equation.

We can solve the NLS, and the result is presented in Eq. (3.4) with $t=0$ and $n^*\equiv n-\nu$ for simplicity (Appendix B)

$$u_n(t=0)=2A\mathrm{sech}\left(Bn^*\right)\cos\left[\left(\gamma+q\right)n^*\right]+\frac{6}{\alpha}A^2\mathrm{sech}^2\left(Bn^*\right)-\frac{2}{\alpha}A^2\mathrm{sech}^2\left(Bn^*\right)\cos\left[2\left(\gamma+q\right)n^*\right], \tag{3.4}$$

with constants (consult Appendix B for details)

$$\begin{aligned}\gamma &= \frac{\omega v}{(\alpha-v^2)}\\ B^2 &= \gamma^2-2\frac{\omega\Lambda}{(\alpha-v^2)}\\ A^2 &= \frac{2\left(\alpha-v^2\right)B^2}{\frac{30}{\beta}-7}\end{aligned}$$

As mentioned, this expression is only valid for straight chains, and even then we notice some erroneous effects from the conversion between a discrete and continuous formulation. But even if it is not feasible as use when considering geometry, we have successfully used it to test the developed numerical code.

3.2 Long-range interaction

Let us turn to the effect of the long-range interactions (3.2) on the wedge shaped chain. For a straight chain, $\theta = 180°$, the LRI terms are identical at all sites, n, and have the shape plotted in Fig. 3.2(a). So at every site, n, we see that there is no dipole-dipole interaction *at* site n — a dipole

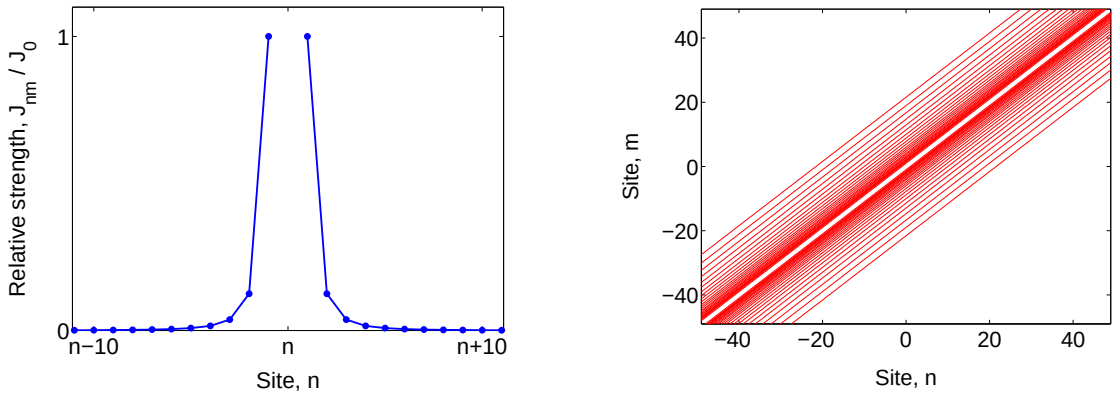

(a) Profile of the LRI.

(b) Contours for all n and m.

Figure 3.2: *Long-range interaction at site n for a straight chain, $\theta = 180°$. In (b), logarithmically spaced contours from 5×10^{-4} to 1 are used. Only in the case $\theta = 180°$ all the profiles at different sites are identical.*

cannot interact with itself. The contribution from sites $n-1$ and $n+1$, however, is large and equal to J_0, consistent with the denominator in (3.2) is 1, the distance between neighboring sites. Due to the inverse cubic distance dependence the contribution from sites further from n quickly wears off for this straight chain.

Fig. 3.2(b) shows a contour plot of the same situation, with 25 contours logarithmically spaced (from 0.0005 to 1) to catch some of the rapidly decaying tails. The way to interpret this contour plot is as follows: Choose a site number, n, on the abscissa. Then proceed m sites upwards to find the interaction between sites n and m.

The appearance of this kind of plot is modified with the introduction of the wedge. Close to the center region — the wedge *tip* — the distance between sites on different legs of the wedge is decreased with decreasing wedge angle, θ. Because of the relation (3.2), this means that the dipole-dipole interaction between these sites is increased. The effect is shown for $\theta = 35°$ in Fig. 3.3. In the top row, we consider the site $m = -3$, slightly left of the wedge tip. From the figure on the left it is clear that the distance between sites $n = 2$ and $m = -3$ is *smaller* than the distance between sites $n = 0$ and $m = -3$. For $m = -3$, $n = 2$ is 5 sites away $(m + 5)$ corresponding to the "hump" on the right part of the figure, Fig. 3.3(a). In the bottom row, we have moved yet another site closer to the bend and the effect is even more pronounced. The situation on the right leg of the wedge, $m > 0$, is completely analogous.

Fig. 3.4 shows contour plots similar to Fig. 3.2 for different wedge angles. We see how the long-range interaction constitute the *nonlocality* of the system. For a given chain site close to the bend, the notion of nonlocality implies that in order to determine the dynamics at site at given site, we need to include more terms than just the nearest neighbor. By convention, the term "long-range interaction" is traditionally used in molecular modeling instead of "nonlocality".

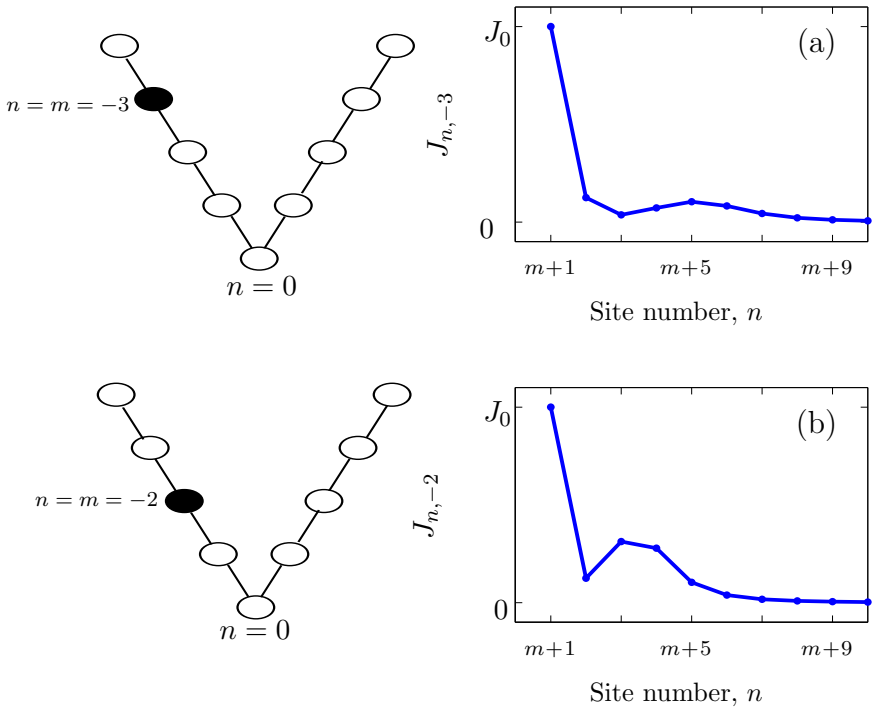

Figure 3.3: *Profile of the long-range interaction coefficient J_{nm} for fixed (a) $m = -3$, (b) $m = -2$. $\theta = 35°$. Note how the effect from sites other than the neighbor becomes important in the vicinity of the wedge tip when bending is present.*

3.3 Breather dynamics

The dynamics of nonlinear excitations has been investigated before in various inhomogeneous models (see e.g. [9, 11, 12, 13, 14, 15, 22, 23, 25, 30, 31, 32, 33, 34, 35, 36, 37, 38, 39, 40, 41]).

A 4th order Runge–Kutta solver is used to simulate Eqs. (2.11) on a chain with $N_T = 301$ sites. A stepsize in time of 0.005 ensures conservation of the Hamiltonian to a relative accuracy of 10^{-10} throughout. We use a Gaussian initial condition

$$u_n(t) = A \exp\left[-k\big((n-\nu) - vt\big)^2\right], \qquad (3.5)$$

where site ν denotes the initial position of the center of mass as the initial excitation, v is the initial velocity of the pulse and k its width and A its amplitude, see Fig. 3.5.

In the following we use the velocity $v = 0.2$, the width $k = 0.2$ and the amplitude $A = 0.5$, because they turn out to provide the right balance between nonlinearity and dispersion to allow the initial condition to evolve rapidly into a discrete moving breather. Insertion of Eq. (3.5) with these parameter values into the total Hamiltonian gives $H = 0.13$. After some initial radiation, the moving breather turns out to possess the *soliton energy*, $H_s \approx 0.08$.

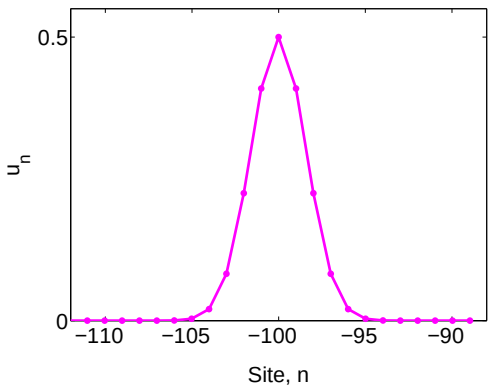

Figure 3.5: *Initial condition (3.5), for $N_T = 301$, $v = 0.2$, $k = 0.2$, $A = 0.5$ and $\nu = -100$. The width is chosen to be comparable with that of the LRI in Fig. 3.2(a).*

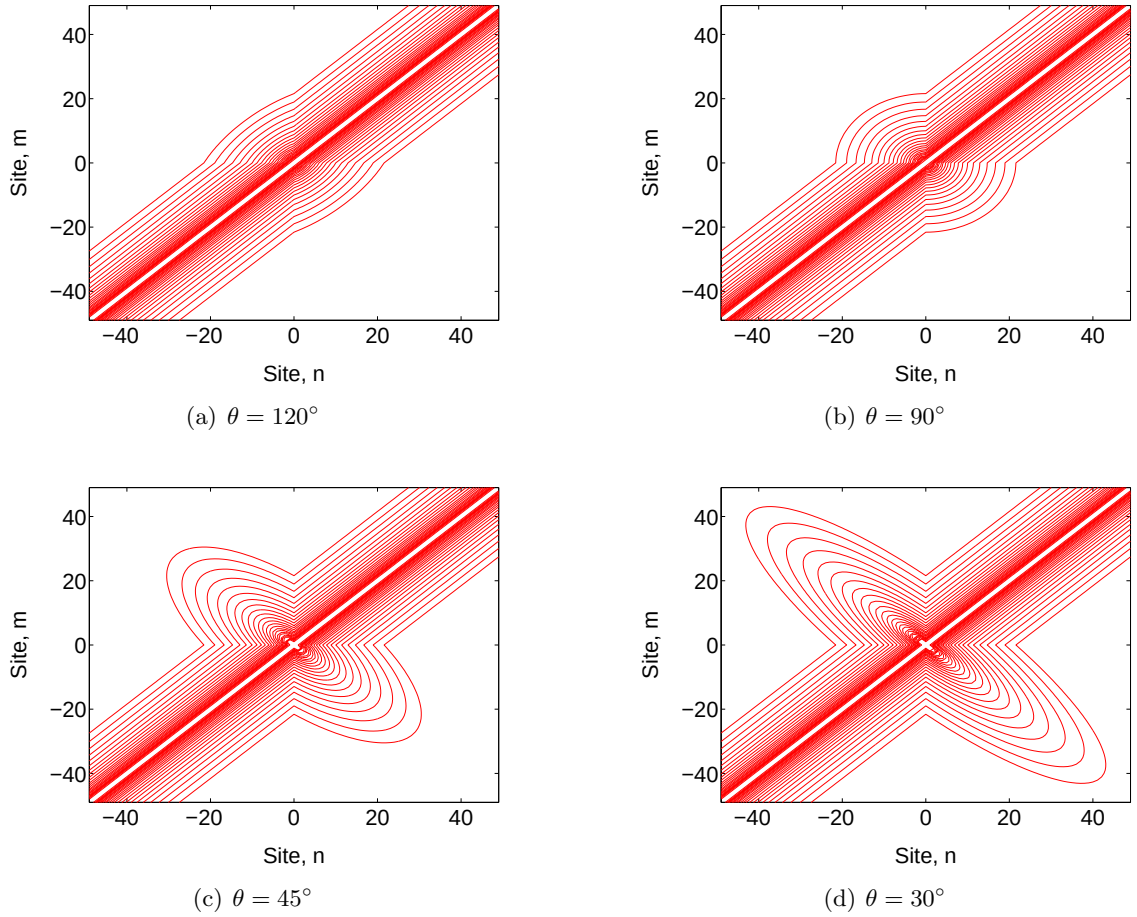

(a) $\theta = 120°$ (b) $\theta = 90°$

(c) $\theta = 45°$ (d) $\theta = 30°$

Figure 3.4: *Contour plots of the long-range interaction for a wedge chain for different wedge angles, θ. Logarithmically spaced contours from 5×10^{-4} to 1.*

As it turns out, our system supports discrete breathers, which are localized wave packets with oscillatory amplitude. This means that the amplitude is inconvenient to monitor and we therefore the positive Hamiltonian density

$$\mathcal{H}_n = \frac{1}{2}\left(\frac{du_n}{dt}\right)^2 + \frac{C}{2}\left(u_n - u_{n-1}\right)^2 + \left(e^{-u_n} - 1\right)^2 + \frac{1}{2}\sum_{m \neq n} J_{nm} u_n u_m \tag{3.6}$$

which measures the energy content at a given site, n. This way we can monitor where the energetic parts of the molecule is. We perform simulations where we launch a Gaussian pulse at site $\nu = -100$ with a velocity towards the wedge center.

Consider for example Fig. 3.6, in which contour plots for the evolution of the Hamiltonian density is shown for two different wedge angles. On the abscissa is marked the chain sites (the outer parts are left out as nothing extraordinary is happening there), while the ordinate shows the evolution in time. Brightly colored lines indicate a high value. A weak bend with $\theta = 140°$ has no significant effect on the pulse [Fig. 3.6(a)] and only a slight decrease of the velocity after passage of the center region is observed. In contrast for a stronger bend, $\theta = 95°$, a considerable part of the excitation is trapped at the tip of the wedge at $n = 0$.

Very strong bends (smaller wedge angles) turn out to result in reflection of the incident breathers.

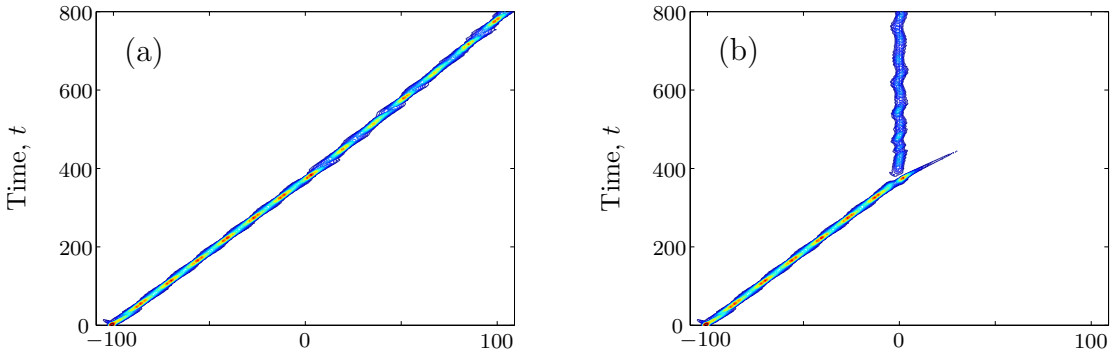

(a) $\theta = 140°$ (b) $\theta = 95°$

Figure 3.6: *Contour plots for the evolution of the Hamiltonian density, $\mathcal{H}_n$, for $N_T = 301$, $C = 0.075$, $J_0 = 0.5$, $v = 0.2$, $k = 0.2$, $A = 0.5$ and $\nu = -100$, yielding $H = 0.13$. 25 equidistant contours $H = 0.005 \ldots 0.05$. (a) $\theta = 140°$ (transmission), (b) $\theta = 95°$ (trapping).*

Such scattering properties and their dependence on the strength of the bend-induced impurity, are similar to those of a linear impurity [65] and those of large amplitude breathers acting as an effective impurity [30, 31]. We stress that the specific shape of the bend does not affect the scattering properties of the bent chain. Thus similar properties were observed in a parabolic chain [66].

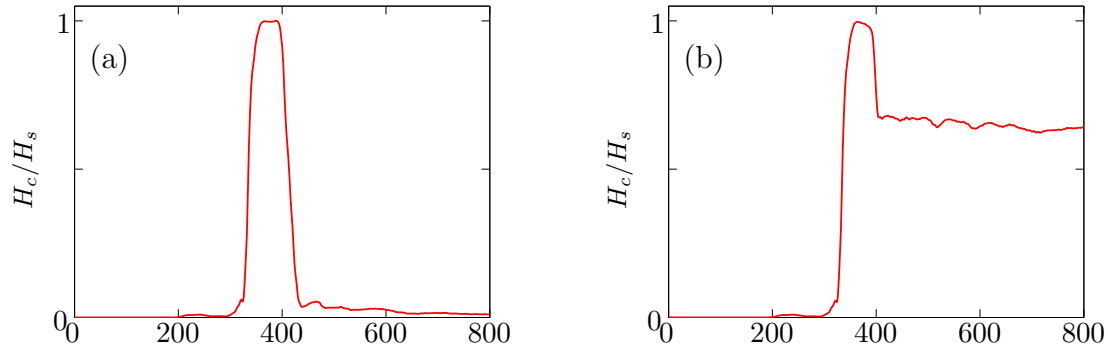

(a) $\theta = 140°$ (b) $\theta = 95°$

Figure 3.7: *Relative central energy, H_c/H_s, for the simulations in Fig. 3.6. (a) $\theta = 140°$ (transmission), (b) $\theta = 95°$ (trapping).*

To analyze the processes in detail, we calculate the central energy, H_c, in 21 sites around $n = 0$ (21 being a typical span of the denaturation bubble of the DNA molecule [10, 9])

$$H_c = \sum_{n=-10}^{10} \mathcal{H}_n, \tag{3.7}$$

where $\mathcal{H}_n$ is from (3.6). The results are shown in Fig. 3.7. Here, time is on the abscissa and the ordinate shows the fraction of the energy in the central region, relative to the soliton energy, H_s. The plots corresponds to summing the Hamiltonian density along a 21 site wide strip in the middle of the plots in Fig. 3.6. In the transmission case with a small bend, Fig. 3.7(a), nearly all the

energy leaves the region. In the trapping case with a stronger bend, Fig. 3.7(b), the trapped energy is stabilized at about $H_c/H_s \approx 64\%$. Thus only part of the energy is trapped.

What fraction of energy that remains trapped at the wedge tip depends on the wedge angle, as is clear from Figs. 3.6 and 3.7. To be more precise, we perform simulations for different θ and record the central energy after 800 time units as a function of the wedge angle. The result is shown in Fig. 3.8. We see that for smaller and larger θ-values, the energy is lost through reflection and transmission, respectively. Efficient trapping is found for intermediate wedge angles, $90° < \theta < 107°$ and the optimal wedge angle for trapping is seen to be around $\theta = 95°$.

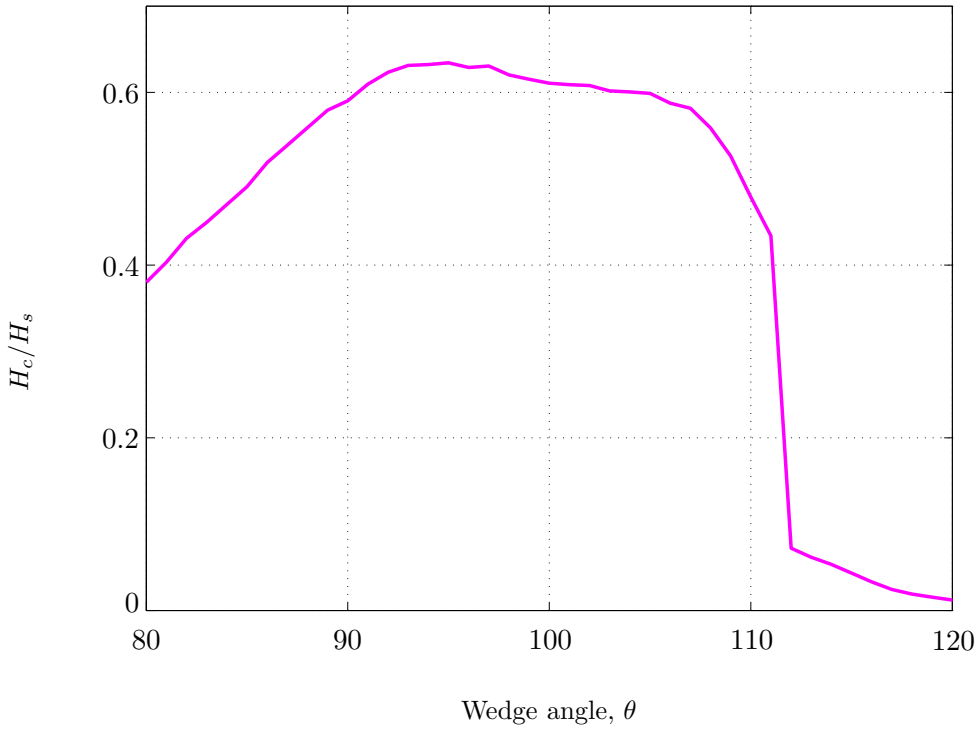

Figure 3.8: *Relative central energy, H_c/H_s, at $t = 800$ versus wedge angle, θ. System parameters as in Fig. 3.6.*

From Fig. 3.8 it is apparent how the wedge angle governs the ability of the model chain to trap an incoming excitation. We stress that this is an effect in an intrinsically homogeneous chain and that it is exclusively governed by the nonlocality.

3.3.1 Multiple breather dynamics

If the ability of a chain bend to trap energy is to be more than a curiosity, then the effect needs to be more pronounced that merely trapping a single incoming breather. To this end, we initially investigate the chain's ability to trap multiple incoming, shown in Fig. 3.9. A first Gaussian pulse (I) is launched at site $\nu = -100$ at $t = 0$. At $t = 800$ both the displacements and the velocities are set to zero, $u_n(800) = 0$ and $\dot{u}_n(800) = 0$, outside the bent region, $|n| > 15$, to remove radiation. This "cleaned" chain is now used as an initial condition for a new simulation, in which we add a second identical Gaussian pulse (II) launched at site $\nu = -87$. Like in other systems the interaction between two breathers, or a breather and an impurity, depends strongly on the relative phase. We

choose $\nu = -87$ for the launching of this second pulse to obtain maximal trapping. Using the same procedure, a third identical Gaussian pulse (III) is launched at $t = 1600$, now at $\nu = -89$. Note that the absolute value of the central energy is shown here, as the relative value only made sense for a single breather, without the elimination of radiation.

As seen in Fig. 3.9 we essentially succeed in trapping 3 breathers at the tip of the wedge chain. Some energy transmission is observed when breathers I and II are trapped, while some reflection occurs at the trapping of breather III. By successively handling the initial conditions as described above, we avoid radiation which, when reflected at the boundaries, distorts the numerical simulations.

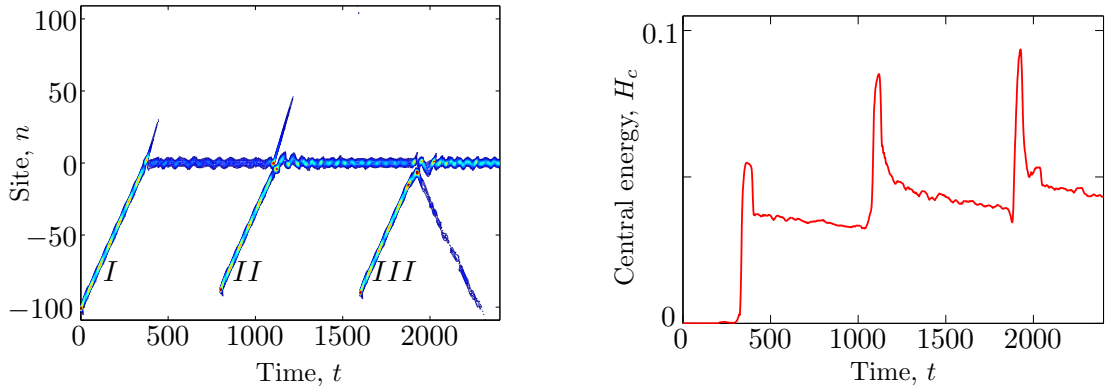

(a) Hamiltonian density, $\mathcal{H}_n$

(b) Central energy, H_c

Figure 3.9: *Trapping of breathers I, II and III at $n = 0$. Contour plot (a) with 25 equidistant lines $H = 0.005 \ldots 0.05$ and central energy, H_c, vs time, t. $N_T = 301$, $J_0 = 0.5$, $v = 0.2$, $k = 0.2$, $A = 0.5$. I : $\nu = -100$ at $t = 0$, II : $\nu = -87$ at $t = 800$, III : $\nu = -89$ at $t = 1600$.*

The corresponding energy evolution for the central site energy is shown in Fig. 3.9(b). The ability of the system to trap energy at the bending region is evident, even though more radiation is observed as the number of trapped breathers increases. As noted also in connection with Fig. 3.7(b), the first incident breather, I, loses about 36% of the total energy before trapping. For the following breathers, II and III, both of the corresponding losses amount to 50%. Thus the possibility for trapping more energy at the chain bend by additional incoming breathers may seem exhausted due to an effective saturation.

4

Funneling of thermal energy

The trapping of breathers observed in the previous Chapter suggests that the bend may funnel energy from the surrounding region. In order to study this in detail, we now explore the dynamics of the chain in the case of *random initial conditions*, as these are meant to model thermal fluctuations.

4.1 Thermal initial conditions

The energy trapping effect demonstrated in the previous Section 3.3 is reassuring, but one may argue that the initial Gaussian pulse is not a very biological effect. We therefore also consider *random thermal fluctuations* as initial condition, which is the topic of this Section.

The physical DNA molecule exists in an environment filled with thermal fluctuations — at body temperature — so it is a very relevant investigation to make. Thermal fluctuations have previously been considered in nonlinear lattices and random initial disturbances have been shown to be able to evolve into nonlinear localized excitations by modulational instabilities. Thus created, the solitons can interact with each other or with any inhomogeneity present [9, 33, 34, 35, 38, 39, 40]. Relevant for our context is of course the interaction with the effective inhomogeneity caused by the bend. In [33, 34, 35], the number of generated solitons were found to depend on the temperature of the system, T, to the power 1/3, and that a significant number of solitons were generated at physiological temperatures. Thus, the "solitonic" approach is by no means irrelevant.

We use the same method of calculating the temperature as in [34]:

$$\frac{1}{2}M\left\langle \dot{U}_n^2 \right\rangle = k_B T, \tag{4.1}$$

where U_n is the physical unscaled variable and $\langle \dot{U}_n^2 \rangle$ the variance of its time derivative. In this approach we assume for simplicity a mean of 0 on $\dot{U}_n$ for all n sites, as well as zero amplitude, $U_n = 0$ for all n. This means that we assume all the initial thermal energy is kinetic, and the initial model chain is a perfect DNA "ladder" with equal (equilibrium) distance but with random velocities, both negative (moving the base pairs closer) and positive (moving them apart). However, the system quickly transfers some

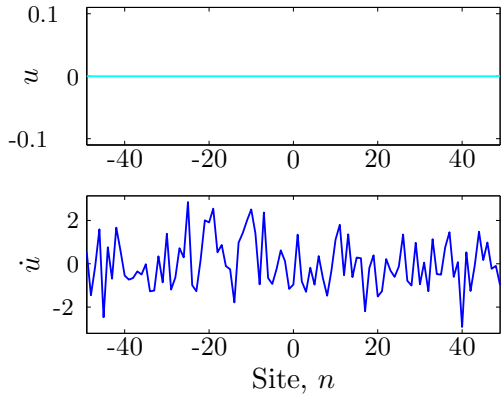

Figure 4.1: *Random initial conditions.*

of the kinetic energy to potential (so that we also have displacements, u_n, different from zero as well as velocities, $\dot{u}_n$), a more physiologically reasonable situation.

Since we use the scalings (repeated from Sec. 2.1.1)

$$t = \sqrt{\frac{D\alpha^2}{M}}\bar{t} \qquad \text{and} \qquad u_n = \frac{1}{\alpha}U_n,$$

we find

$$T = \frac{M}{2k_B}\left\langle \dot{U}_n^2 \right\rangle = \frac{M}{2k_B}\left\langle \left(\frac{1}{\alpha}\sqrt{\frac{D\alpha^2}{M}}\frac{du_n}{d\bar{t}}\right)^2 \right\rangle = \frac{D}{2k_B}\left\langle \dot{u}_n^2 \right\rangle = \frac{D}{2k_B}\sigma_{\dot{u}_n}^2.$$

With $k_B = 1.3807 \times 10^{-23}$ J/K and $D = 0.04\text{eV} = 0.64 \times 10^{-20}$J, we find the standard deviation corresponding to physiological temperature (310K):

$$\left\langle \dot{u}_n^2 \right\rangle = \frac{2 \times 310\text{K} \times 1.3807 \times 10^{-23}\text{J/K}}{0.64 \times 10^{-20}\text{J}} = 1.34, \tag{4.2}$$

and the standard deviation is the square root of (4.2): $\sigma_{\dot{u}_n} = 1.156$.

4.2 Analytical expectations

Before we perform simulations on the wedge chain with thermal initial conditions, we pause to investigate what we can expect from analytical considerations.

4.2.1 The blow up effect

A way of assessing the dynamical behavior of the model is found by considering a chain with only two sites: the *dimer* case. We choose for example the center sites $n = 0$ and $n = 1$. Assuming that both displacements are equal, $u_0 = u_1 \equiv u$, the coupling term in the Hamiltonian, Eq. (2.10), vanishes and we are left with

$$H = \dot{u}^2 + 2\left(e^{-u} - 1\right)^2 - Ju^2, \tag{4.3}$$

with $J = |J_{01}| = |J_{10}|$. The effective potential

$$V(u) = 2\left(e^{-u} - 1\right)^2 - Ju^2 \tag{4.4}$$

is shown as the dashed red curve in Fig. 4.2. It is thus an *infinite* potential well, resulting in infinite growth of the oscillation amplitude if some threshold value of the displacement is exceeded. Equation (4.3) may now be integrated as

$$t - \hat{t} = \int_{\hat{u}}^{u} \frac{dw}{\sqrt{H - 2\left(e^{-w} - 1\right)^2 + Jw^2}} \tag{4.5}$$

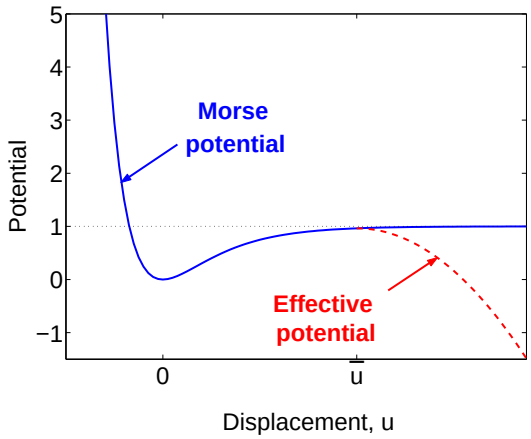

Figure 4.2: *Modified Morse potential for the dimer case. For displacements larger than a given threshold, an infinite potential well occurs.*

where $u = \hat{u}$ at the time $t = \hat{t}$. Choosing $\hat{t}$ so large that $w \gg 1$, the power term in the square root of Eq. (4.5) dominates (as seen in Fig. 4.2). Therefore, Eq. (4.5) may be approximated as

$$t - \hat{t} \approx \int_{\hat{u}}^{u} \frac{dw}{\sqrt{Jw^2}},$$

from which we find $u \propto \exp\left[\sqrt{J}(t-\hat{t})\right]$, in accordance with the exponential behavior found numerically in Fig. 4.4, page 28.

Thus the existence of an exponential increase of the oscillation amplitude — a *blow up* — is predicted in the dimer case, when some threshold value of u is exceeded.

We stress that if a harmonic potential is used as the inter-strand potential instead of the Morse potential — so that the resulting effective dimer potential is in this case $V^{\text{Eff}}_{\text{harmonic}}(u) = (2-J)u^2$ — the effective potential (4.4) does *not* give a potential well for the physical relevant value of J.

We also see that a larger value of J acts to decrease the threshold for the onset of the potential well in Fig. 4.2; this was confirmed in some simulations (not mentioned further here).

4.2.2 Effective potential

The potential well described in Sec. 4.2.1 may also be found by considering the long-range interaction as follows:

$$\sum_n \sum_{m\neq n} J_{nm} u_n u_m = -\frac{1}{2} \sum_n \sum_{m\neq n} J_{nm} \left(u_n - u_m\right)^2 + \sum_n \sum_{m\neq n} J_{nm} u_n^2. \tag{4.6}$$

This is easily verified, remembering $\sum_n \sum_m J_{nm} u_n^2 = \sum_n \sum_m J_{nm} u_m^2$. In (4.6) the first summations on the right hand side correspond to an inhomogeneous dispersion energy (seen in Fig. 3.3), while the second summation corresponds to an *effective on-site potential* [51]. This quantifies the effect of the LRI at a given site and we introduce the notation $V_n^{\text{Eff}} \equiv \sum_{m\neq n} J_{nm}$. With negative values of J_{nm}, the potential V_n^{Eff} has the double-well profile, shown in Fig. 4.3. Changing the wedge angle has the effect of making the wells deeper, which is shown both in Fig. 4.3(a) and (b). Fig. 4.3(a) are cuts of Fig. 4.3(b) at wedge angles $\theta = 120°, 95°$ and $80°$, except that the mesh plot is subtracted the "ground state" potential V_∞, *i.e.,* the potential far from the bend. From Fig. 4.3(a), this value is about -1.2.

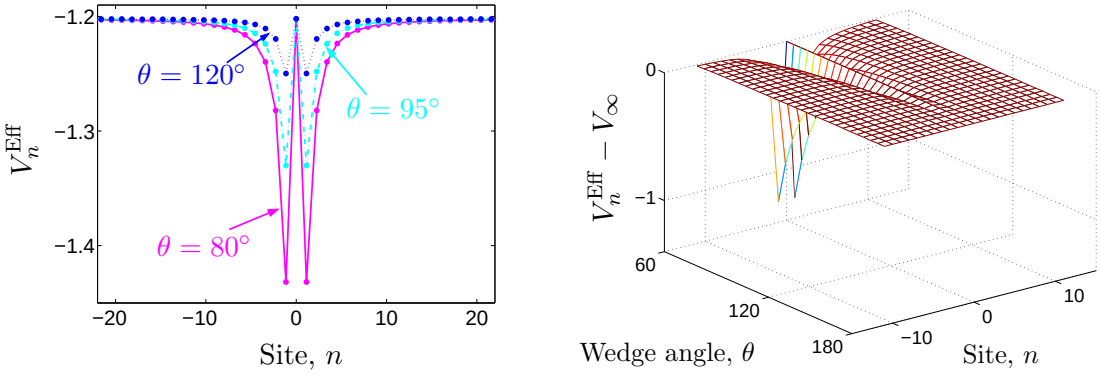

(a) $\theta = 80°, 95°, 120°$ (b) $180° \leq \theta \leq 60°$

Figure 4.3: *Effective "ground state" potential,* $V_n^{\text{Eff}} \equiv \sum_{m\neq n} J_{nm}$*, versus site number,* n*, for different wedge angles,* θ*.*

The mesh plot in Fig. 4.3(b) shows — for a given wedge angle between 60° and 180° — the potential arising from the long-range interactions at given sites. For example, by choosing $n = -1$ we see that for a straight chain, $\theta = 180°$, the dipole-dipole interaction is the same at all sites and we see how a stronger bend (smaller wedge angle) increases the depth of the potential well at this

site, corresponding to (4.4). At the center site $n = 0$ we always have the same potential because in the wedge chain, neither the distance from site $n = 0$ to all other sites, nor the dipole orientation, changes with the wedge angle, θ.

We have already seen how this geometrically generated "impurity", or effective on-site potential, introduced by the bend can trap or transmit incoming excitations (Sec. 3.3). In the following we shall see its effect on random initial conditions.

4.3 Fluctuations on the wedge chain

With the random initial conditions generating solitons, we find that collision of the nonlinear excitations may result in exponential growth of the oscillation amplitude at the collision site as predicted in Secs. 4.2.1 and 4.2.2. Fig. 4.4 depicts the deviation from the equilibrium base pair distance, u_n, for a given site at physiological temperature ($T \approx 310$K, solid line). We see that the amplitude increases exponentially as expected — also shown is a different initial condition corresponding to a lower temperature ($T \approx 7$K, dashed line) where the exponential shape is a bit more clear. This unbounded growth of amplitude implies energy localization at the site.

For this very realization of the initial condition, the depicted site $n = -1$, *i.e.,* just to the left of the center, for a bending angle of 45°. But it is emphasized that the behavior can be found at *all* chain sites and for all bending angles!

In this case of always attractive dipole-dipole interaction, a blow up at one site will spread, causing blow up at neighboring sites, which in turn cause blow up at further sites and so on.

It is noted that this blow up effect is also found for the Gaussian initial conditions considered in Sec. 3.3. They are predominantly found for small wedge angles, where the dipole-dipole interaction is most strongly augmented due to the bending. When considering collision between breathers, the blow ups will occur when the added oscillations exceed the threshold mentioned in Sec. 4.2.1, but a thorough investigation is not performed here.

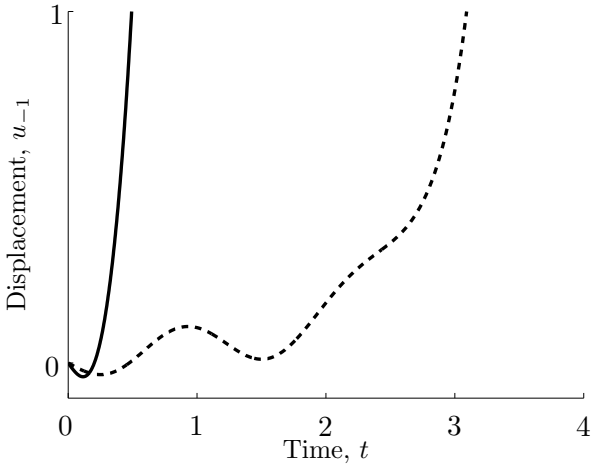

Figure 4.4: Displacement at site $n = -1$, u_{-1}, versus time on bent chain with $N_T = 99$ and $\theta = 45°$ for random initial velocities generated with normal distribution: $<\dot{u}_n>= 0$ and $\sigma_{\dot{u}_n} = 1.156$, or $T \approx 310$K, (solid) and $\sigma_{\dot{u}_n} = 0.17$, or $T \approx 7$K, (dashed). Initial displacements: $u_n = 0$ for all n.

4.3.1 Statistical approach

We conduct simulations for 500 different realizations with zero displacement, $u_n = 0$, and velocities normally distributed with zero mean, $<\dot{u}_n>= 0$ and standard deviation $\sigma_{\dot{u}_n} = 1.156$ are used as determined in Sec. 4.1, corresponding to a temperature of about 37°C. We note where the initial blow up occurs and present these records in the following histogram plots.

Our results for a straight chain of length $N_t = 99$ are depicted in Fig. 4.5(a) showing a histogram of the occurrences of sites with a displacement above the threshold value $u_n = 10$, corresponding to the value for DNA opening used in [67]. The simulations were discontinued when this threshold value was exceeded. These threshold transgressions, which in most cases occur after a few time units, are seen to be uniformly distributed along the chain.

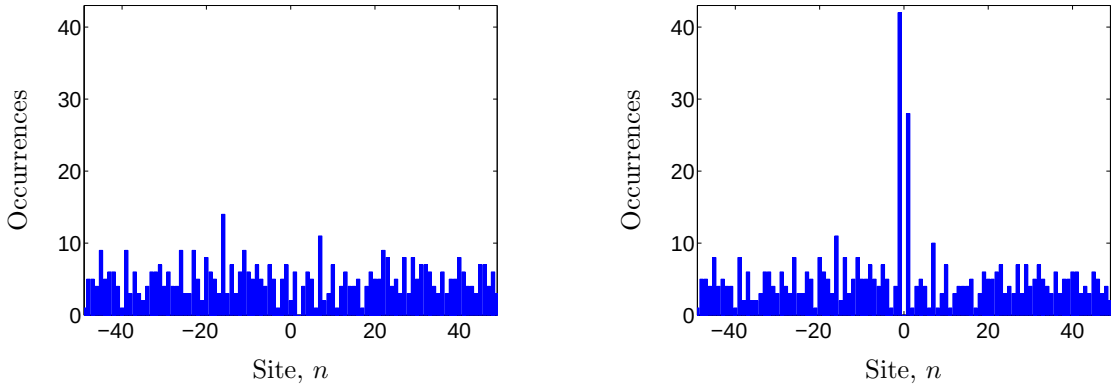

(a) Straight chain, $\theta = 180°$

(b) Wedge chain, $\theta = 45°$

Figure 4.5: *Occurrence of amplitudes above threshold,* $u_n > 10$*, versus site,* n*, for* $N_T = 99$ *until max.* $t = 10,000$*. Initial displacements:* $u_n = 0$ *for all* n*. 500 random initial velocities with normal distribution:* $<\dot{u}_n> = 0$ *and* $\sigma_{\dot{u}_n} = 1.156$*,* $T \approx 310K$*.*

On a wedge chain with bending angle $\theta = 45°$, identical initial conditions give the remarkably different result shown in Fig. 4.5(b). We see that 70 (out of 500) threshold transgressions occur at the sites $n = -1$ and $n = 1$, between which the long–range interaction is most strongly increased due to the bending. Thus energy localization, implied by unbounded growth of amplitude, is observed in the vicinity of the tip of the wedge which therefore acts as an energy funnel.

5 A proper dipole-dipole interaction

So far we have been considering a not very realistic expression for the dipole-dipole long-range interaction, namely all parallel dipoles, perpendicular to the chain plane and with *attracting* interaction. This is of course a rather crude approximation, as parallel dipoles mutually repel each other, but it was chosen as a first try because the erroneously attracting interaction quickly wears off with distance. Attraction between dipoles is by no means impossible, but to give a proper description of it, we need to introduce the *twist* of the chain. The work presented in this chapter largely corresponds to what is published in [68].

First, however, a few words about dipole-dipole interaction, which is far from trivial. The potential interaction energy between 2 electric dipoles of elementary charge is given by

$$V(\mathbf{r}) = \frac{1}{4\pi\varepsilon_0} \frac{\mathbf{d}_n \cdot \mathbf{d}_m - 3\,(\mathbf{d}_n \cdot \mathbf{r}_{nm})\,(\mathbf{d}_m \cdot \mathbf{r}_{nm})}{|\mathbf{r}_n - \mathbf{r}_m|^3}, \tag{5.1}$$

where $\mathbf{r}_n$ and $\mathbf{d}_n$ are the position vector and the unit dipole vector at the nth site, respectively, and $\mathbf{r}_{nm}$ denotes the unit vector from the nth to the mth site

$$\mathbf{r}_{nm} = \frac{\mathbf{r}_n - \mathbf{r}_m}{|\mathbf{r}_n - \mathbf{r}_m|}.$$

This is a standard textbook result, see e.g. [58]. Thus the orientation of the dipoles governs their mutual interaction, and a few possible configurations and their respective interaction are given in Table 5.1. Note — as indicated in the Table — that even when considering only parallel dipoles,

Dipole configuration		Interaction strength	Interaction
$\Rightarrow$	$\Rightarrow$	-2	Attractive
$\Rightarrow$	$\Leftarrow$	4	Repulsive
$\Uparrow$	$\Uparrow$	1	Repulsive
$\Uparrow$	$\Downarrow$	-1	Attractive

Table 5.1: *Some possible orientations for 2 dipoles and their interaction energy. The center column indicates the relative strength and nature of the interaction.*

the interaction can change from attraction to repulsion. For parallel dipoles, the general expression (5.1) changes to

$$V(\mathbf{r}) = \frac{1}{4\pi\varepsilon_0}\left[1 - 3\left(\mathbf{d}_n \cdot \mathbf{r}_{nm}\right)\left(\mathbf{d}_m \cdot \mathbf{r}_{nm}\right)\right]. \tag{5.2}$$

With $\mathbf{r}$ being the unit vector, both the scalar products become $\cos\theta$ and the potential a function of θ

$$V(\theta) = \frac{1}{4\pi\varepsilon_0}\left(1 - 3\cos^2\theta\right) = \frac{-1}{8\pi\varepsilon_0}\left(1 + 3\cos 2\theta\right), \tag{5.3}$$

which is depicted in Fig. 5.1. We see that the interaction is attractive (negative), when the absolute value of the angle θ is less than $|\theta_0| < \arccos\frac{1}{\sqrt{3}} \approx 0.96$. This is to show that even parallel dipoles can be both attracting and repelling each other. The interaction between more than 2 dipoles is described by

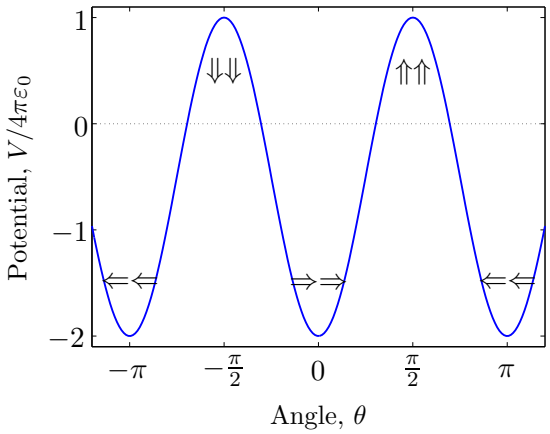

Figure 5.1: *The sign and orientation of the interaction between 2 parallel dipoles as a function of their common angle of rotation, θ. Plot of $V(\theta)$ from (5.3).*

$$V_{\text{Dip}} = \frac{1}{2}\sum_{n\neq m} J_{nm} u_n u_m, \tag{5.4}$$

with

$$\boxed{J_{nm} = \sum_{n\neq m} \frac{\mathbf{d}_n \cdot \mathbf{d}_m - 3\left(\mathbf{d}_n \cdot \mathbf{r}_{nm}\right)\left(\mathbf{d}_m \cdot \mathbf{r}_{nm}\right)}{|\mathbf{r}_n - \mathbf{r}_m|^3}.} \tag{5.5}$$

The factor of 1/2 in (5.4) is needed since all contributions are otherwise counted twice and the u_n and u_m accounts for the varying distance between base pair dipoles. This distance and the charge of the base pairs modify the expression (5.1), written for elementary charges. The factor J_{nm} is here scaled as (2.9) [repeated from page 13],

$$J_{nm} = \frac{2\overline{J}_0}{l^3 D\alpha^2}\overline{J}_{nm}, \quad \text{with} \quad \overline{J}_0 = \frac{q^2}{4\pi\varepsilon_0}.$$

We note that for dipoles perpendicular to the model chain axis, which is oriented along the x-axis, the last term of (5.5) vanishes and we are left with something resembling the preliminary result, only with repulsive interaction.

To determine the actual dipole moments, $\mathbf{d}_n$, we need to know the chain geometry.

5.1 The twist function on a parabola chain

To this end, we also abandon the wedge shaped chain in Fig. 3.1 in favor of a parabola embedded chain, $y_n = \frac{\kappa}{2}x_{n-\eta}^2$, sketched in Fig. 5.2. A normal vector in the xy-plane is found though

$$\tan\psi_n = \kappa x_n.$$

Using basic trigonometry[1], a unit normal vector in the chain plane is

$$\mathbf{n} = \pm\left(-\sin\psi_n, \cos\psi_n\right) = \left(\frac{-\kappa x_n}{\sqrt{1+\kappa^2 x_n^2}}, \frac{1}{\sqrt{1+\kappa^2 x_n^2}}\right), \tag{5.6}$$

[1]We have a right-angled triangle with sides of length 1 and κx_n, so the hypotenuse is of length $1 + \kappa^2 x_n^2$

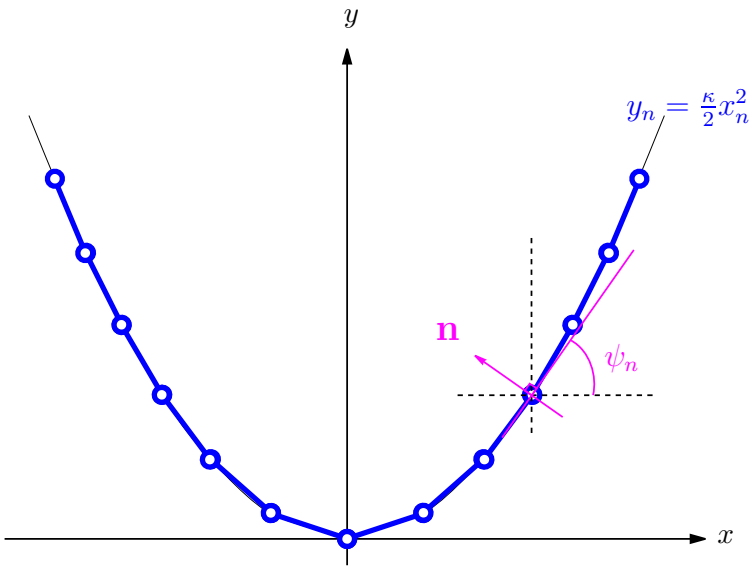

Figure 5.2: *The parabola shaped chain with a normal vector depicted. Also marked is the tangent, needed for calculation of the normal vector.*

where the positive sign is chosen to have "inward pointing" normal vectors as in Fig. 5.2.

Here, the value of the *symmetry center* η is zero. This means that the symmetry axis of the model chain is coinciding with a base pair site at $n = 0$ — this is also referred to as the *on-site* case. Only one other possibility is considered here, namely $\eta = \frac{1}{2}$, the *intersite* case. In this, the axis of symmetry runs between the two sites $n = 0$ and $n = 1$. The two cases are sketched in Fig. 5.3.

(a) On-site case, $\eta = 0$ ((b) Intersite case, $\eta = \frac{1}{2}$

Figure 5.3: *Chain configurations.*

Regardless of the choice of η, the chain is always embedded on a parabola. In contrast to the wedge chain, Eq. (3.1), an analytical expression for the position of chain sites with mutual unit distance is not available. The position of the sites are determined by a bisection method.

We still consider dipoles perpendicular to the molecular chain, but we also need to quantify their direction. To do this, we introduce the *twist function*, ϕ_n

$$\boxed{\phi_n = 2 \arctan\left(e^{-\tau(n-\eta)}\right).} \tag{5.7}$$

This expression varies the dipole orientation from having an angle with respect to the z axis of π to 0 with position n. How quickly this happens is governed by the value of the *twist*, τ, see Fig. 5.4.

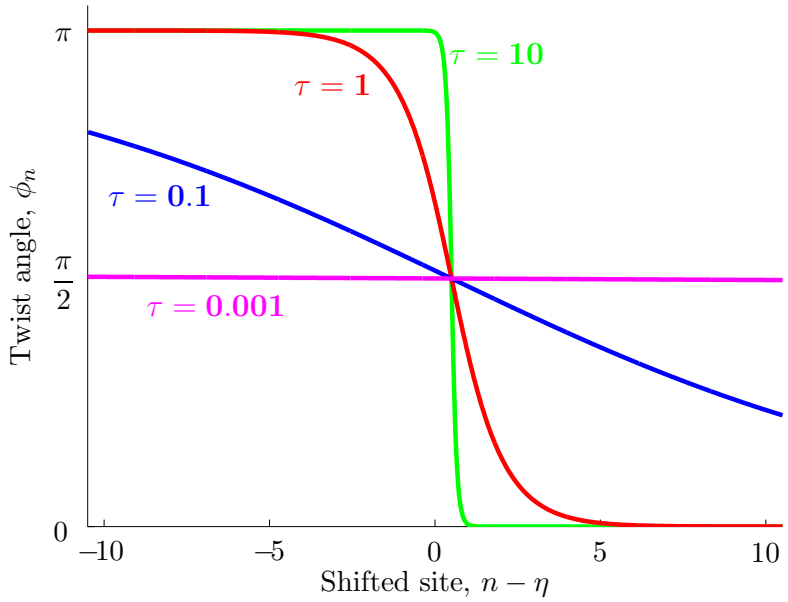

Figure 5.4: *The twist function, $\phi_n\,(n-\eta)$.*

We see that the change from twist angle $\phi = \pi$ to $\phi = 0$ happens faster for large values of τ. See also Fig. 5.5, which shows how ϕ is oriented to the z-axis at the center site.

We can now express the direction of the dipole moment at site n as

$$\mathbf{d}_n = \sin\phi_n \cdot \mathbf{n} + \cos\phi_n \cdot \mathbf{e}_z,$$

where $\mathbf{e}_z$ is the unit vector in the direction of the z axis. In coordinates, this amounts to

$$\boxed{\mathbf{d}_n = \left(-\sin\phi_n \frac{\kappa x_n}{\sqrt{1+\kappa^2 x_n^2}}, \sin\phi_n \frac{1}{\sqrt{1+\kappa^2 x_n^2}}, \cos\phi_n \right).} \quad (5.8)$$

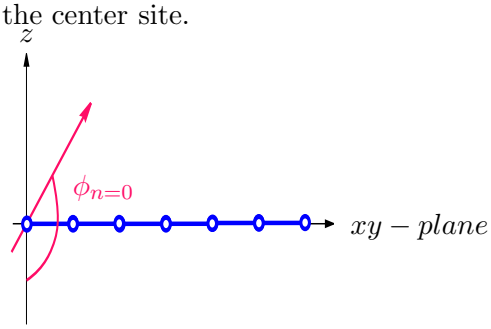

Figure 5.5: *The angle between the z-axis and the twist function, ϕ_n at $n = 0$.*

We note that $|\mathbf{d}_n| = 1$ as should be the case for unit dipoles.

The symmetry center, η, also appears in (5.7). Here, its effect is different from the placement of sites along the parabola chain: For $\eta = 0$, the symmetry lies *on* the site $n = 0$. This means that at this site, the twist function will have the value $\phi_{n=0} = \frac{\pi}{2}$. For strong twists ($\tau \to \infty$), the neighboring sites will tend towards π and 0, respectively. Thus the maximum change in twist angle is $\frac{\pi}{2}$ for the on-site case. On the other hand, in the intersite case $\eta = \frac{1}{2}$, the symmetry is *between* sites $n = 0$ and $n = 1$. This means that for strong twists, the angle between the dipole and the z-axis will be $\phi_0 = \pi$ for $n = 0$, but $\phi_1 = 0$ for $n = 1$ and thus a change in angle of π. See Fig. 5.6.

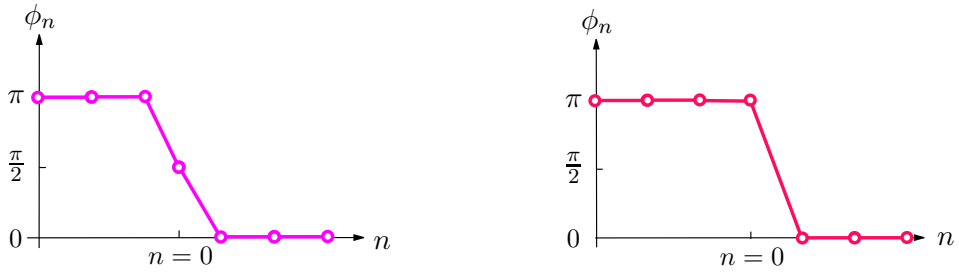

(a) On-site case, $\eta = 0$ (b) Intersite case, $\eta = \frac{1}{2}$

Figure 5.6: *The twist function, ϕ_n for the two different symmetry cases for $\tau \to \infty$.*

To sum up, we are looking at two different parabola chains with twisting dipole moments. The difference between the two is the placement of the axis of symmetry, which can be either *on* a chain site or *between* two. See Fig. 5.7, where we have tried to depict both curvature and twist for both chain configurations.

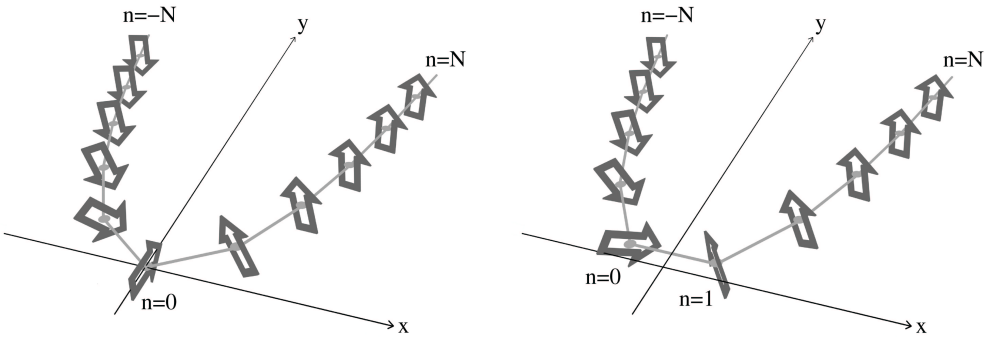

(a) On-site case, $\eta = 0$. (b) On-site case, $\eta = \frac{1}{2}$.

Figure 5.7: *DNA chain embedded on a parabola in the xy-plane. Sites (x_n, y_n) with $y_n = \frac{\kappa}{2} x_{n-\eta}^2$, indicated by light grey dots. Base pair dipoles, orthogonal to the parabola, shown as dark grey arrows. Curvature $\kappa = 2$ and twist $\tau = 2$. The z-axis (not shown) forms a right-handed system with x- and y-axes. Fig. (a) shows the on-site case, $\eta = 0$; Fig. (b) the inter-site case, $\eta = 1/2$.*

5.2 Long-range interaction in the twist model

The long-range dipole-dipole interaction can be investigated in a way similar to the one in Sec. 3.2. The setting is more complicated as we now have two different geometric features — the curvature, κ, and the twist, τ — as well as the two different chain configurations; the on-site and the intersite case.

We shall give a few examples of the outcomes. The following contour plots are constructed in a similar way as the ones in Fig. 3.4 on page 21. We use the same values for the contours, but now we have to consider both positive as well as negative terms. We use the same range of values — from 5×10^{-4} to 1, logarithmically spaced, but we also consider the same *negative* values now, together with the zero contour. We continue to use 25 lines in total; to make an example with only 11

contours, the values used would be $\{-1, -0.1, -0.01, -0.001, -0.0001, 0, 0.0001, 0.001, 0.01, 0.1, 1\}$. The color convention is also the same - but apart from the red color denoting attractive interaction, we also have a blue color to indicate repulsive interaction, as well as a green line, showing the zero contour line.

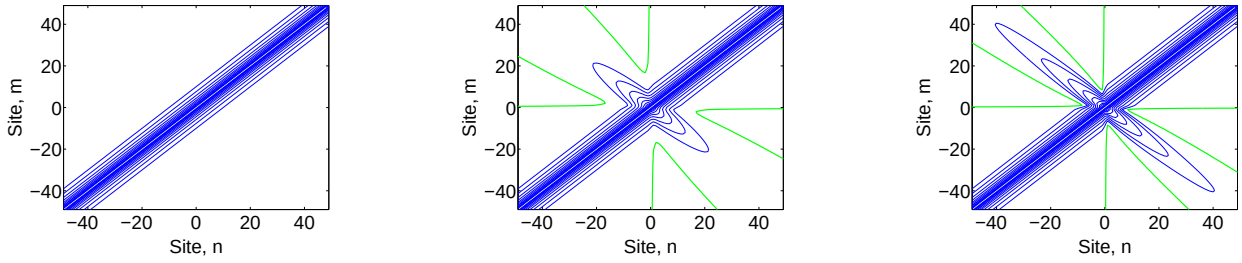

(a) $\kappa = 0.0$. (b) $\kappa = 1.0$. (c) $\kappa = 2.0$.

Figure 5.8: *Long-range interaction for the on-site chain for different curvatures, κ for a weak twist, $\tau = 10^{-6}$. 25 logarithmically spaced contours from -1 to 1. Red color denotes attraction, blue attraction and green the zero value contour.*

Parallel dipoles, $\tau = 10^{-6}$ We plot the result of a very weak twist, corresponding to virtually parallel dipoles in Fig. 5.8. We see that the straight chain ($\kappa = 0$) and weak twist $\tau = 10^{-6}$, depicted for the on-site case $\eta = 0$ in Fig. 5.8(a) corresponds to the straight wedge chain in Fig. 3.2(b) on page 19 — with one important difference: Now the interaction between the base pairs is *repulsive*, indicated by the blue color. For increasing degrees of curvature, we see that the sites in the center region begins to feel the effects from the other leg of the parabola and a shape similar to the ones in Fig. 3.4 appears. Also, the zero contour line appears, but no red contours are drawn, as the values are extremely small. The curvature of the chain together with the almost parallel dipoles in the bending plane gives an attractive (but in this case negligible) interaction. In contrast to the "wedge dipoles", which were modeled orthogonally to the wedge chain plane, the very low twist here corresponds to a twist angle $\phi = \frac{1}{2}$, which means that the dipoles lies *in* the chain plane.

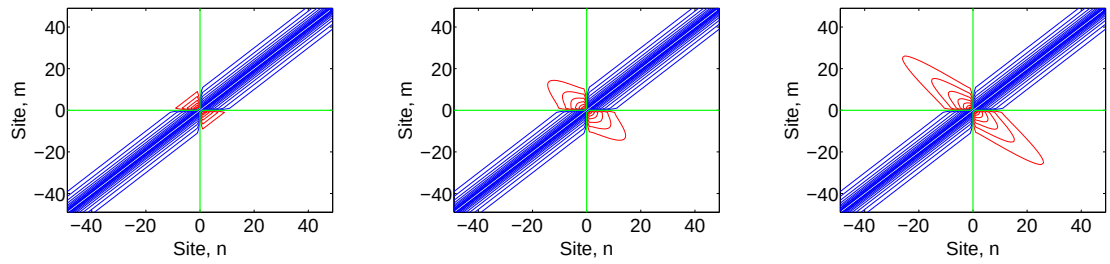

(a) $\kappa = 0.0$. (b) $\kappa = 1.0$. (c) $\kappa = 2.0$.

Figure 5.9: *Long-range interaction for the on-site chain for different curvatures, κ for a strong twist, $\tau = 10$. 25 logarithmically spaced contours from -1 to 1. Red color denotes attraction, blue attraction and green the zero value contour.*

"Domain wall" case, $\tau = 10$ Increasing the twist to a very large value, $\tau = 10$, result in a dipole configuration, where all dipoles in one half of the chain, $n < \eta$, are aligned almost parallel to the

z-axis, but the dipoles for $n > \eta$ are *anti*parallel to the z-axis. This is referred to as a *domain wall* at $n = \eta$ and it gives the result shown for the on-site case in Fig. 5.9. Since the chain in Fig. 5.9(a) is straight as it was in Fig. 5.8(a), the absolute value of the interaction is the same — the contour lines are at the same levels. But the interaction between sites on different legs of the chain is now *attracting* due to the antiparallel orientation describe above. Increasing the curvature increases the magnitude of the attracting interaction between the center sites.

Intermediate values For an intermediate value of the twist, $\tau = 0.2$, gives the result shown for the on-site case in Fig. 5.10. The plots in Figs. 5.10 and 5.11, which shows the LRI for constant

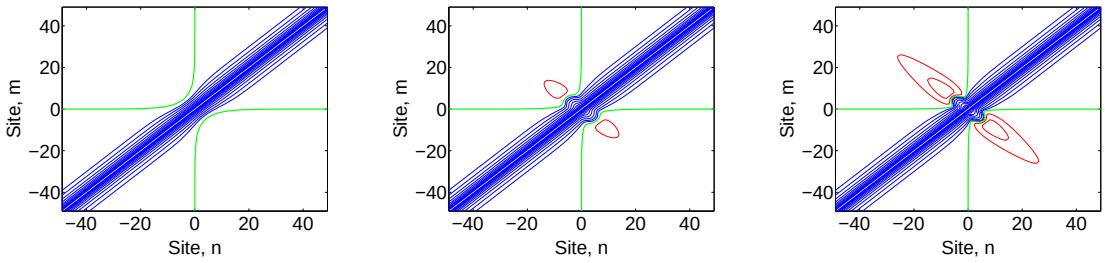

(a) $\kappa = 0.0$. (b) $\kappa = 1.0$. (c) $\kappa = 2.0$.

Figure 5.10: *Long-range interaction for the on-site chain for different curvatures, κ for an intermediate twist, $\tau = 0.2$. 25 logarithmically spaced contours from -1 to 1. Red color denotes attraction, blue attraction and green the zero value contour.*

intermediate curvature, are included to show that for intermediate values of twist and curvature, the picture is more complex. We see that both parameters play a role in determining the nature of the dipole-dipole interaction.

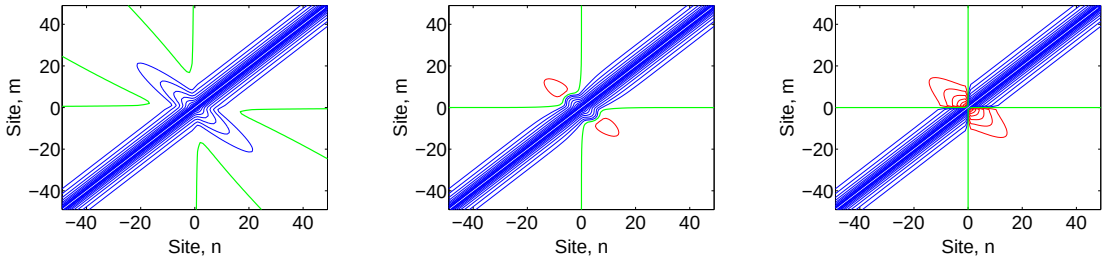

(a) $\tau = 10^{-6}$. (b) $\tau = 0.2$. (c) $\tau = 10$.

Figure 5.11: *Long-range interaction for the on-site chain for constant intermediate curvature, $\kappa = 1.0$ for different twists, τ. 25 logarithmically spaced contours from -1 to 1. Red color denotes attraction, blue attraction and green the zero value contour.*

5.2.1 Comparison between the two chain configurations

The plots in Figs. 5.8–5.11 are all made for the on-site symmetry case, $\eta = 0$. The qualitative appearance of the corresponding intersite case is very similar. To observe the difference, we consider the LRI profile at given sites — just as we did in Fig. 3.3 on page 20. Here, however, we show both sides of the chain and also the sign of the interaction — Fig. 3.3 only shows the magnitude of the then attractive interaction.

Fig. 5.12 shows profiles for the on-site case for $\tau = 10$ in a strongly curved chain, $\kappa = 2.0$. We recognize the strong contributions from neighboring sites at site $n = -2$ [Fig. 5.12(a)] (even though it here means a repelling interaction), but in this case, the dipole at $n = 0$ (m+2) always has a twist angle of $\phi_0 = \frac{\pi}{2}$. In the depicted case, the twist is strong, so the twist angle for $n \leq -1$ (m+1) is close to π. This means that the dipoles at sites $n = -3$ (m-1) and $n = -1$ (m+1) are almost parallel and their interaction is close to their maximal repelling value.

The dipole at $n = -1$ [Fig. 5.12(b)], however, experiences an attraction from site $n = +1$ (m+2) on the other side of the center site, corresponding to a negative value of J.

The center site [Fig. 5.12(c)] is in this case almost perpendicular to all other sites; therefore the interaction is almost zero. We note the symmetry: The case $n = -1$ and $n = -2$ correspond to the mirror image in $n = \eta$ of $n = 1$ and $n = 2$, respectively, and so on.

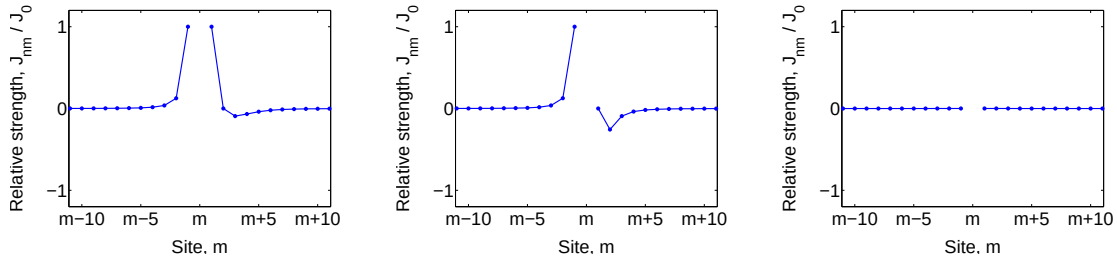

(a) $n = -2$ (b) $n = -1$ (c) $n = 0$

Figure 5.12: *Profiles of the dipole-dipole interaction for the on-site case for a chain with a strong twist, $\tau = 10$, corresponding to the domain wall case, with curvature $\kappa = 2.0$, at different sites. The figures correspond to cuts of Fig.5.9(c).*

In the intersite case $\eta = \frac{1}{2}$, depicted in Fig. 5.13, the center of symmetry is between sites $n = 0$ and $n = 1$. The case $n = -2$ [Fig. 5.13(a)] is very similar in both the on-site and intersite case, but the $n = -1$ case [Fig. 5.13(b)] has almost the same orientation as the previous one and so the interaction between sites $n = -1$ and $n = 1$ (m+1) is in this case close to J; not zero as in the on-site case [Fig. 5.12(b)]. For $n = 0$ [Fig. 5.13(c)], we see that the interaction to site $n = -1$ (m-1) is strongly repulsive, but strongly attractive to site $n = 1$ (m+1) on the other side of the symmetry center. Here, the symmetry is that site $n = 0$ is the mirror image of site $n = 1$, site $n = -1$ the mirror image of site $n = 2$ and so on.

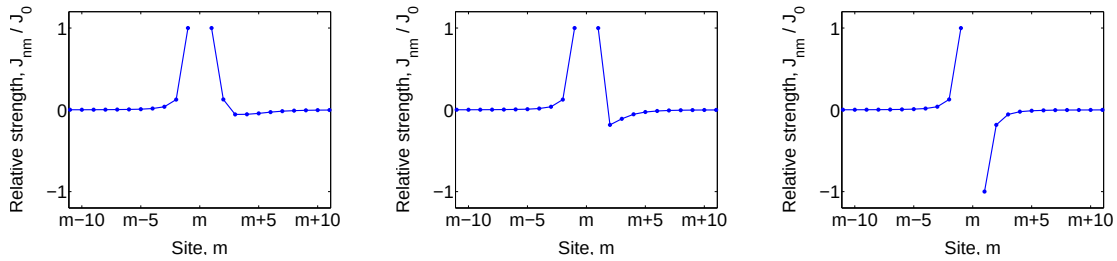

(a) $n = -2$ (b) $n = -1$ (c) $n = 0$

Figure 5.13: *Profiles of the dipole-dipole interaction for the intersite case for a chain with a strong twist, $\tau = 10$, corresponding to the domain wall case, with curvature $\kappa = 2.0$, at different sites. Compare to the on-site case of Fig. 5.12.*

5.3 Thermal dynamics on the twist chain

We consider exactly the same thermally generated initial conditions as we did in Sec. 4.1 and observe the effect of the more physiologically sound dipole moments.

Note that the considerations for the blow up effect in Sec. 4.2.1 on the dimer are also valid here, when considering strong twists. In the on-site case, though, we must also include some curvature to bring the next-to-center sites closer, as the twist between sites $n = \pm 1$ and $n = 0$ is $\frac{\pi}{2}$. But in contrast with the preliminary version of the dipole-dipole interaction, this "attracting dimer" limit is *only* applicable in the center region! Regardless of the twist, neighboring base pair dipoles are almost parallel in the far ends of the parabola chain and thus interacts repulsive and no blow ups occur. When the chain is twisted, the dipole-dipole interaction between sites at different legs of the chain may be formally attractive, but will be negligible due to the strong inversely dependence on distance.

Therefore, we do not expect a behavior as in the histograms Fig. 4.5. There, the attractive dipole-dipole interaction between *all* sites made it possible for the exponential increase of oscillation amplitude to occur everywhere, and the bending of the chain made it more probable that these blow ups would occur in the center region. Here, the exponential increase in base pair oscillation distance occurs *only* between the center sites with an overall attractive interaction! Namely at sites $n = 0$ and $n = 1$ in the intersite case and sites $n = -1$ and $n = 1$ in on-site case.

Essentially, we are now facing 3 different scenarios:

1. "Steady oscillations": oscillations with non-exponential amplitudes [inset (b) in Fig. 5.15 or (d) in Fig. 5.16].
2. "On-site blow up": blow up at site $n = -1$, $n = 0$, and $n = 1$ [inset (a) in Fig. 5.15].
3. "Intersite blow up": blow up at site $n = 0$ and $n = 1$ [inset (c) in Fig. 5.16].

Depending on the initial condition and the geometry, the system will oscillate in bounded fluctuations or evolve into an exponentially increasing amplitude. The on-site and intersite blow up cases occur only in the corresponding kind of chain. An example of Case 1 and 2 is shown in Fig. 5.14, in which the physical variables are noted. Using the same initial condition, the amplitude at the center site either stays bounded or increases exponentially. Here, the behavior is governed by the twist, but as we shall see, changing the curvature could also have the same effect.

In the "all attractive dipole interaction" model of Chapters 3 and 4, a blow up at a given site would spread to neighboring sites. In this model, the opening only affects a couple of base pairs, namely the ones fulfilling the prediction of the dimer case. For our parameter range, this means only sites $n = 0$ and $n = 1$ in the intersite case and sites $n = \{-1, 0, 1\}$ in the on-site case. This could change for stronger values of the curvature, because then the next-to-center sites would get closer; most prominently the on-site case. In the intersite case, the limiting case of infinity curvature will only bring sites $n = -1$ and $n = 2$ at a distance of 1, whereas $\kappa \to \infty$ in the on-site case corresponds to a chain collapse, *i.e.,* that the two legs coincide, sites at equal distance from the center will get infinitely close. This, by the way, corresponds

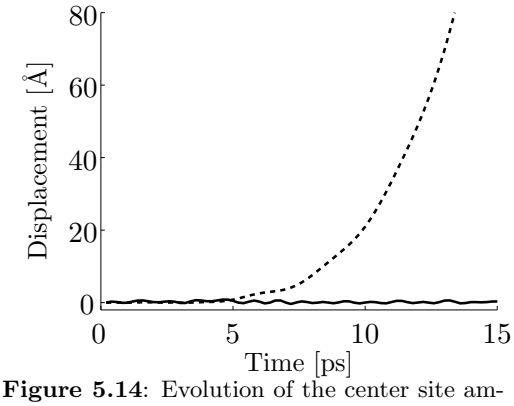

Figure 5.14: Evolution of the center site amplitude, u_0, for the same initial condition for curvature $\kappa = 1.0$ and twist $\tau = 4$ (solid curve) and $\tau = 6$ (dashed curve).

somewhat to a straight chain (of half length) with attractive dipole-dipole interaction at all sites, except that the magnitude of the interaction tends to infinity due to the distance dependence.

The lack of a blow up extending to a larger portion of the chain leads us to conclude that our model only describes a *precursor* for bubble generation.

In the following, we perform simulations with the 100 different realizations of the physiologically sound initial conditions, modeling thermal fluctuations. These are, the same 100 of for the simulations on the wedge chain (see one of them in Fig. 4.1). We let the simulations evolve for 100 time units (corresponding to about 20 picoseconds) and at the end we measure if the oscillation amplitude at any 2 neighboring sites (only the 3 center sites are relevant here, following the remarks above, but all sites are checked) has exceeded a threshold values of $u_n = 100$, corresponding to about 20 Å, *i.e.,* twice the equilibrium distance between base pairs.

We repeat the same set of initial conditions for various values of curvature and twist and refer to the set of simulations as a "bubble case" if at least one fulfils the requirement of at least 2 neighboring sites exceeding the amplitude threshold. The outcomes of the two chain configurations are discussed in the following.

5.3.1 Results for the on-site case

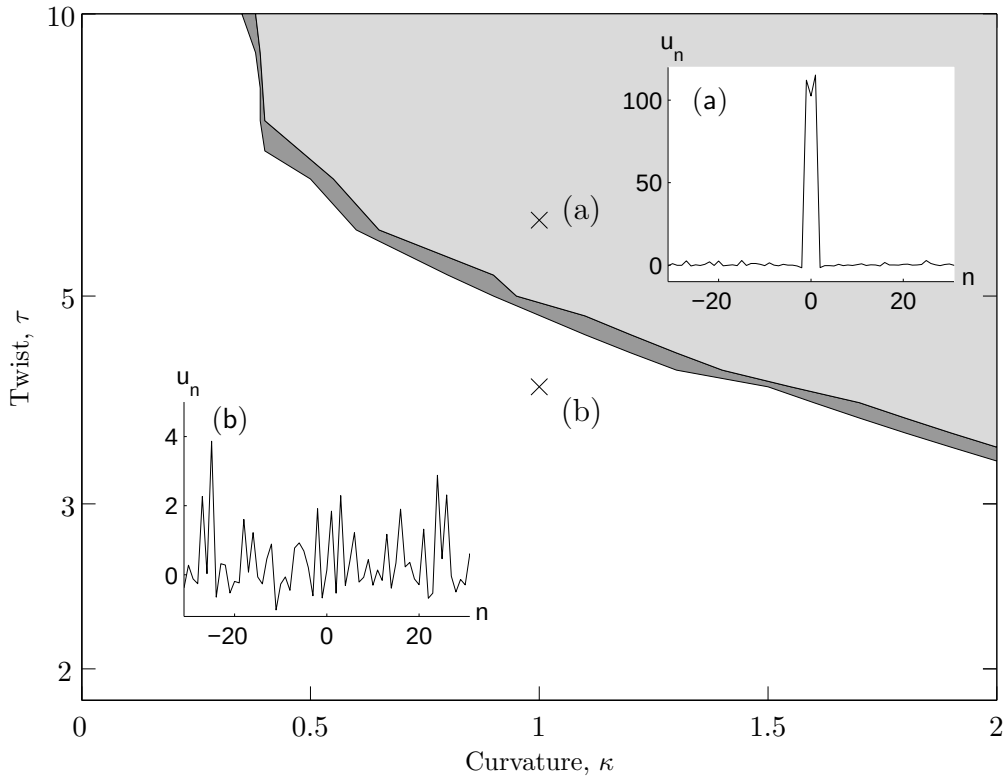

Figure 5.15: *Region of bubble generation in the on-site case. Light grey region: Bubble generation. Dark grey region: Transition region indicating the uncertainty of the simulations. White region: No bubble generation. Insets show the displacement, u_n, versus site, n, at the points (a) and (b) at simulation times (a) $t = 51$ and (b) $t = 100$ for the same initial condition.*

The result for the on-site chain figuration [Fig. 5.7(a)] is shown in Fig. 5.15, where the colored region corresponds to parameter values that exhibit bubble generation. We see that bubbles are generated for strong twist and strong curvature, which is expected. For the on-site case, the strongest attraction between dipoles occurs at the sites $n = -1$ and $n = 1$, which are almost antiparallel for strong twist. For smaller twists, the interaction is either not attracting or it is too weak. In the latter case, increasing the curvature brings attracting dipoles closer, increasing their interaction and spurs a bubble generation. This behavior is found in Fig. 5.15 for a constant twist of, say, $\tau = 5$. Even for strong twists, no bubbles are generated for small curvatures in the on-site case. In this case, the attracting dipole are at sites $n = -1$ and $n = 1$, and are thus separated by a distance of 2 lattice lengths on a straight chain. When the chain bends, however, the attracting sites are brought closer together and blow ups begin quickly to occur.

The exact shape of Fig. 5.15 depends on the chosen amplitude threshold — as well as system parameters[2] — but its qualitative shape is unchanged. Close to the region border, only a few of the simulations results in bubble generation, but this number increases as one proceeds in the direction of stronger twist and larger curvature (*i.e.,* towards the upper right corner). We note that for the on-site case the amplitude is increased at the 3 center sites $n = -1$, $n = 0$ and $n = 1$ as indicated in the inset (a).

[2]Some simulations have been performed with other dipole-dipole interaction strengths, J_0, but these are not presented here due to the lesser correspondence with the biology. As expected from the considerations in Sec. 4.2.1, a larger value of J_0 stimulates blow up. See also Chap. 6, where the dependence of mobility of a breather on the stacking and LRI parameters is investigated.

5.3.2 Results for the intersite case

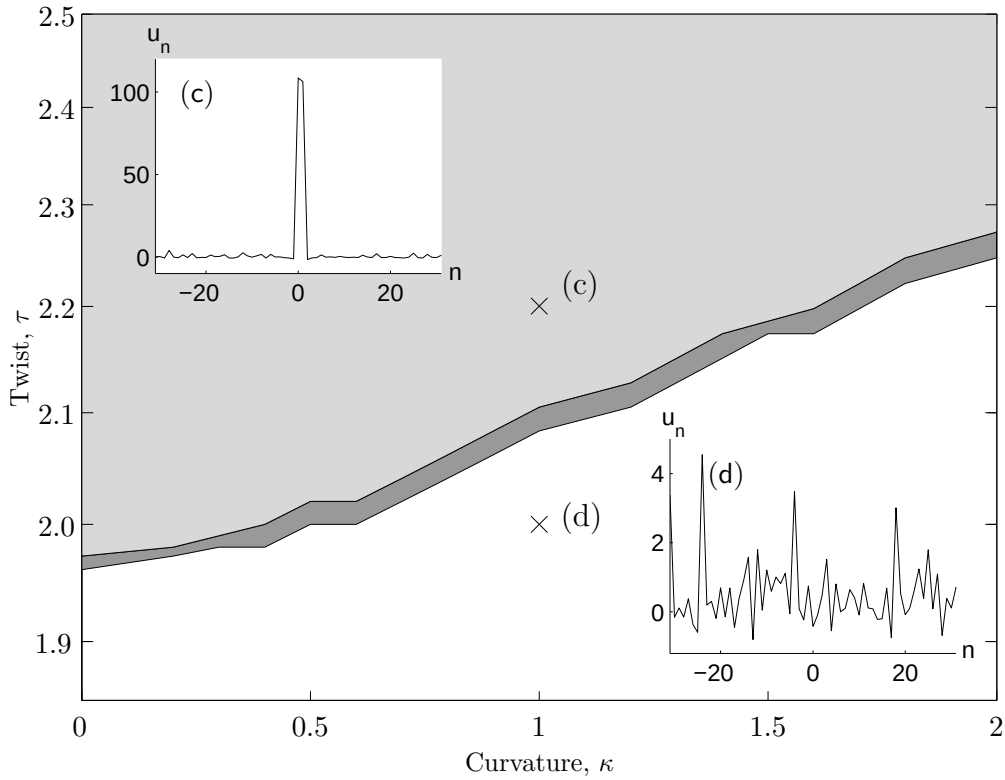

Figure 5.16: *Region of bubble generation in the intersite case. Light grey region: Bubble generation. Dark grey region: Transition region indicating the uncertainty of the simulations. White region: No bubble generation. Insets show the displacement, u_n, versus site, n, at the points (c) and (d) at simulation time (c) $t = 45$ and (d) $t = 100$ for the same initial condition.*

In the intersite case, Fig. 5.16, the picture is different. First of all, the twist needed for bubble generation is smaller and blow ups are initiated for twists of about 2. Secondly, the dependence on the curvature is less pronounced. This is because it is *neighboring* dipoles, that for strong twist are anti-parallel and thus attracting each other. Since, in the framework of our model, the chain has constant distance between adjacent sites, increasing the curvature does not increase the tendency for bubbles to be generated. This is in contrast to the on-site case, Fig. 5.15.

In fact, the opposite is the case: As the dipole twist is perpendicular to the chain, increasing the curvature has the consequence that the center dipoles interact in a less attracting way. Even though sites $n = 0$ and $n = 1$ have a fixed distance, the dipole-dipole interaction still changes with curvature. This is due to the fact that dipoles are perpendicular to the chain, so when the chain shape is altered due to changed curvature, so is the dipole orientation.

Note that in this case, the displacement at the two center cites, $n = 0$ and $n = 1$, is increased as the inset (c) shows. Close to the region border, the number of simulations resulting in bubble generation is small, but it increases as one increases the twist or decreases the curvature (*i.e.,* moves towards the upper left corner).

5.4 Effective potential for the twist chain

It is obvious that having initially randomly distributed energy along the chain, successful bubble generation should include, as a first stage, funneling of energy in the bent and twisted region. Therefore we can expect that only in the case when this region acts as a potential well, bubbling may occur. The behavior found in Figs. 5.15 and 5.16 can be qualitatively explained by the effective on-site potential, $V_n = \sum_{m \neq n} J_{nm}$, already presented in (4.6) on page 27. We consider the dipole potential at given sites for both the on-site and the intersite case for constant curvature, $\kappa = 1.0$, with respect to the "ground state" at $n \to \pm\infty$. Fig. 5.17 shows the difference in

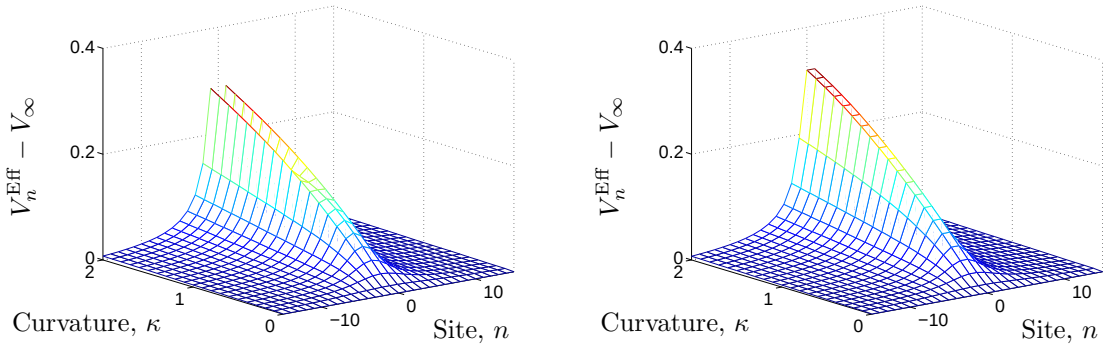

(a) On-site case. (b) Intersite case.

Figure 5.17: *Effective "ground state" potential, $V_n^{\mathrm{Eff}} - V_\infty$ with untwisted chains, $\tau \to 0$, for different curvatures, κ.*

curvature dependence for the untwisted versions of the two parabolic chain configurations. The on-site case has a single maximal value at $n = 0$, whereas the intersite has two. All values are positive, corresponding to repulsion, as it should be for the parallel dipoles. For the straight chain ($\kappa = 0$), the long-range interaction is identical at all chain sites and as the chain curves, the interaction between the next-to-center sites increases. This is much like the case of the wedge chain, Fig. 4.3(b), but with the opposite sign of interaction. These are compared in Fig. 5.18.

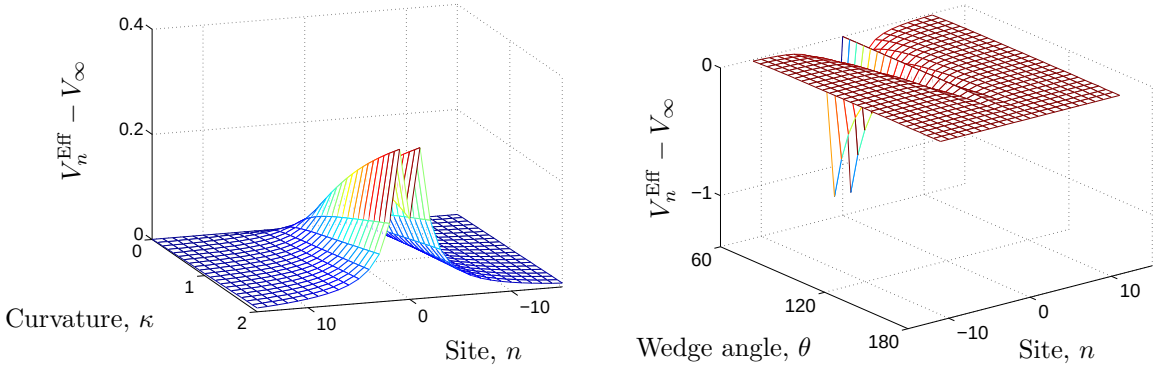

(a) On-site case. (b) Wedge case.

Figure 5.18: *Comparison of the effective "ground state" potential, $V_n^{\mathrm{Eff}} - V_\infty$ for untwisted chains. Fig. (a) is the same as Fig. 5.17, but from a different angle, emphasizing the double-well potential. Fig. (b) is the wedge chain from Fig. 4.3 on page 27.*

In Fig. 5.18 the no twist case is compared to the previously considered wedge case [Fig. 4.3(b)]. First of all, we see that the sign is opposite, as it should be, but we also notice the difference that arises from the parallel dipole orientation. In the wedge case, the dipoles are parallel to the bending plane, but for the parabola with no twist, the parallel dipoles are aligned *in* the bending plane. This explains the main difference between Fig. 5.18(a) and (b) [remember, of course, that the chain in (a) is parabolic, while the chain in (b) is wedge shaped].

Fig. 5.19 shows the effect of twist in straight versions of the two parabolic chain configurations. We see how the twist changes the interaction to attractive in the center region. Again, there is only one site of maximal interaction in the on-site case, but two in the intersite one. This seemingly modest difference plays a role in the difference in the generation of blow ups in the on-site and intersite cases (Figs. 5.15 and 5.16).

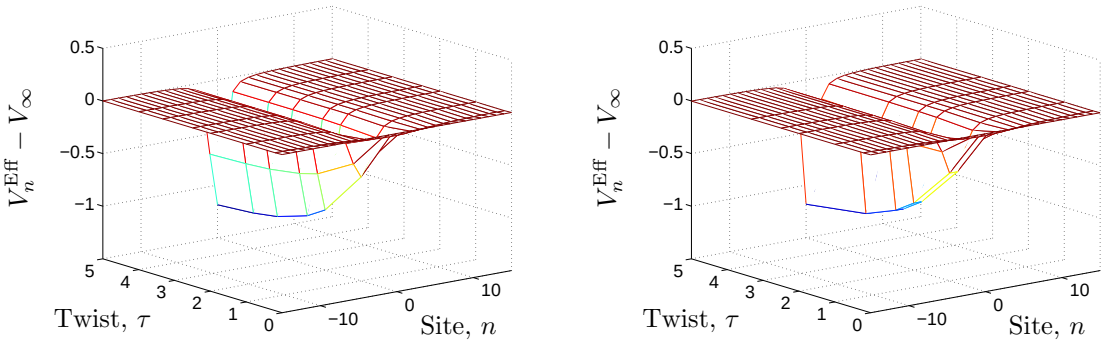

(a) On-site case.

(b) Intersite case.

Figure 5.19: *Effective "ground state" potential,* $V_n^{\mathrm{Eff}} - V_\infty$ *for straight chains,* $\kappa = 0$*, for different twists.*

The combined effect of both twist and curvature is shown in Figs. 5.20 and 5.21. Thus, Figs. 5.20 depicts the depth of the potential well for constant curvature for both the on-site [Fig. 5.20(a)] and the intersite [Fig. 5.20(b)] case. Interestingly, the effective potential is repulsive without any twist, but increasing τ drives the interaction to be attractive. We see that in the vicinity of the bending point, there exist an effective potential well for τ larger than about 0.5. This corresponds to the behavior found in Figs. 5.15 and 5.16, where no blow ups are found for τ smaller than roughly 5 and 2, respectively. That the values does not coincide precisely is because the existence of a potential well is a necessary, but not sufficient, condition for bubble generation (notice for example how the attractive interaction for $\kappa = 0$ in Fig. 5.19(a) is not sufficient to generate any blow ups). The depth of the potential well increases with increasing twist, until a saturation is reached at $\tau \approx 5$.

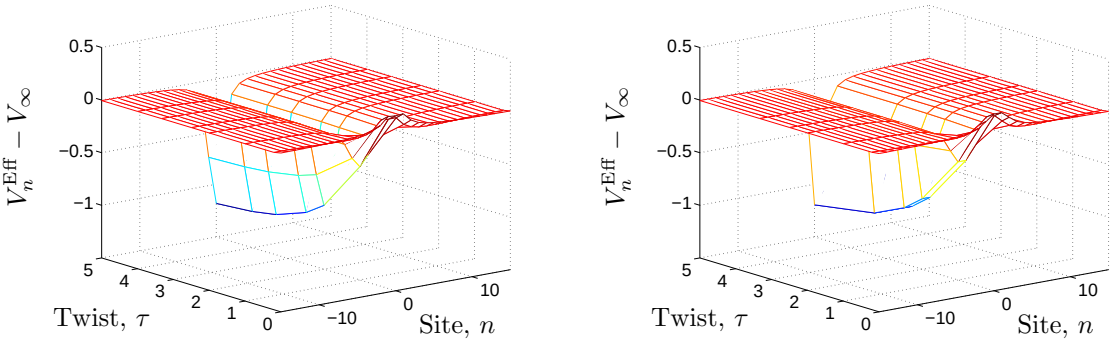

(a) On-site case. (b) Intersite case.

Figure 5.20: *Effective "ground state" potential, $V_n^{\mathrm{Eff}} - V_\infty$ with curvature $\kappa = 1.0$ and for various twists, τ, in the two chain configurations.*

For constant twist, Fig. 5.21, the situation is much more dominated by the twist than the curvature. For the on-site case with $\tau = 5$ [Fig. 5.21(a)], we see a decreasing potential well depth with increasing curvature at sites $n = -1$ and $n = 1$, whereas the potential at $n = 0$ is almost constant. Interestingly, the effective potential at $n = 0$ *increases* very slightly with increasing twist, but the overall outcome is still an effective potential well.

In the intersite case [Fig. 5.21(b)], the twist is fixed at $\tau = 2$. We see again that the depth of the potential well increases with increasing curvature at the center sites $n = 0$ and $n = 1$, but this time a bit stronger. The potential at $n = -1$ and $n = 2$ descreases, but not as much as in the on-site case. For the depicted values, the overall effect of curvature is to prevent blow up. Therefore, bubble generation is not found for larger curvature in the intersite case, corresponding to the behavior seen in Fig. 5.16.

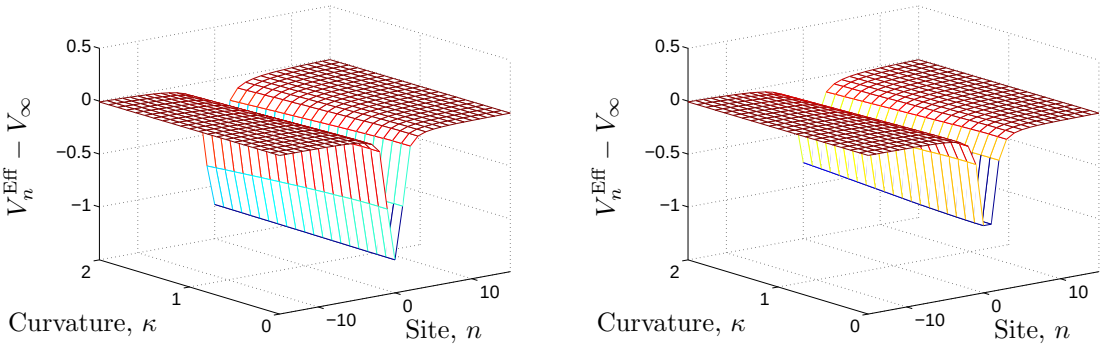

(a) On-site case, $\tau = 5$. (b) Intersite case, $\tau = 2$.

Figure 5.21: *Effective "ground state" potential, $V_n^{\mathrm{Eff}} - V_\infty$ with untwisted chains, $\tau \to 0$, for different curvatures, κ.*

We see that both curvature and twisting play a role in the localized formation of precursors for denaturation bubbles in our model of the DNA molecule and it is clear that the chain configuration is important. The many figures here have been included to emphasize the similarities and differences between the on-site and intersite model. At a first glance, the effective potentials of the on-site and intersite chain configurations, depicted in Figs. 5.17–5.21, seem qualitatively identical but nevertheless there are differences, which account for the difference in the "master"

plots Figs. 5.15–5.16.

Stronger twist increases the initiation of bubble generation in both cases considered. The effect of increasing curvature is different: in the on-site case, curvature clearly enhances bubble generation, but in the intersite case it slightly decreases the formation of bubbles in the range of κ considered.

6

Another note on moving breathers — The interface model

One may wonder if moving breathers are supported in a molecular chain where the dipoles are better described that the overall attracting interaction, as discussed in Chapter 3. To this end, investigations have been made on moving breathers in a so-called *interfaced* DNA molecular model [69]. We are considering a straight molecule, with dipole moments being either parallel or antiparallel to one another. The Hamiltonian considered is

$$\overline{H} = \sum_{n=1}^{N} \left(\frac{1}{2} m \dot{\overline{u}}_n^2 + D \left(e^{-b\overline{u}_n} - 1 \right)^2 + \frac{1}{2} \overline{\varepsilon} \left(\overline{u}_{n+1} - \overline{u}_n \right)^2 + \frac{1}{2} \overline{\mu} \sum_{p \neq n} J_{n,n+p} \overline{u}_{n+p} \overline{u}_n \right), \tag{6.1}$$

with the dipole-dipole interaction term

$$J_{n,n+p} = \frac{\alpha_{n,n+p}}{|p|^3}. \tag{6.2}$$

Basically, it is the same system as we have been considering all along, except that we also have a strength parameter, $\overline{\mu}$, to the dipole-dipole interaction term and the scaling is slightly different. This corresponds to J_0 in Sec. 2.1.1, as well as the strength of the stacking term, $\overline{\varepsilon}$, is denoted C in Sec. 2.1.1. This work is reported in [69] and the notation and scalings has been adopted for this final Chapter of Part I.

We transform the physical quantities (indicated with a bar) to dimensionless with the scalings

$$t = \omega_0 \overline{t}, \quad u_n = b\overline{u}_n, \quad \varepsilon = \frac{\overline{\varepsilon}}{m\omega_0^2}, \quad \mu = \frac{\overline{\mu}}{m\omega_0^2}, \quad \text{and} \quad H = \frac{\overline{H}}{2D},$$

where $\omega_0 = \sqrt{\frac{2b^2 D}{m}}$, the frequency of of an isolated DNA base pair oscillator, becomes unity in the scaled system.

As initial conditions we do not use a Gaussian in this case, but rather evolve numerically a single site distortion to the amplitude, $u_m = \lambda$, $u_{n \neq m} = 0$, until a stationary breather is obtained.

We are considering a molecular chain in which the dipoles in one half are parallel to each other, but antiparallel to the dipoles in the other half of the chain, see Fig. 6.1.

Figure 6.1: *The model piecewise interfaced chain.*

Instead of the free boundary conditions (2.12) and (2.12) used previously, we are using periodic boundary conditions. But to avoid having 2 interfaces, we shape the numerical chain as a kind of a Möbius band, so that the dipoles at the ends are parallel as well. Details are found in [69].

Moving breathers

By perturbing the initial stationary breather (numerically obtained from the $u_m = \lambda$ Ansatz) with a translational energy of magnitude λ we are able to generate a moving breather, provided that the coupling between adjacent sites is strong enough. We use a "kick" at the next-to-center sites:

$$\dot{u}_{m-1} = -v \quad \text{and} \quad \dot{u}_{m+1} = +v, \tag{6.3}$$

where the velocity, v, fulfills $\frac{1}{2}\lambda^2 = \frac{m^*}{2}v^2$, m^* being the effective mass of the moving breather.

For parameter values stacking $\varepsilon = 0.129$, dipole-dipole term $\mu = 0.02$, and breather frequency $\omega_b = 0.8$, we observe different behavior depending on a threshold value of the kinetic energy, λ_c.

For smaller values, $\lambda < \lambda_c$ a *trapping regime* is found on the chain configuration in Fig. 6.1. This means that the incoming breather is trapped in a region around the interface, see Fig. 6.2(a).

For larger values, $\lambda > \lambda_c$ a *transmission regime*, where the breather passes through the interface region, is found, see Fig. 6.2(b). We conclude that moving breathers are supported with repulsive,

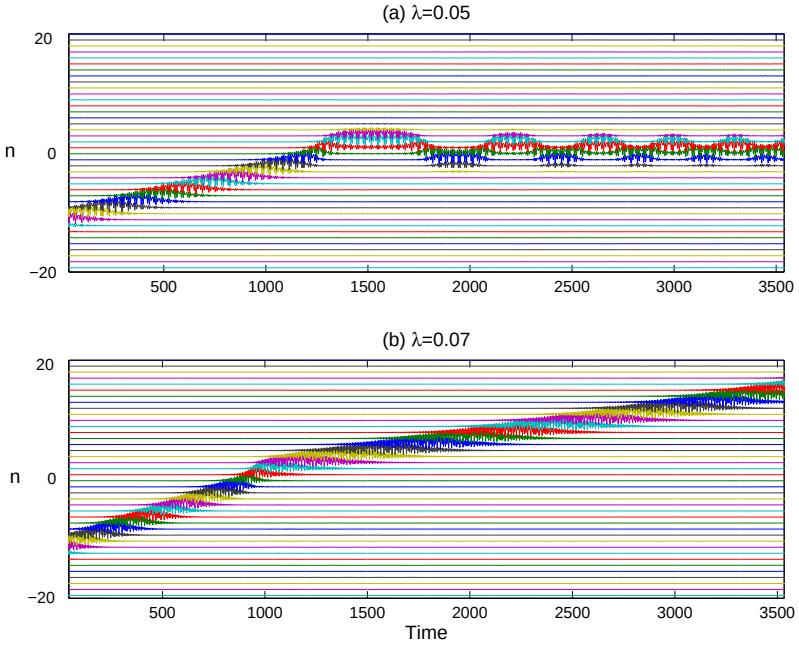

Figure 6.2: *Examples of trapping and transmission. In both cases,* $\mu = 0.002$ *and* $\varepsilon = 0.129$. *The interface is between sites 0 and 1.*

parallel dipoles. Compare also to Fig. 3.6 on page 22. We see that qualitatively similar effects exist for both expressions for the dipole-dipole interaction.

We note that similar results were obtained using the chain geometries depicted in Fig.6.3. No simulations were conducted with other chain geometries than the straight one.

Figure 6.3: *Single inverted dipole chain.*

Effective potential

Also in this case, an effective potential is calculated; slightly modified due to the difference in scalings:

$$V_n^{\mathrm{Eff}} = \frac{1}{2}\mu \sum_{m \neq n} J_{n,m}, \tag{6.4}$$

which is depicted in Fig. 6.4 for both the interfaced piecewise and the single inverted dipole system. We note a symmetry similar to the on-site and intersite potentials of Sec. 5.4. In the "domain wall"-case (solid circles), we see a symmetry between sites 0 and 1, corresponding to the intersite case. In the case of a single inverted dipole (open circles), we have symmetry center at $n = 0$. Also, the potential for the single inverted dipole is lower due to the attractive interaction from *both* of its two neighboring sites — in the domain wall case only of the neighbors are attracting.

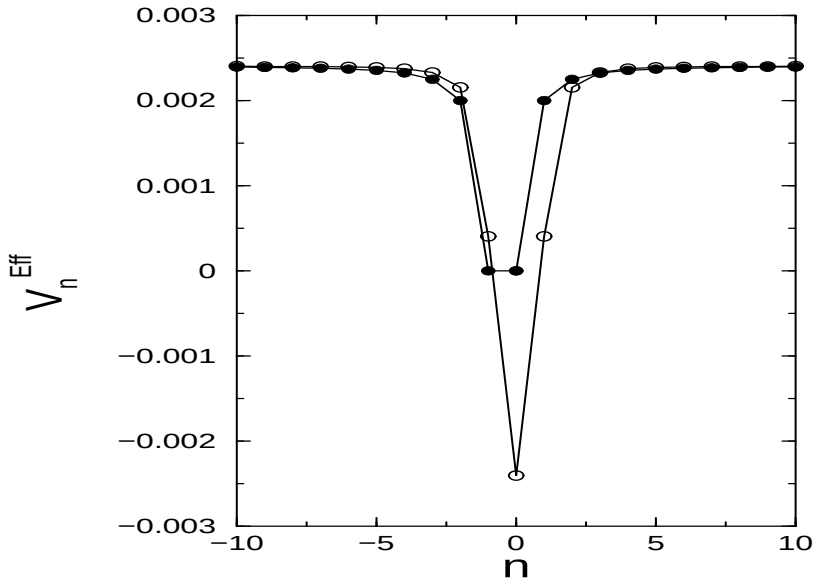

Figure 6.4: *Effective potential V_n^{Eff}, versus site number, n, for the interfaced piecewise system (dots) and for the single inverted dipole system (open circles).*

Critical value of λ

A critical value of the initial perturbation for different μ and ε is found through a series of simulations, displayed in Fig. 6.5. We see that for a given value of the dipole-dipole interaction strength, the tendency for trapping to occur increases with increasing value of the stacking potential, μ. Larger values of λ_c means a larger window for trapping to occur: $\lambda < \lambda_c$. For a fixed value of the stacking strength, λ_c increases with increasing dipole-dipole interaction, μ. The tendency is most pronounced for smaller values of ε, in which case the strength of the dipole-dipole interaction is relatively larger than the stacking interaction.

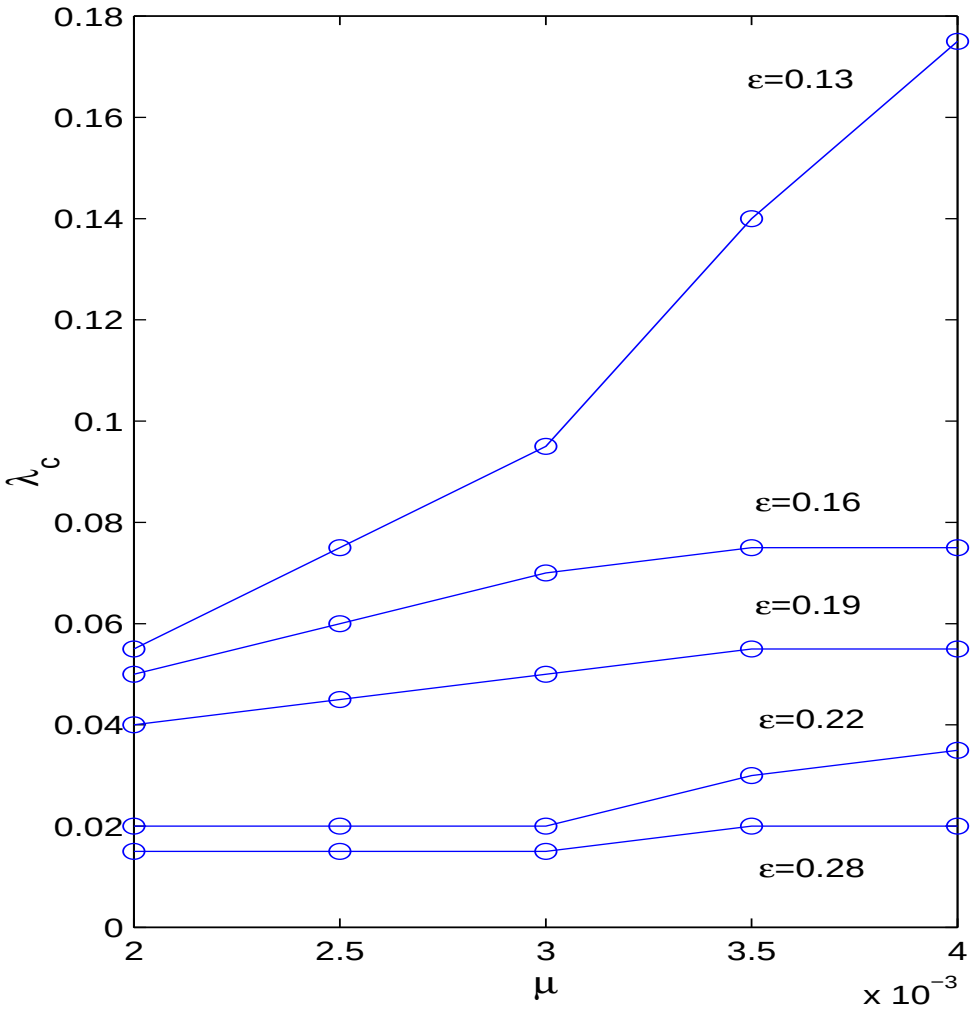

Figure 6.5: *Dependence of the critical value of initial velocity perturbation, λ_c with the dipole-dipole strength $\mu = 0.002$ for different values of the stacking strength, ε.*

Multiple breather interaction

Finally, multiple breather interactions have also been considered in the interface model in exactly the same way as in Sec. 3.3.1. With a given choice of initial translational kinetic energies, λ (the "kick"), we get the result in Fig. 6.6.

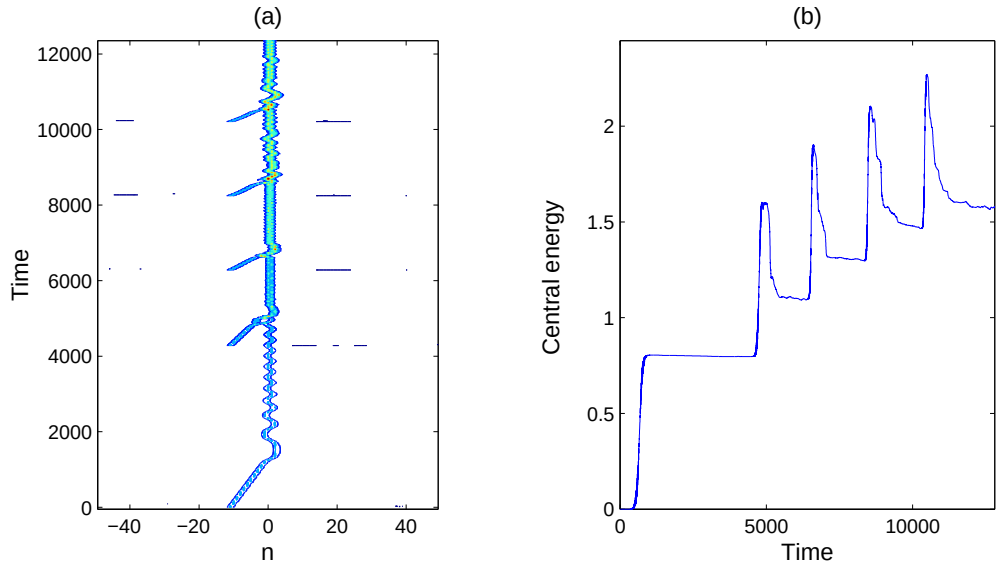

Figure 6.6: *(a) Contour plots for the evolution of five breathers launched towards the interface with different translational kinetic energies. The breathers are trapped at the interface increasing the accumulated energy density ($\lambda = 0.05; 0.07; 0.15; 0.19; 0.2$). (b) Time evolution of the central energy.*

Compare with Fig. 3.9 on page 24. As expected, the multiple trapping effect appears here as well. We note that the saturation effect seems to be slower with the present formulation.

7
Conclusion

We have investigated a bent chain of Morse oscillators and find that moving discrete breathers may be trapped at a bending point in the presence of a preliminary dipole-dipole-like long-range interaction. Thus the role of the geometry for the dynamics is analogous to that of an inhomogeneity, but here it is present in an intrinsically homogeneous chain. At the bending point, several incident discrete breathers may be trapped. However, energy is lost to radiation and a saturation effect seems to limit the total trapped energy in the vicinity of a given bending point.

For random initial conditions modeling thermal fluctuations, we observe an unbounded growth of oscillation amplitude. This blow up behavior is analytically supported. The tendency for blow up in the vicinity of the bending point is substantially amplified with increasing bending. Thus energy localization is implied in this region which therefore acts as an energy funnel.

The use of a nonlinear potential is crucial for obtaining the energy funneling effect in our model, since no amplitude growth is observed in a linear approximation. The plateau of the characteristic Morse potential allows for the breaking of the hydrogen bonds, e.g., in the molecule to be modeled. In contrast, a linear approximation with a parabolic potential produces too powerful an attraction for this effect to take place and would therefore not be an adequate description of chemical bonds.

We also note that the attracting nature of the long–range interaction is crucial for the occurrence of amplitude growth. This is further investigated with a more accurate dipole-dipole interaction term. We have shown that bubble generation in DNA-like models can be initiated by curvature and twist of the molecular strands.

Stronger twist facilitate bubble generation, whereas the effect of curvature depends on the details of the geometry. For the on-site case, with the axis of symmetry lying *on* a chain site, increasing curvature increases the tendency for bubble generation. Conversely, the intersite case (with symmetry *between* two chain sites) decreases bubble generation for increasing curvature.

Bubbles emerge in the region of maximal twist and curvature, and are found at physiological temperatures and with widely used parameter values for DNA.

Also, moving breathers were investigated with an interface dipole configuration. We find that also in this case, moving breathers are supported, and effects such as collision, trapping, and saturation are observed as well and the outcome of changing some of the parameters is investigated.

Bibliography

[1] J. D. Watson and F. H. C. Crick. A structure for deoxyribose nucleic acid. *Nature*, 171:737–738, April 1953.

[2] C.R. Calladine and H.R. Drew. *Understanding DNA*. Academic Press, London, 2002.

[3] W. Saenger. *Principles of Nucleic Acid Structure*. Springer Verlag, New York, 1984.

[4] L.V. Yakushevich. *Nonlinear Physics of DNA*. Wiley, New York, 1998.

[5] C. Reiss. In *Nonlinear excitations in biomolecules,* edited by M. Peyrard. Springer, Les Ulis, 1994.

[6] L.V. Yakushevich. Nonlinear DNA dynamics: hierarchy of the models. *Physica D: Nonlinear Phenomena*, 79(1):77–86, February 1994.

[7] N. Korzheva, A. Mustaev, M. Kozlov, A. Malhotra, V. Nikiforov, A. Goldfarb, and S.A. Darst. A structural model of transcription elongation. *Science*, 289(5479):619–25, 2000.

[8] K S Murakami, S Masuda, E A Campbell, O Muzzin, and S A Darst. Research - research articles - structural basis of transcription initiation: An rna polymerase holoenzyme-dna complex. *Science : International Edition - AAAS*, 296(5571):1285–1289, 2002.

[9] Thierry Dauxois, Michel Peyrard, and A. R. Bishop. Dynamics and thermodynamics of a nonlinear model for DNA denaturation. *Physical Review E*, 47(1):684, January 1993.

[10] Maria Barbi, Simona Cocco, Michel Peyrard, and Stefano Ruffo. A twist opening model for DNA. *Journal of Biological Physics*, 24(4):97–114, 1999.

[11] Kyle Forinash, Michel Peyrard, and Boris Malomed. Interaction of discrete breathers with impurity modes. *Physical Review E*, 49(4):3400–3411, April 1994.

[12] Julian J. L. Ting and Michel Peyrard. Effective breather trapping mechanism for DNA transcription. *Physical Review E*, 53(1):1011–1020, January 1996.

[13] I. Bena, A. Saxena, G. P. Tsironis, M. Ibanes, and J. M. Sancho. Confinement of discrete breathers in inhomogeneously profiled nonlinear chains. *Physical Review E*, 67:037601, 2003.

[14] Kyle Forinash, Thierry Cretegny, and Michel Peyrard. Local modes and localization in a multicomponent nonlinear lattice. *Physical Review E*, 55(4):4740–4756, April 1997.

[15] J. Cuevas, F. Palmero, J. F. R. Archilla, and F. R. Romero. Moving discrete breathers in a klein-gordon chain with an impurity. *Journal of Physics A: Mathematical and General*, 35(49):10519–10530, December 2002.

[16] Mario Techera L. L. Daemen and E. W. Prohofsky. Analysis of a nonlinear model for the DNA double helix: Energy transfer in an inhomogeneous chain. *Physical Review A*, 42(2):1008–1011, July 1990.

[17] Mario Salerno. Discrete model for DNA-promoter dynamics. *Physical Review A*, 44(8):5292–5297, October 1991.

[18] Terence Hwa, Enzo Marinari, Kim Sneppen, and Lei han Tang. Localization of denaturation bubbles in random DNA sequences. *Proceedings of the National Academy of Sciences of the United States of America*, 100(8):4411–4416, April 2003.

[19] Grégoire Altan-Bonnet, Albert Libchaber, and Oleg Krichevsky. Bubble dynamics in double-stranded DNA. *Physical Review Letters*, 90:138101, April 2003.

[20] S Ares, N K Voulgarakis, K O Rasmussen, and A R Bishop. Condensed matter: Structure, etc. - bubble nucleation and cooperativity in dna melting. *Physical Review Letters*, 94(3):35504–35700, 2005.

[21] G Kalosakas, K O Rasmussen, A R Bishop, C H Choi, and A Usheva. Sequence-specific thermal fluctuations identify start sites for dna transcription. *Europhysics Letters*, 68(1):127–133, 2004.

[22] K.O. Rasmussen, G. Kalosakas, N.K. Voulgarakis, A.R. Bishop, C.H. Choi, and A. Usheva. Thermally induced coherent vibrations in DNA. *Fluctuations and Noise in Biological, Biophysical, and Biomedical Systems II and Proceedings of SPIE - The International Society for Optical Engineering*, 5467:235–241, 2004.

[23] K.K. Voulgarakis, G. Kalosakas, K.O. Rasmussen, and A.R. Bishop. Temperature-dependent signatures of coherent vibrational openings in dna. *Nano Letters*, 4(4):629–32, 2004.

[24] Chu H. Choi, George Kalosakas, Kim Œ. Rasmussen, Makoto Hiromura, Alan R. Bishop, and Anny Usheva. DNA dynamically directs its own transcription initiation. *Nucleic Acids Research*, 32(4):1584–1590, 2004.

[25] Fei Zhang, Michael A. Collins, and Yuri S. Kivshar. Kinks and conformational defects in nonlinear chains. *Physical Review E*, 51(3):3774–3777, April 1995.

[26] A.S. Davydov. *Solitons in Molecular Systems*. D. Reidel, Dordrecht, 1985.

[27] A. Scott. Davydov's soliton. *Physics Reports*, 217(1):1–67, 1992.

[28] S. Flach and C. R. Willis. Discrete breathers. *Physics Reports*, 295(5):181, 1998.

[29] A.J. Heeger, S. Kivelson, J. R. Schrieffer, and W.-P. Su. Solitons in conducting polymers. *Reviews of Modern Physics*, 60(3):781–850, 1988.

[30] O. Bang and M. Peyrard. High order breather solutions to a discrete nonlinear klein-gordon model. *Physica D: Nonlinear Phenomena*, 81(1-2):9–22, February 1995.

[31] Ole Bang and Michel Peyrard. Generation of high-energy localized vibrational modes in nonlinear klein-gordon lattices. *Physical Review E*, 53(4):4143–4152, April 1996.

[32] Thierry Dauxois and Michel Peyrard. Energy localization in nonlinear lattices. *Physical Review Letters*, 70(25):3935–3938, June 1993.

[33] V. Muto, A. C. Scott, and P. L. Christiansen. A toda lattice model for DNA: thermally generated solitons. *Physica D: Nonlinear Phenomena*, 44(1-2):75–91, 1990.

[34] V. Muto, A. C. Scott, and P. L. Christiansen. Thermally generated solitons in a toda lattice model of DNA. *Physics Letters A*, 136(1-2):33–36, 1989.

[35] V. Muto. Anharmonic models for DNA dynamics. *Nanobiology*, 1(3):325–334, 1992.

[36] K.Ø. Rasmussen, S. Aubry, A.R. Bishop, and G.P. Tsironis. Discrete nonlinear schrodinger breathers in a phonon bath. *The European Physical Journal B*, 15(1):169–175, 2000.

[37] K.Ø. Rasmussen, A.R. Bishop, and N. Gronbech-Jensen. Creation and annihilation of intrinsic localized excitations. *Physical Review E (Statistical Physics, Plasmas, Fluids, and Related Interdisciplinary Topics)*, 58(1):R40–3, 1998.

[38] Michel Peyrard. The pathway to energy localization in nonlinear lattices. *Physica D: Nonlinear Phenomena*, 119(1-2):184–199, August 1998.

[39] G. P. Tsironis, A. R. Bishop, A. V. Savin, and A. V. Zolotaryuk. Dependence of thermal conductivity on discrete breathers in lattices. *Physical Review E*, 60(6):6610–6613, December 1999.

[40] T. Dauxois, M. Peyrard, and C. R. Willis. Localized breather-like solution in a discrete klein-gordon model and application to DNA. *Physica D: Nonlinear Phenomena*, 57(3-4):267–282, 1992.

[41] Alessandro Campa. Bubble propagation in a helicoidal molecular chain. *Physical Review E*, 63(2):021901, February 2001.

[42] J. Cuevas, J. F. R. Archilla, Yu. B. Gaididei, and F. R. Romero. Moving breathers in a DNA model with competing short- and long-range dispersive interactions. *Physica D: Nonlinear Phenomena*, 163(1-2):106, March 2002.

[43] Leonor Cruzeiro-Hansson. Effect of long range and anharmonicity in the minimum energy states of the davydov-scott model. *Physics Letters A*, 249(5-6):465–473, December 1998.

[44] Maria Barbi, Simona Cocco, and Michel Peyrard. Helicoidal model for dna opening. *Physics Letters A*, 253(5-6):358–369, March 1999.

[45] S. F. Mingaleev, Yu. B. Gaididei, P. L. Christiansen, and Yu. S. Kivshar. Nonlinearity-induced conformational instability and dynamics of biopolymers. *Europhysics Letters*, 59(3):403–409, 2002.

[46] R. Reigada, J. M. Sancho, M. Ibañes, and G. P. Tsironis. Resonant motion of discrete breathers in curved nonlinear chains. *Journal of Physics A: Mathematical and General*, 34(41):8465–8475, October 2001.

[47] Peter L. Christiansen, Yuri B. Gaididei, and Serge F. Mingaleev. Effects of finite curvature on soliton dynamics in a chain of non-linear oscillators. *Journal of Physics: Condensed Matter*, 13(6):1181–1192, February 2001.

[48] J. F. R. Archilla, Yu. B. Gaididei, P. L. Christiansen, and J. Cuevas. Stationary and moving breathers in a simplified model of curved alpha–helix proteins. *Journal of Physics A: Mathematical and General*, 35(42):8885–8902, October 2002.

[49] B. Sánchez-Rey, J. F. R. Archilla, F. Palmero, and F. R. Romero. Breathers in a system with helicity and dipole interaction. *Physical Review E*, 66:017601, July 2002.

[50] J. F. R. Archilla, P. L. Christiansen, S. F. Mingaleev, and Yu. B. Gaididei. Numerical study of breathers in a bent chain of oscillators with long-range interaction. *Journal of Physics A: Mathematical and General*, 34(33):6363–6373, August 2001.

[51] Yu. B. Gaididei, S. F. Mingaleev, and P. L. Christiansen. Curvature-induced symmetry breaking in nonlinear schrödinger models. *Physical Review E*, 62(1):R53–R56, July 2000.

[52] J. Cuevas, F. Palmero, J. F. R. Archilla, and F. R. Romero. Moving breathers in a bent DNA model. *Physics Letters A*, 299(2-3):221–225, July 2002.

[53] H. Feddersen. Localization of vibrational energy in globular protein. *Physics Letters A*, 154(7-8):391–395, 1991.

[54] S. F. Mingaleev, P. L. Christiansen, Yu. B. Gaididei, M. Johansson, and K. Ø. Rasmussen. Models for energy and charge transport and storage in biomolecules. *Journal of Biological Physics*, 25(1):41–63, 1999.

[55] M. Peyrard and A. R. Bishop. Statistical mechanics of a nonlinear model for DNA denaturation. *Physical Review Letters*, 62(23):2755–2758, June 1989.

[56] Y. Gao and E. W. Prohofsky. A modified self-consistent phonon theory of hydrogen bond melting. *Journal of Chemical Physics*, 80(5):2242–2243, 1984.

[57] Y. Gao, K. V. Devi-Prasad, and E. W. Prohofsky. A self-consistent microscopic theory of hydrogen bond melting with application to poly (dg).poly(dc). *Journal of Chemical Physics*, 80(12):6291–6298, 1984.

[58] L. D. Landau and E. M. Lifshitz. *The classical theory of fields*. Pergamon Press, 1962.

[59] Maria Barbi. *Localized solutions in a model of DNA helicoidal structure*. PhD thesis, University of Florence, 1998.

[60] Thierry Dauxois. *Dynamique non lineaire et Mechanique Statiostique d'un Modele d'ADN*. PhD thesis, University of Burgondy, 1988. In French.

[61] Vernon D. Barger and Martin G. Olsson. *Classical Electricity and Magnetism*. Allyn and Bacon, Inc., 1987.

[62] M. V. Satarić. The influence of endogenous ac fields on the breather dynamics in DNA. *Physica D: Nonlinear Phenomena*, 126(1-2):60–68, February 1999.

[63] J. Pranata, S. G. Wierschke, and W. L. Jorgensen. Opls potential functions for nucleotide bases. relative association constants of hydrogen-bonded base pairs in chloroform. *Journal of the American Chemical Society*, 113(8):2810–2819, March 1991.

[64] P. V. Larsen, P. L. Christiansen, O. Bang, J. F. R. Archilla, and Yu. B. Gaididei. Energy funneling in a bent chain of morse oscillators with long-range coupling. *Physical Review E*, 69(2):026603–1–026603–6, 2004.

[65] A.A. Sukhorukov, Y.S. Kivshar, O. Bang, J.J. Rasmussen, and P.L. Christiansen. Nonlinearity and disorder: Classification and stability of nonlinear impurity modes. *Physical Review E*, 63(3):366011–3660118, 2001.

[66] Peter Vingaard Larsen. Energy funnelling in a DNA model. Master's thesis, Technical University of Denmark, 2002. IMM-THESIS-2002-32.

[67] Simona Cocco and Rémi Monasson. Theoretical study of collective modes in DNA at ambient temperature. *Journal of Chemical Physics*, 112(22):10017–10033, June 2000.

[68] P. V. Larsen, P. L. Christiansen, O. Bang, J. F. R. Archilla, and Yu. B. Gaididei. Bubble generation in a twisted and bent DNA-like model. *Physical Review E*, 70(3):036609–1–036609–6, 2004.

[69] A. Alvarez, F. R. Romero, J. F. R. Archilla, J. Cuevas, and P. V. Larsen. Moving breathers in a DNA model with a dipole orientation interface. *Submitted to European Physical Journal B*, 2005. arXiv/nlin.PS/0503062.

Part II

Nonlocal Optical Quadratic Materials

8

Introduction to nonlinear optics

The invention of the laser has spurred tremendous interest in the research of nonlinear optics. The laser allows for investigation of nonlinear effects, which are only detectable for the high light intensities provided by the coherent laser light. Furthermore, development of materials which exhibit nonlinearities at lower light intensities has also intensified the research activities in the field.

A motivation for investigating light propagation in optical crystals is — amongst others — the aspect of all-optical signal processing. A successful implementation of this would for one result in remarkable faster optical communications networks, but is also the foundation for optical computers; computers using photons instead of electrons as the fundamental processing unit.

When light waves travel through a medium it is affected by the atoms of the crystal. With a low intensity beam, this effect causes the initial beam profile to broaden with time and/or distance. These effects are referred to as *dispersion* (temporal broadening) and *diffraction* (spatial broadening) and are well understood. But interestingly, if the incoming light beam has a higher intensity, the nonlinear effects, not noticeable in the low intensity beam, become important and these can counteract the broadening; thus resulting in a beam with constant shape as illustrated in Fig. 8.1. This is another example of the balance between linearity and nonlinearity other than the water wave example mentioned in the Introduction on page 1.

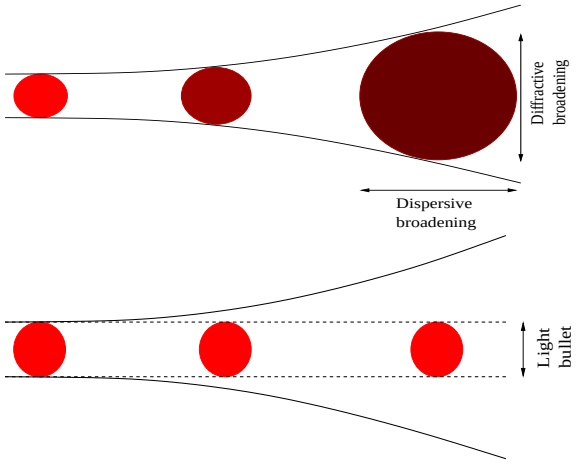

Figure 8.1: *The energy density of a diffracting and dispersive low intensity beam (top) compared to a high intensity spatio-temporal light bullet (bottom). Bright red corresponds to high density; darker red to lower. Redrawn from [1, Fig. 1].*

This effect is a result of the *nonlinearity* in the crystal, which arises from the interaction between photons and electrons in the crystal for large light intensities [2]. The most powerful nonlinear effect is the so-called *quadratic* — or $\chi^{(2)}$— nonlinearity. One important of one such nonlinear effect is

the *second harmonic generation*, also known as *frequency doubling*, in which the crystal induces a secondary wave with the double frequency. With this effect, one can generate, say, visible light from infrared by passing it through a suitable crystal.

Optical solitons in quadratic nonlinear materials The term *quadratic nonlinear materials* refer to materials where the nonlinearity is governed mainly by the $\chi^{(2)}$-effect. Due to their strong and fast nonlinearity, quadratic nonlinear materials have been a center of attention for a number of years. The $\chi^{(2)}$-effect gives rise to for instance frequency doubling — or "up-conversion" — of the fundamental beam, as well as a converse "down-conversion" effect, whereby waves of double frequency are transformed back to the original frequency. In quadratic nonlinear materials, the formation of solitons is not due to a change in refractive index caused by the local intensity of the beam, but due to a cascading phase-modulation mechanism [3]. The term cascading refers to the continuous up- and down-conversion that takes place in these materials. An intuitive explanation given in Ref. [4] explains some of the occurring phenomena, like soliton formation, self-focusing, and self-defocusing, but it does not explain effects such as soliton interaction and the existence of bound states. As mentioned in Chapter 1, the localized entity referred to as a *soliton*, retains its shape due to a balance between linear and nonlinear effects, which counteract each other. In the case of nonlinear optics the linear broadening of the pulse, caused by either temporal *dispersion* or spatial *diffraction* — or both — is countered by the nonlinear *self-phase modulation* focusing effect. The study of localized wave packets have been of particular interest as these solitons can act as ideal carriers of optical information. Spatial solitons were observed experimentally some twenty years ago [5, 6, 7] and some years later temporal solitons (localized in time) were observed using femtosecond laser pulses [8]. Initially, both types of solitons were theoretically predicted almost half a century ago [9, 10], but experimental verification was not possible at that time. With the evolution of sufficiently sophisticated laboratory equipment, this spurred a new interest for research in optical solitons and some examples are found in Refs. [3, 11, 12, 13, 14, 15, 16, 17, 18].

A special type of soliton combines these features: the spatio-temporal soliton, also referred to as a *light bullet*, which exhibits localization in *both* regimes is also a possibility [1, 20, 21, 22, 23, 24]. A light bullet is thus a promising candidate as a unit of information in future all-optical circuits and networks.

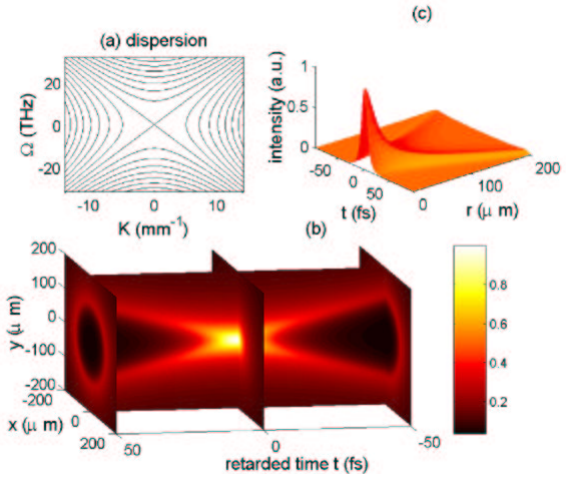

Figure 8.2: *The biconial structure of an X-wave. Note the small amplitude of the "tails" compared to the center peak. From [19], courtesy of S. Trillo.*

X waves The existence of light bullets requires materials with anomalous dispersion which, acting similarly to standard diffraction in bulk materials, can counteract nonlinearities of the self-focusing type. Conversely, normally dispersive media support other effects, such as temporal splitting and spectral breaking [25, 26, 21], that were commonly believed to prevent the existence of nonlinear localized wave-packets. In a material with normal dispersion, the higher frequency components travel slower than the lower frequency components and vice versa for anomalous dispersion. However, the perspective changes completely, if one consider so-called *X-waves* [27],

introduced in 1992 in the field of *linear* acoustics. These waves have translationally invariant solutions of the (scalar) linear wave equation with characteristic biconical shape (they are called X-waves because the main longitudinal cut resembles the letter X) [28].

Therefore they exist also as electromagnetic waves whose evidence has been reported both at microwave frequencies [29], and in the context of linear optics [30, 31] where they can be considered non-monochromatic generalizations of Durnin's Bessel beam [32]. In general, X waves can exist also in vacuum, and do not necessarily have a narrow spectrum. However, when the propagation of beams with narrow spatio-temporal spectral content in bulk dielectrics is considered, linear X-waves turn out to be natural eigenmodes of normally dispersive dielectrics [33, 34]. Their excitation, however, remains quite difficult because their shape is quite far from standard laser beams.

It was therefore a breakthrough when the formation of *nonlinear* X-waves was found starting from a standard Gaussian beam in quadratic nonlinear optical materials [28, 35]. The key is that a sufficiently strong nonlinearity provides, through spatio-temporal modulational instability, a mechanism which is able to dynamically evolve a localized input profile into an X-wave. General results prove that X-waves can have indeed a key role in the nonlinear dynamics both in optics [36, 37, 38, 39], and in Bose-Einstein condensation [40, 41] where the negative effective mass due to a 1D lattice mimics the effect of normal dispersion [42].

Optical nonlocality In contrast, the notion of *nonlocality* was recently shown to provide a simple physical explanation of all these effects, as well as of bound states and general soliton interaction [43]. The idea is to describe the effect of the second harmonic (SH) field on the fundamental through a *response function*, which contains the nonlinearity of the system and the linear properties of the SH. This analogy further allows to obtain analytical solutions of solitons and their bound states in the so-called strongly nonlocal limit, where the governing equations become linear [43, 44, 45]. See also Ref. [46, 47] for a review of the effects of nonlocality.

Considering only one transverse spatial dimension, it was found in Ref. [43] that with a positive phase mismatch, the response function is localized and symmetric. However, a negative phase mismatch introduces a difference in sign in the SH dispersion relation, which in turn changes the nature of the response function to be oscillatory. This corresponds well with the absence of a continuous family of soliton solutions in this case, where only pairs of solitons exist at discrete points, corresponding to isolated values of the separation between the solitons [16].

Including the temporal dimension in the nonlocal description introduces another way of having opposite signs in the SH dispersion relation, namely when considering normally dispersive materials. We would thus expect an analogy between systems that support X-waves and a nonlocal system with an oscillatory response function.

Aim of this work In this work we propose a description of 2+1D X-waves (Here 2+1D means that diffraction is effective in only one transverse dimension, say x, as it occurs in planar waveguides. Linear X-waves have been investigated in this case in Refs. [48, 49]) in quadratic media, based on a nonlocal response function. The inclusion of the temporal dependence complicates the effect somewhat and the response function turns out to be of Bessel type. Interestingly, we show that for normal SH dispersion the local cascading limit in terms of a nonlinear Schrödinger equation does not exist — one *needs to* use the nonlocal description, because the nonlocal response function does not converge towards a delta-function when the degree of nonlocality goes to zero.

Also, we investigate the effects of having opposite signs of the dispersion in the fundamental wave (FW) and SH fields. We demonstrate the novel effect that X-type waves can form in quadratic nonlinear materials with anomalous dispersion at either the FW or the SH.

9
Nonlocality in quadratic materials

Light propagation is in general governed by the celebrated *Maxwell Equations*

$$\nabla \times \mathbf{E} = -\frac{\partial \mathbf{B}}{\partial t}, \tag{9.1}$$

$$\nabla \times \mathbf{H} = \mathbf{J} + \frac{\partial \mathbf{D}}{\partial t}, \tag{9.2}$$

$$\nabla \cdot \mathbf{D} = \rho, \tag{9.3}$$

$$\nabla \cdot \mathbf{B} = 0, \tag{9.4}$$

where $\mathbf{E}$ describes the electric field, $\mathbf{H}$ the magnetic field, and $\mathbf{D}$ and $\mathbf{B}$ the corresponding electric and magnetic flux densities, respectively. $\mathbf{J}$ is called the current density vector and ρ the charge density.

Furthermore, the following material dependent equations are needed, when light propagates through other than vacuum:

$$\mathbf{D} = \varepsilon_0 \varepsilon \mathbf{E} = \varepsilon_0 \mathbf{E} + \mathbf{P}, \tag{9.5}$$

$$\mathbf{B} = \mu_0 \mu \mathbf{H} = \mu_0 \mathbf{H} + \mathbf{M}, \tag{9.6}$$

$$\mathbf{J} = \sigma \mathbf{E}, \tag{9.7}$$

where ε_0 and μ_0 are the permittivity and permeability of free space, respectively[1]

Note that ε (and μ) are *tensors* and it is through nonlinearities in the ε tensor that generates the optical nonlinearities.

However, in the nonlinear case, the ε tensor is a function of the spatial coordinates through crystal configuration. From the first constitutive relation (9.5) we define the *susceptibility*, χ

$$\mathbf{P} = \varepsilon_0 \chi \mathbf{E} \quad \Longleftrightarrow \quad \varepsilon_0 = 1 + \chi. \tag{9.8}$$

The *polarization*, $\mathbf{P}$, is affected by the intensity of the electric field, and we must consider changes in the polarization arising from increasing orders of the electrical field. Thus, the ith component

[1] Values are $\varepsilon_0 = 8.854 \times 10^{-12} \frac{F}{m}$ and $\mu_0 = 4\pi \times 10^{-7} \frac{H}{m}$.

of $\mathbf{P}$ is expanded as

$$P_i = \varepsilon_0 \chi^{(1)}_{ij} E_j + 2\chi^{(2)}_{ijk} E_j E_k + 4\chi^{(3)}_{ijkl} E_j E_k E_l + \dots, \tag{9.9}$$

where we sum over repeated indices (Einstein's summation formula). These nonlinear terms in the polarization of a light beam are the ones responsible for the nonlinearity in nonlinear optics.

Let us investigate Maxwell's equations further. Assuming μ and ε to be constant, taking the curl of (9.1) gives

$$\begin{aligned} \nabla \times (\nabla \times \mathbf{E}) &= = \nabla \times \left\{ -\frac{\partial}{\partial t} (\mu_0 \mu \mathbf{H}) \right\} = -\mu_0 \mu \frac{\partial}{\partial t} \left(\mathbf{J} + \frac{\partial \mathbf{D}}{\partial t} \right) \\ &= -\mu_0 \mu \frac{\partial}{\partial t} \left\{ \sigma \mathbf{E} + \frac{\partial}{\partial t} (\varepsilon_0 \varepsilon \mathbf{E}) \right\} = -\mu_0 \mu \sigma \frac{\partial \mathbf{E}}{\partial t} - \mu_0 \mu \varepsilon_0 \varepsilon \frac{\partial^2 \mathbf{E}}{\partial t^2}. \end{aligned} \tag{9.10}$$

The vector identity $\nabla \times (\nabla \times \mathbf{E}) = \nabla (\nabla \cdot \mathbf{E}) - \nabla^2 \mathbf{E}$, together with the material equation (9.5) gives us

$$\nabla \times (\nabla \times \mathbf{E}) = \nabla \left(\nabla \cdot \frac{\mathbf{D}}{\varepsilon \varepsilon_0} \right) - \nabla^2 \mathbf{E} = -\nabla^2 \mathbf{E}, \tag{9.11}$$

since we assume that there are no free charges, $\rho = 0$, and by (9.3), the divergence of the $\mathbf{D}$ is then zero. This, in fact, is not the case for non-isotropic materials, but the terms turn out to be negligible in this context. Refer to [3] and references therein for details. If we also assume that there is no conductance, $\sigma = 0$, (9.10) and (9.11) become

$$\nabla^2 \mathbf{E} - \varepsilon \mu \varepsilon_0 \mu_0 \frac{\partial^2 \mathbf{E}}{\partial t^2} = 0.$$

Assuming nonmagnetic materials, $\mu = 1$, and since the speed of light is $c = (\varepsilon_0 \mu_0)^{-\frac{1}{2}}$, we get through (9.5)

$$\nabla^2 \mathbf{E} - \frac{1}{c^2} \frac{\partial^2 \mathbf{D}}{\partial t^2} = 0. \tag{9.12}$$

Eq. (9.12) is the starting point for the derivation of the $\chi^{(2)}$-equations and details can be found in [50, 51]. In Appendix C, a sketch of the derivation of the temporal version of the equations is given.

The general idea is that by considering a wave of the form

$$\mathbf{E} \approx E_1 e^{ik_1(\omega_0)z - i\omega_0 t} \hat{\mathbf{e}}_\mathbf{1} + E_2 e^{ik_2(2\omega_0)z - 2i\omega_0 t} \hat{\mathbf{e}}_\mathbf{2} + \mathbf{c.c.}, \tag{9.13}$$

where $\hat{\mathbf{e}}_\mathbf{j}$ is a unit vector describing the polarization of field component j and where we have introduced the notation **c.c.** for the *complex conjugate* and not explicitly written the dependencies of $E_j = E_j(z,t), j = 1, 2$, for brevity. Similar equations describe $\mathbf{D}$, but this may be expressed in terms of $\mathbf{E}$ and inserted in (9.12). We the obtain the equations

$$i \frac{\partial E_1}{\partial z} + i k_1' \frac{\partial E_1}{\partial t} - \frac{1}{2} k_1'' \frac{\partial^2 E_1}{\partial t^2} + K_1 E_1^* E_2 e^{-i\Delta k z} = 0$$

and

$$i \frac{\partial E_2}{\partial z} + i k_2' \frac{\partial E_2}{\partial t} - \frac{1}{2} k_2'' \frac{\partial^2 E_2}{\partial t^2} + K_2 E_2 e^{i\Delta k z} = 0,$$

with constants

$$K_1 = \frac{\omega_0^2 \widetilde{\varepsilon}_1^{(2)}}{k_1 c^2} \quad \text{and} \quad K_2 = \frac{2\omega_0^2}{k_2 c^2} \widetilde{\varepsilon}_2^{(2)}.$$

With proper scalings, excluding the velocity terms (the ∂/∂_t-terms), but including a similar transverse spatial variable, these equations yield

$$i\partial_z E_1 + 2\partial_x^2 E_1 + 2d_1 \partial_t^2 E_1 + E_1^* E_2 e^{-i\beta z} = 0, \tag{9.14}$$

$$i\partial_z E_2 + \partial_x^2 E_2 + d_2 \partial_t^2 E_2 + E_1^2 e^{i\beta z} = 0, \tag{9.15}$$

which are the governing equations for this Part of the work. Details are given in Appendix C.

9.1 The nonlocal description

The general idea behind nonlocality is to describe the effect of the SH on the fundamental through a *response function*, which contains the nonlinearity of the system. This eliminates the equation for the SH and we obtain only a single equation and thereby a better change of making analytical predictions. In contrast to the *cascading* limit, which also reduces two equations to one, the nonlocal approximation makes fewer assumptions.

The notion of nonlocality has been introduced in various papers on one dimensional systems [43, 45, 46, 47, 52, 53, 54, 55].

9.1.1 A one dimensional nonlocality

Let us initially consider a 1+1D version of the $\chi^{(2)}$equations

$$i\partial_z E_1 + d_1 \partial_x^2 E_1 + E_1^* E_2 e^{-i\beta z} = 0, \tag{9.16}$$

$$i\partial_z E_2 + d_2 \partial_x^2 E_2 + E_1^2 e^{i\beta z} = 0, \tag{9.17}$$

to gain some insight into the nature of nonlocality in quadratic materials (this Section follows [43]). We consider a SH field of the form $E_2(x,z) = e_2(x,z)\exp(i\beta z)$, which is inserted in (9.17) to give

$$i\left(\partial_z e_2 + i\beta e_2\right)\exp(i\beta z) + d_2 \partial_x^2 e_2 \exp(i\beta z) + E_1^2 e^{i\beta z} = 0.$$

Assuming that the amplitude of the SH varies slowly with respect to the propagation variable z, we can neglect the first term to give

$$-\beta e_2 + d_2 \partial_x^2 e_2 + E_1^2 = 0 \tag{9.18}$$

For large phase mismatch, $\beta \gg 1$, the first term is dominating the e_2 contribution and therefore the x-derivative may be neglected. This is the cascading limit assumption and it ties the shape of the SH to the one of the FW through the relation $e_2 = E_1^2/\beta$. The phrase that the SH is "slaved" to the FW is also used.

However, this exclusion of the spatial derivative is *not* made in the nonlocal description. If we use Fourier transformation on (9.18), we get

$$-\beta \widetilde{e}_2 - k^2 d_2 \widetilde{e}_2 + \widetilde{E}_1^2 = 0$$

which solves to

$$\widetilde{e}_2 = \frac{1}{\beta + d_2 k^2} \widetilde{E}_1^2, \tag{9.19}$$

where we define the *response function* in Fourier space as

$$\widetilde{R} = \frac{1}{1 + s\sigma^2 k^2}, \tag{9.20}$$

with the *degree of nonlocality* is defined as

$$\sigma = \sqrt{\left|\frac{d_2}{\beta}\right|} \tag{9.21}$$

and with $s = \mathrm{sgn}\,(d_2\beta)$. Keeping in mind that a multiplication in Fourier space corresponds to a convolution in real space, the 1+1D $\chi^{(2)}$-equations (9.16)–(9.17) can then be written

$$\boxed{i\partial_z E_1 + d_1\partial_x^2 E_1 + N\left(E_1^2\right)E_1^* = 0,} \tag{9.22}$$

where the nonlinearity is conveniently determined by the convolution integral

$$\boxed{N\left(E_1^2\right) = \frac{1}{\beta}\int_{-\infty}^{\infty} R(x-\xi)E_1^2(\xi,z)d\xi.} \tag{9.23}$$

Notice that due to the reciprocality of the Fourier transform, a large degree of nonlocality *narrows* the profile of the Fourier transform as in (9.20). The term *nonlocality* is therefore coined to the real space in the sense that a large σ means a broad response function in the real space. But as $\sigma \to \infty$, the Fourier transformed response function (9.20) tends to zero except at $k = 0$ and it therefore becomes very narrow in the Fourier space. Conversely, $\sigma = 0$ returns $\widetilde{R} = 1$, which covers the whole k-axis.

The degree of nonlocality, σ, and different limits.

The convolution integral (9.23) explains the use of the term nonlocality, since it captures the effect of the response function on the squared fundamental field. Fig. 9.1 shows different cases of the relative widths of $|R|$ and $|E_1^2|$.

In Fig. 9.1(a), R is very narrow compared to the FW, and this is referred to as the *local* case. Here, the small width of the response function implies that the effect of the convolution is small. In the limit of the response function being a δ-function, Equation (9.22) becomes the well-known Kerr nonlinearity, described by the nonlinear Schrödinger equation

$$i\partial_z E_1 + d_1\partial_x^2 E_1 + \beta^{-1}|E_1|^2 E_1 = 0. \tag{9.24}$$

In this limit, the light intensity at a given point is determined exclusively from values *at that very point*. This is why it is referred to at the *local* limit. Conversely, as the effect of nonlocality is increased, the value of the light intensity at a given point is a function of values *in a region around the point in question*. The bigger the degree of nonlocality, the bigger the region.

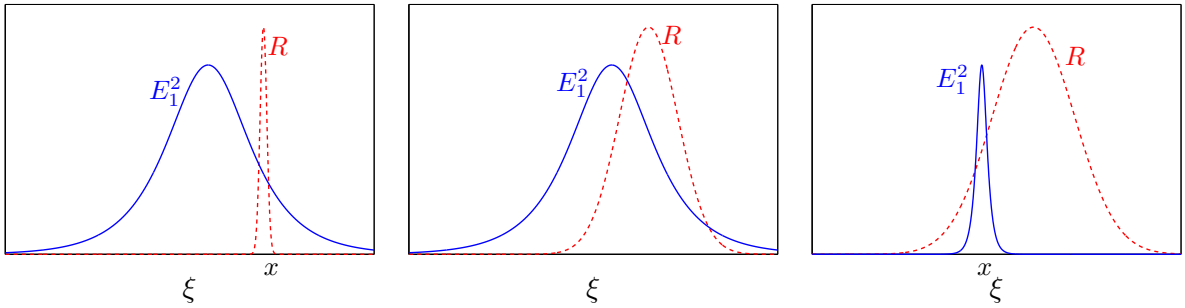

(a) Local case, $\sigma \ll 1$. (b) General case, $\sigma \approx 1$. (c) Nonlocal case, $\sigma \gg 1$.

Figure 9.1: *Different degrees of nonlocality.*

Fig. 9.1(b) shows a case where the response function and the FW intensity profile are of comparable widths; this is the general case.

The effect of a very wide response function is shown in Fig. 9.1(c). Here, the response function will greatly affect the outcome of the convolution. In this case, the value of the FW intensity at a given site is determined by the value of all other sites through this folding of R onto E_1^2, in accordance with (9.23).

For a given one dimensional FW intensity profile, the value of σ determines strength of the nonlocality (see derivation in Sec. 9.1.1). The local case [Fig. 9.1(a)] occurs for $\sigma \ll 1$, where R is narrow, and the nonlocal case [Fig. 9.1(c)] for very large values, $\sigma \gg 1$, where the response function is broad compared to the FW.

A physical example of the application of nonlocality is for instance found in liquid crystals. Here, light is propagated through a medium whose refractive index changes with the temperature of the crystal plasma. Because of heat dissipation, the energy provided by the incident light beam begins relatively quickly to dissipate into the surrounding liquid phase, increasing the temperature and thereby changes the refractive index. In this case, the rate of index change is proportional to the temperature difference between neighboring point; thus a nonlocal model is needed for a proper description.

The local limit The local and nonlocal limits allow for approximations of the convolution integral. For the narrow response function in the local limit, the intensity profile is approximated by a Taylor expansion:

$$\begin{aligned}
\int_{-\infty}^{\infty} R(x-\xi)E_1^2(\xi,z)d\xi \;&\approx\; \int_{-\infty}^{\infty} R(x-\xi)\Big[E_1^2(x,z) \\
&\qquad +\partial_x E_1^2(x,z)(\xi-x)+\frac{1}{2}\partial_x^2 E_1^2(x,z)(\xi-x)^2+\ldots\Big]d\xi \\
&= E_1^2(x,z)\int_{-\infty}^{\infty} R(x-\xi)d\xi \\
&\qquad +\partial_x E_1^2(x,z)\int_{-\infty}^{\infty} R(x-\xi)(\xi-x)d\xi \\
&\qquad +\frac{1}{2}\partial_x^2 E_1^2(x,z)\int_{-\infty}^{\infty} R(x-\xi)(\xi-x)^2 d\xi+\ldots.
\end{aligned} \tag{9.25}$$

For a normalized response function, $\int_{-\infty}^{\infty} R(x-\xi)d\xi = 1$, we once again the we then obtain (to first order accuracy) the NLS equation (9.24).

$$i\partial_z E_1 + d_1\partial_x^2 E_1 + \beta^{-1}|E_1^2|E_1 = 0, \tag{9.26}$$

Note that if the response function is even, the second term in (9.25) vanishes and (9.26) has second order accuracy. This is often the case for physically reasonable response functions. In general, the response function may attain various shapes, where some physically reasonable are Gaussians, Lorentzians, sech-shaped, e.g., and they need not be symmetric [56].

In the strongly nonlocal limit a similar approximation is employed, but now it is the response function, which is almost constant compared to E_1^2. We get

$$i\partial_z E_1 + d_1\partial_x^2 E_1 + \beta^{-1}R(x)P_1E_1 = 0,$$

with the power

$$P_1 = \int_{-\infty}^{\infty} E_1^2(\xi)d\xi.$$

Solving the 1D response function

The response function was introduced in the Fourier space in (9.20), but by performing an inverse Fourier transform,

$$R(x) = \mathcal{F}^{-1}\left\{\widetilde{R}(k)\right\} = \frac{1}{2\pi}\int_{-\infty}^{\infty}\widetilde{R}(k)e^{-ikx}dk = \frac{1}{2\pi}\int_{-\infty}^{\infty}\frac{1}{1+s\sigma^2k^2}e^{-ikx}dk,$$

we obtain an expression in the real space. There are two distinct cases depending on the sign of s.

$s = +1$ In this case, $\widetilde{R}(k) = 1/\left(1+\sigma^2k^2\right)$, see Fig. 9.2(a). By parity, symmetry, and change of variable $\kappa = \sigma k$, we get

$$R(x) = \frac{2}{2\pi\sigma}\int_0^{\infty}\frac{1}{1+\kappa^2}\cos\left(\frac{x}{\sigma}\kappa\right)d\kappa,$$

which has the solution [57, 3.723.2] (or is solved by calculus of residues)

$$R_+(x) = \frac{1}{2\sigma}e^{-\frac{|x|}{\sigma}}, \tag{9.27}$$

where index "+" denotes $s = +1$, shown in Fig. 9.2(b).

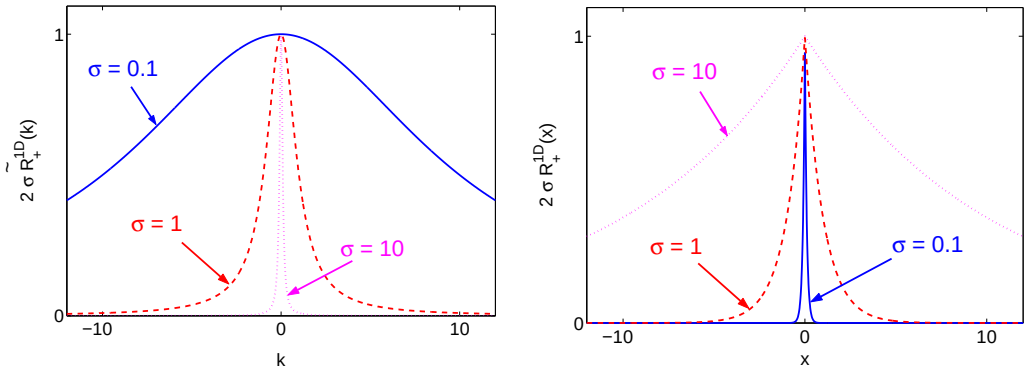

(a) Spectral domain, $\widetilde{R}_+^{1D}(k)$. (b) Real domain, $R_+^{1D}(x)$.

Figure 9.2: *The 1D response function for $s = +1$, in spectral and real domain for different degrees of the nonlocality, σ.*

We note that the response function (9.27) is not differentiable at $x = 0$. This causes some inaccuracy in the region close to $x = 0$, but thanks to the convolution integral with the response function, the deviation from the true solution is only small (see e.g. [43, Fig. 2]).

Fig. 9.2 depicts how a large degree of nonlocality corresponds to a wider profile in the real space, but a narrower in the spectral domain.

The response function for $s = +1$ is normalizable, since

$$\int_{-\infty}^{\infty} R_+(x)\,dx = \frac{1}{2\sigma}\int_{-\infty}^{\infty} e^{-\frac{|x|}{\sigma}}dx = \frac{1}{\sigma}\int_{0}^{\infty} e^{-\frac{|x|}{\sigma}}dx = 1 \tag{9.28}$$

by [57, 3.310] (or — as usual — by calculus of residues). This is one of the requirements for R_+^{1D} to tend to a δ-function in the local limit $\sigma \to 0$.

$s = -1$ Here, the Fourier transformed response function $\widetilde{R}(k) = 1/\left(1-\sigma^2k^2\right)$ has singularities at $k = \pm 1/\sigma$, see Fig. 9.3(a). By applying the same observations of parity, symmetry, and change of variable as in the $s = +1$ case, we get

$$R(x) = \frac{2}{2\pi\sigma}\int_0^{\infty}\frac{1}{1-\kappa^2}\cos\left(\frac{x}{\sigma}\kappa\right)d\kappa,$$

which has the solution [57, 3.723.9] (or is solved by calculus of residues)

$$R_-(x) = \frac{1}{2\sigma}\sin\frac{|x|}{\sigma},$$

where index "−" denotes $s = -1$, see Fig. 9.3(b).

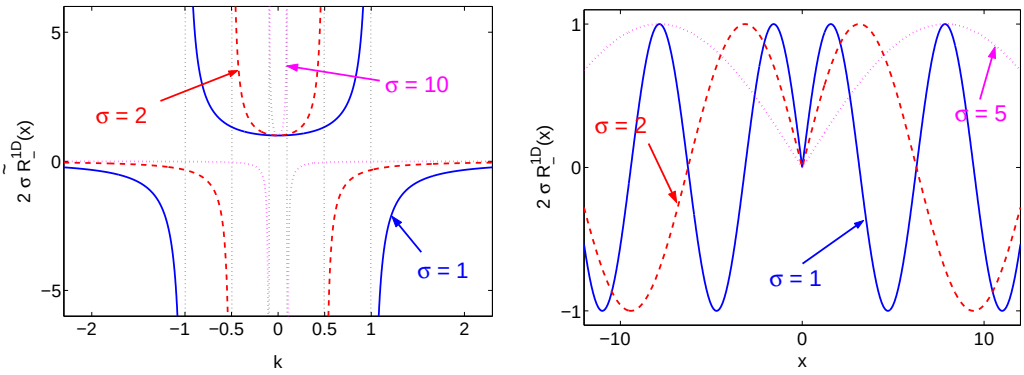

(a) Spectral domain, $\widetilde{R}_-^{1D}(k)$. (b) Real domain, $R_-^{1D}(x)$.

Figure 9.3: *The 1D response function for $s = -1$, in spectral and real domain for different degrees of the nonlocality, σ.*

For $s = -1$, the response function is thus oscillatory and is not normalizable as in the $s = +1$ case. Also, the nonlocal effect of σ is somewhat less pronounced, but it is still recognizable. Looking at the curve for $\sigma = 5$ in Fig. 9.3(b), we see how it almost engulfs the depicted window, whereas the $\sigma = 1$-curve oscillates rapidly. In the spectral window, the singularities are there for all values of σ and $\widetilde{R}_-^{1D}(k)$ tends to zero for large values of $|k|$, but for the smaller degree of nonlocality, the width of the center region with values bigger than 1 is expanded.

9.1.2 Nonlocality in general dimensions

With this introduction in only one dimension to the notion of nonlocality described by response functions and convolution integrals in Sec. 9.1.1, it is hopefully easier to extend the idea to more dimensions.

In the one dimensional case, the degree of nonlocality is comparable to the length of some line. In two dimensions, one needs to consider the *areas* where the response function and the intensity profile have significant contributions. As an example, a punctuation mark on this sheet of paper is local, compared to the area of the entire sheet. A life size picture of for example a Compact Disc would not be, as it would take up a significant part of the paper area, so a general nonlocal description would be in order. Compared to the same sheet of paper, any sports field (soccer, basket ball, cricket, tennis, etc.) would be significantly larger than the piece of paper. Thus, the strongly nonlocal limit would be appropriate here.

In three dimensions, nonlocality can still be imagined. For instance, a pea would be almost "local" to a basket ball, but not to a golf ball. The larger basket ball would still be local to, say, the moon or any celestial object.

The concepts described for the 1D case in Sec. 9.1.1 have their extensions to multiple dimensions as we shall see. A key issue is that with the introduction of both spatial and temporal variation implies both diffraction as well as dispersion. This means that new combinations of signs appear, as we shall see in the following.

9.2 Quadratic nonlocality

We are considering the standard normalized (all quantities are suitably scaled so that they are dimensionless) model for $\chi^{(2)}$-materials [50, 51]. These equations are also derived in Appendix C and the work in this Part is also presented in Ref. [58]. We have

$$\begin{aligned} i\partial_z E_1 + 2\partial_x^2 E_1 + 2d_1\partial_t^2 E_1 + E_1^* E_2 e^{-i\beta z} &= 0, & (9.29)\\ i\partial_z E_2 + \partial_x^2 E_2 + d_2\partial_t^2 E_2 + E_1^2 e^{i\beta z} &= 0, & (9.30) \end{aligned}$$

where E_1 and E_2 denote the slowly varying amplitude of the fundamental wave and the second harmonic, respectively, and β is the phase mismatch. Important in our context is the sign of β and the dispersion coefficients d_1 and d_2. Positive values of $d_{1,2}$ describe anomalous dispersion, responsible for temporal localization [20, 21, 1], whereas a negative value describes normal dispersion; a requirement for the existence of X-waves in the linear case [38].

To obtain simple intuitive predictions it is customary to write the SH as $E_2 = e_2(x,z,t)\, e^{i\beta z}$, which transforms the SH equation to

$$\beta e_2 - i\partial_z e_2 - \partial_x^2 e_2 - d_2\partial_t^2 e_2 = E_1^2.$$

For large phase mismatch, $|\beta| \to \infty$, we obtain the cascading limit, $e_2 \approx E_1^2/\beta$, (corresponding to neglecting all derivatives of e_2), and we obtain the nonlinear Schrödinger equation (NLS) for the FW

$$i\partial_z E_1 + 2\partial_x^2 E_1 + 2d_1\partial_t^2 E_1 + \beta^{-1}|E_1|^2 E_1 = 0, \qquad (9.31)$$

with a local Kerr nonlinearity. It is known that X-wave solutions to the NLS (9.31) exist in both the linear and nonlinear cases, provided that $d_1 < 0$ [38]. The cascading limit corresponds to assuming that the SH is slowly varying in all coordinates. However, Eq. (9.31) with $e_2 \approx E_1^2/\beta$, does not accurately describe all the dynamics of the original Eqs. (9.29)–(9.30). For example, the NLS equation predicts collapse and modulational instability (MI) for positive β and d_1, but it is well known that collapse does not exist in $\chi^{(2)}$-materials [17, 59, 60], and that the existence of MI depends on the sign of d_2 [3]. In a 1+1D model, it was recently shown that a nonlocal picture correctly describes these effects and the existence of bound states, while still providing a simple physically intuitive model [43].

In the nonlocal approach, the only assumption is that $|\partial_z e_2| \ll |\beta e_2|$, that is, the SH varies slowly in z, but without any restrictions on the x or t dependence. Thus, the nonlocal equations become

$$\begin{aligned} i\partial_z E_1 + 2\partial_x^2 E_1 + 2d_1\partial_t^2 E_1 + E_1^* e_2 &= 0, & (9.32)\\ -\beta e_2 + \partial_x^2 e_2 + d_2\partial_t^2 e_2 + E_1^2 &= 0. & (9.33) \end{aligned}$$

Physical insight into the system can be extracted from the spectral domain, and we therefore apply Fourier transformation in both the spatial and temporal domain $\left[\widetilde{e_2}(k,\omega) = \int\int e_2(x,t) e^{ikx} e^{i\omega t} dx dt\right.$, where an integration without explicit limits here and henceforth denotes integration from $-\infty$ to $\left.\infty\right]$, whereby Eq. (9.33) solves to

$$\boxed{\widetilde{e_2} = \frac{1}{\beta}\,\frac{1}{1 + s_\beta \sigma^2 (k^2 + d_2\omega^2)}\widetilde{E_1^2} = \frac{1}{\beta}\,\widetilde{R}\,\widetilde{E_1^2}.} \qquad (9.34)$$

In this equation, tilde denotes Fourier transformation, s_β is the sign of the phase mismatch, and σ represents the *degree of nonlocality*

$$\boxed{\sigma = \frac{1}{\sqrt{|\beta|}}.} \tag{9.35}$$

In the simplest case, $s_\beta = d_2 = +1$, we see how the cascading limit corresponds to the local limit, $\sigma \to 0$, and that the Fourier transformed *response function* approaches a constant, $\widetilde{R} = 1$, which yields the NLS equation (9.31) discussed above. As we shall see, the case $s_\beta = -d_2 = 1$ does not have the same simple local (nor nonlocal) limit.

Substitution of Eq. (9.34) into Eq. (9.32) yields the nonlocal equation for the fundamental

$$\boxed{i\partial_z E_1 + 2\partial_x^2 E_1 + 2d_1\partial_t^2 E_1 + \beta^{-1} N\left(E_1^2\right) E_1^* = 0,} \tag{9.36}$$

with the nonlocal nonlinearity determined by

$$\boxed{N\left(E_1^2\right) = \iint R\left(x-\xi, t-\eta\right) E_1^2(\xi,\eta,z) d\xi d\eta.} \tag{9.37}$$

Here we see how the nonlinear term is computed by a two dimensional convolution integral over the squared FW and the response function, R. Compare to the one dimensional case in Eqs. (9.22)–(9.23). The response function in real space is found through a 2D inverse Fourier transform

$$R\left(x,t\right) = \frac{1}{4\pi^2}\iint \frac{e^{-ikx}e^{-i\omega t}}{1 + s_\beta\sigma^2\left(k^2 + d_2\omega^2\right)} dk d\omega. \tag{9.38}$$

Note how the linear SH properties are incorporated in the response function.

Looking at Eq. (9.36) we identify the strength of the *nonlinearity* as

$$\boxed{\gamma = \frac{1}{\beta} = s_\beta\sigma^2.} \tag{9.39}$$

Interestingly, both the degree of nonlocality and the strength of nonlinearity are determined by σ. Therefore it is not possible to choose these parameters independently.

In the strongly nonlocal limit, $\sigma \gg 1$, R is assumed to be much broader than E_1^2 in Eq. (9.37) and can therefore be approximated by its Taylor expansion. This makes Eqs. (9.36)–(9.37) effectively linear of the form

$$i\partial_z E_1 + 2\partial_x^2 E_1 + 2d_1\partial_t^2 E_1 + \beta^{-1} R(x,t) E_1^* P_1 = 0. \tag{9.40}$$

Similarly, in the local limit, $\sigma \ll 1$, is assumed to be much broader than R in order to obtain the NLS equation. For bright solitons $P_1 = \iint E_1^2(u,v) du dv$; for dark solitons $P_1 = \iint \left[A_1^2 - E_1^2(u,v)\right] du dv$, where A_1 is the background amplitude.

In the 1+1D case discussed in Sec. 9.1.1, the response function was easily derived and the approximation provides excellent agreement with the full equations, except for a narrow region around the origin, where the response function is non-differentiable [43]. In our 2D case, however, the response function is more complicated. As we shall see, for $d_2 = +1$ a singularity arises at $(x,t) = (0,0)$, whereas for $d_2 = -1$ the response function is singular along hyperbolas in the xt-plane. When singularities arise, the linearization made for the approximation (9.40) is no longer valid. This has profound effects for the description of the nonlocal system, e.g., neither accessible solitons [61] nor the cascading limit exist (this is discussed in Sec. 12.2).

Henceforth, we shall only consider the case of positive phase mismatch, $s_\beta = +1$, corresponding to a self-focusing nonlinearity at FW in the cascading limit. The case with negative phase mismatch, $s_\beta = -1$, and normal SH dispersion, $d_2 = -1$ is completely analogous to the case $s_\beta = +1$ and $d_2 = -1$, but with x and t interchanged. The case $s_\beta = -1$ and $d_2 = +1$, which gives a circularly shaped singularity in the response function, is not considered in the present work.

10
Simulation considerations

To solve the $\chi^{(2)}$-equations (9.29)–(9.30) we have used a Fourier split step method. This is a spectral method, in which the nonlinear part is solved with a fourth order Runge-Kutta solver and the linear part through a Fast Fourier Transform. The method is explained more thoroughly in Appendix D.

With this computational scheme, we evolve the equations in z with step size $dz = 0.001$. This ensures that the power

$$P = \iint \left(|E_1|^2 + |E_2|^2 \right) dxdy \tag{10.1}$$

is constant, with a relative deviation of less than 10^{-10}. The simulation box is $-25 < x, t < 25$, divided into 256×256 grid points unless otherwise noted (see Table D.1).

As mentioned previously, using a Gaussian input beam profile, X-waves have been shown to spontaneously generate [28, 19]. We also use a Gaussian initial condition

$$E_1(x, t, z = 0) = A \; e^{-(x^2+t^2)/B^2}, \tag{10.2}$$

where B determines the diameter of the pulse, usually $B = 3$. We assume no *seeding* (in the sense that $E_2(x, t, z = 0) = 0$), and we typically use an amplitude of $A = 5$ to ensure a sufficiently strong nonlinear effect.

10.1 Linear and nonlinear length scales

A crucial knowledge to have when conducting numerical (and real!) experiments in nonlinear optical crystals is the linear and nonlinear length scales. These are numbers that quantify the effects originating from the linear dispersive/diffractive and the nonlinear terms, respectively. The numbers, L_{D} and L_{NL}, measures what propagation distance is necessary to observe the various phenomena. Roughly speaking, at propagation distance $z \ll L_{\mathrm{D}} \ll L_{\mathrm{NL}}$, both the linear and nonlinear effects are negligible and the input beam profile will therefore be almost constant. If z is of comparable size as the dispersion/diffraction length, $z \approx L_{\mathrm{D}}$, but $z \ll L_{\mathrm{NL}}$, we begin to observe dispersive and diffractive effects, but without significant nonlinear disturbances. Conversely, at some $z \gg L_{\mathrm{NL}}$, but $z \ll L_{\mathrm{D}}$ (in some other medium!), we will see a behavior governed almost exclusively by the nonlinear terms of the equations.

It is therefore important to know these lengths scales in a given experiment, because otherwise one is not able to say whether any observation is due to linear, nonlinear or both effects. In our

case, looking for stationary solitonic solutions, we wish to be well into both the linear as well as the nonlinear regime, because the existence of these particular entities depends on an interplay between linear and nonlinear effects.

There is some freedom allowed in the definition of these lengths scales. Often, the dispersion/diffraction length is defined as the propagation distance at which the width of the pulse has broadened by a factor of 2 or $\sqrt{2}$ [62], but equally as common is that the maximum intensity or amplitude drops by a similar factor. The nonlinear length scale can be used analogously, but may also be defined through the phase shift. In this way, L_{NL} may correspond to the propagation length at which the phase of the initial beam has changed by, say, π.

In the following Sections, we will define the linear and nonlinear length scales. We will assume a Gaussian input beam profile as in Eq. (10.2) where A is the amplitude and B the spatial and temporal width of the pulse. We also assume an unseeded SH. It is no coincidence that we choose this initial condition, as nonlinear X-waves have been shown to spontaneously generate [28, 19]. Moreover, it provides some simplifications to the considerations made in the following Sec. 10.1.1 and 10.1.2.

10.1.1 The linear length scale

To derive the linear dispersion/diffraction length scale, we consider Eqs. (9.29)–(9.30) without the nonlinear terms. Thus, there is no coupling between the FW and the SH, and since we consider the unseeded case, we need only look at the FW for now. The equation to investigate is

$$i\partial_z E_1 + 2\partial_x^2 E_1 + 2\partial_t^2 E_1 = 0, \tag{10.3}$$

so we are assuming $d_2 = +1$ without loss of generality. We solve Eq.(10.3) by 2D Fourier transformation $\widetilde{E_1} = \frac{1}{\sqrt{2\pi}^2}\iint E_1(x,t,z)e^{-ikx}e^{-i\omega t}dxdt$. This is inserted in (10.3) to give

$$i\partial_z \widetilde{E_1} = -2i\left(k^2+\omega^2\right)\widetilde{E_1},$$

which solves in the spectral domain to

$$\widetilde{E_1}(k,\omega,z) = \widetilde{E_1}(0)e^{-2i\left(k^2+\omega^2\right)z},$$

where $\widetilde{E_1}(0)$ is the Fourier transform of the initial condition. This becomes

$$\widetilde{E_1}(0) = \frac{1}{2\pi}\int_{-\infty}^{\infty}\int_{-\infty}^{\infty} A\; e^{-(x^2+t^2)/B^2}e^{-ikx}e^{-i\omega t}dxdt = \frac{A}{2\pi}\left[\int_{-\infty}^{\infty} e^{-\left(\frac{x}{B}\right)^2}e^{-ikx}dx\right], \tag{10.4}$$

which by the equality $\int_0^\infty e^{ax^2}\cos bx dx = \frac{1}{2}\sqrt{\frac{\pi}{a}}e^{b^2/4a}$ solves to [57, 3.896.4]

$$\widetilde{E_1}(0) = \frac{AB^2}{2}e^{-\frac{k^2+\omega^2}{4}B^2}. \tag{10.5}$$

An inverse 2D Fourier transform, $E_1(x,t,z) = \frac{1}{\sqrt{2\pi}^2}\iint \widetilde{E_1}(0)e^{ikx}e^{i\omega t}dkd\omega$, on (10.4) with the expression (10.5), then yields

$$E_1(x,t,z) = \frac{AB^2}{4\pi}\left[\sqrt{\frac{\pi}{\frac{B^2}{4}-2iz}}^2\exp\left(\frac{-(x^2+t^2)}{B^2-2iz}\right)\right].$$

This is trivially rearranged into a complex number in ordinary form $z = a + ib$. For the purpose of finding the diffraction/dispersion length, however, we do not need to now the value of the resulting factor to the exponential function as we are looking for a relative width broadening. Therefore it suffices to consider

$$E_1 \propto \mathcal{C} \exp\left(-\frac{r^2}{B^4 + 64z^2} B^2\right), \tag{10.6}$$

where the spatio-temporal radius $r = \sqrt{x^2 + t^2}$ has been introduced, and where the prefactor as well as an oscillating term has been incorporated into $\mathcal{C}$. This can be chosen so that at $z = 0$, the width of the pulse is $r_0 = B$. We define the linear diffraction/dispersion length as the propagation distance at which this width has doubled: $r_0 \to 2r_0$. Then the diffraction/dispersion length is a matter of solving the equation

$$r_0|_{z=0} = 2r_0|_{z=L_{\mathrm{D}}} \quad \Longleftrightarrow \quad r_0^2 = (2B)^2 = B^2 + \frac{64z^2}{B^2}$$

and we get the linear diffraction/dispersion length, $z = L_{\mathrm{D}}$, as

$$\boxed{L_{\mathrm{D}} = \frac{\sqrt{3}}{8} B^2} \tag{10.7}$$

We note that because of the unseeded SH initial condition, we need not to look for any linear length for the SH.

10.1.2 The nonlinear length scales

Just as the nonlinear terms were neglected when determining the linear length in Sec. 10.1.1, we disregard the linear terms when looking for the nonlinear length, L_{NL}. Thus, we are considering the equations

$$i\partial_z E_1 + E_1^* E_2 e^{-i\beta z} = 0, \quad i\partial_z E_2 + E_1^2 e^{i\beta z} = 0. \tag{10.8}$$

Already it is apparent that the search for the nonlinear length scale is more difficult than in the linear case, where we could use Fourier transformation. We note that the total intensity $I = |E_1|^2 + |E_2|^2$ of (10.8) is constant. This result is obtained by multiplying the FW and SH (10.8) with the respective complex conjugates. This gives

$$iE_1^* \partial_z E_1 + \left(E_1^*\right)^2 E_2 e^{-i\beta z} = 0, \quad iE_2^* \partial_z E_2 + E_1^2 E_2^* e^{i\beta z} = 0$$

and since $\partial_z |E_1|^2 = E_1^* \partial_z E_1 + E_1 \partial_z E_1^*$ we find

$$\begin{aligned} \partial_z |E_1|^2 &= \left(E_1^*\right)^2 E_2 e^{-i\beta z} - iE_1^2 E_2^* e^{i\beta z}, \\ \partial_z |E_2|^2 &= iE_1^2 E_2^* e^{i\beta z} - \left(E_1^*\right)^2 E_2 e^{-i\beta z} = -\partial_z |E_2|^2, \end{aligned}$$

so $\partial_z \left(|E_1|^2 + |E_2|^2\right) = 0$.

We consider again the nonlocal approximation, $E_2(z) = e_2(z) e^{i\beta z}$ (without the linear terms, the fields are constant in x and t), and so the SH equation becomes $i\partial_z e_2 - \beta e_2 + E_1^2 = 0$.

In the local limit, $|\beta| \gg 1$ and we obtain the nonlinear Schrödinger equation

$$i\partial_z E_1 + \frac{1}{\beta} |E_1|^2 E_1 = 0. \tag{10.9}$$

In the slowly varying envelope approximation we can treat $|E_1|^2$ as constant, in which case (10.9) solves to

$$E_1(z) = E_1(0)\exp\left(i\frac{1}{\beta}|E_1|^2 z\right). \tag{10.10}$$

From this expression, there is no amplitude variation with z. We therefore define the nonlinear length scale in the local (cascading) limit as the *propagation distance corresponding to a phase shift of* π. From (10.10) we see that this occurs for $z = L_{\mathrm{NL}}^{\mathrm{NLS}}$

$$\boxed{L_{\mathrm{NL}}^{\mathrm{NLS}} = \frac{\pi|\beta|}{A^2} = \frac{\pi}{\sigma^2 A^2}.} \tag{10.11}$$

In terms of the degree of nonlocality, this approximation is valid for $\sigma \ll 1$.

In another limiting case, the case of phase matching, $\beta = 0$, and the equations (10.8) become

$$\partial_z E_1 = iE_1^* E_2, \quad \partial_z E_2 = iE_1^2. \tag{10.12}$$

With the solution Ansätze,

$$E_1(z) = A_1\mathrm{sech}(Bz), \quad \text{and} \quad E_2(z) = iA_2\tanh(Bz),$$

insertion in (10.12) yields

$$-A_1 B\mathrm{sech}(Bz)\tanh(Bz) = -A_1^2 A_2\mathrm{sech}^2(Bz)\tanh(Bz), \quad A_2 B\mathrm{sech}^2(Bz) = iA_1^2\mathrm{sech}^2(Bz),$$

from which $A_2 = B$ and $A_1^2 = B^2$. Then $I = |E_1|^2 + |E_2|^2 = B^2$ and the solutions (10.1.2) become

$$E_1(z) = \sqrt{I}\mathrm{sech}\left(\sqrt{I}z\right), \quad E_2(z) = i\sqrt{I}\tanh\left(\sqrt{I}z\right).$$

In this case it is more natural to define the nonlinear length as the *propagation distance at which the FW intensity is halved*, $|E_1|^2 = I/2$. It is found by solving the equation $\mathrm{sech}^2\left(\sqrt{I}z\right) = \frac{1}{2}$ which by the definition of the inverse hyperbolic secant function is easily solved to

$$\boxed{L_{\mathrm{NL}}^{\mathrm{int}}\big|_{\beta=0} = \frac{1}{\sqrt{I}}\ln\left(\sqrt{2}+1\right).} \tag{10.13}$$

This approximation is valid for $\sigma \gg 1$ and for $A = \sqrt{I} = 5$, we have $L_{\mathrm{NL}}^{\mathrm{int}}\big|_{\beta=0} \approx 0.1763$.

In the general case, no assumptions are made on β, and we look for solutions of the form

$$E_1(z) = A_1 e^{i\phi_1}, \quad E_2(z) = A_2 e^{i\phi_2} e^{i\beta z},$$

and also define $\theta = \phi_2 - 2\phi_1$ (inspired by [63]). Here, both the amplitudes $A_{1,2}$ and phases $\phi_{1,2}$ are functions of z, and for simplicity we denote differentiation with respect to z by a dot in the following. Insertion in (10.8) together with the nonlocal approximation yields

$$i\dot{A}_1 - A_1\dot{\phi}_1 + A_1 A_2 e^{i\theta} = 0, \quad i\dot{A}_2 - A_2\dot{\phi}_2 - \beta A_2 + A_1^2 e^{-i\theta} = 0, \tag{10.14}$$

Separating into real and imaginary parts gives us

$$\begin{aligned} \dot{A}_1 + A_1 A_2\sin\theta = 0, \quad -\dot{A}_1\dot{\phi}_1 + A_1 A_2\cos\theta = 0, \\ \dot{A}_2 - A_1^2\sin\theta = 0, \quad -\dot{A}_2\dot{\phi}_2 - \beta A_2 + A_1^2\cos\theta = 0. \end{aligned}$$

The equations for $\dot{\phi}_{1,2}$ are condensed into

$$\dot{\theta} = \dot{\phi}_2 - 2\dot{\phi}_1 = \left(\frac{A_1^2}{A_2} - 2A_2\right)\cos\theta - \beta.$$

Again, the total intensity $I = A_1^2 + A_2^2$ is conserved, since $\dot{I} = 2A_1\dot{A}_1 + 2A_2\dot{A}_2 = \ldots = 0$ (by insertion). The intensity is not the only conserved quantity inherent in Eqs. (10.14). A quantity of the form $\mathcal{H} = \left(C_1A_2 + C_2A_2^3\right)\cos\theta + A_2^2$ is introduced. To have it conserved, it is differentiated and equaled to zero, which solves to

$$\mathcal{H} = 2\left(A_2^2 - I\right)A_2\cos\theta + \beta A_2^2. \tag{10.15}$$

This means we have the identities

$$\begin{aligned} \dot{A}_1 &= -A_1A_2\sin\theta & I &= A_1^2 + A_2^2 \\ \dot{A}_2 &= A_1^2\sin\theta & \mathcal{H} &= 2\left(A_2^2 - I\right)A_2\cos\theta + \beta A_2^2 \\ \dot{\theta} &= \left(\tfrac{A_1^2}{A_2} - 2A_2\right)\cos\theta - \beta & \dot{\phi}_1 &= A_2\cos\theta \end{aligned} \tag{10.16}$$

These will allow us to determine an expression for the nonlinear length scale, even though the road is still somewhat cumbersome. We define $u \equiv A_2^2$, which differentiated with respect to z gives $\dot{u} = 2A_2\left(I - A_2^2\right)\sin\theta$. Squaring this expression and inserting the values from (10.16) gives us a third degree polynomial in u:

$$\dot{u}^2 = 4u^3 - \left(8I + \beta^2\right)u^2 + \left(4I^2 + 2\mathcal{H}\beta\right) - \mathcal{H}^2.$$

Considering unseeded initial conditions, $A_2(0) = 0$ and thus also $u = 0$ and $\mathcal{H} = 0$. The polynomial then has a root $u_0 = 0$ and $u_1 > 0$ and $u_2 < u_1$ and can be written

$$\dot{u}^2 = \left[4u^2 - \left(8I + \beta^2\right)u + 4I^2\right]u = 4\left(u - u_0\right)\left(u - u_1\right)\left(u - u_2\right) \equiv f(u),$$

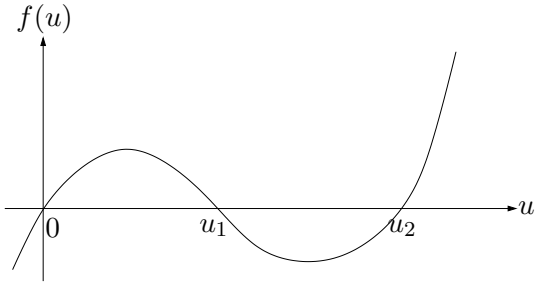

Figure 10.1: *The polynomial $f(u)$.*

see Fig. 10.1. By examining the derivative of f, we find that $f(u)$ is positive between the roots $u_0 = 0$ and $u_1 > 0$ and that these roots are

$$u_1 = \frac{1}{8}\left(8I + \beta^2 - \sqrt{16I\beta^2 + \beta^4}\right), \tag{10.17}$$

$$u_2 = \frac{1}{8}\left(8I + \beta^2 + \sqrt{16I\beta^2 + \beta^4}\right). \tag{10.18}$$

We therefore have

$$\dot{u} = 2\sqrt{u\left(u - u_1\right)\left(u - u_2\right)}. \tag{10.19}$$

Defining $u \equiv u_1a^2$, which is valid for positive u, (10.19) may be written

$$\dot{a} = \sqrt{\left(1 - a^2\right)\left(u_2 - u_1a^2\right)} = \sqrt{u_2}\sqrt{\left(1 - a^2\right)\left(1 - k^2a^2\right)}, \tag{10.20}$$

where the constant $k = \sqrt{u_1/u_2}$ is between 0 and 1. By separation of variables, (10.20) a is found by

$$\int_0^z \sqrt{u_2}\,dw = \sqrt{u_2}\,z = \int_0^a \frac{1}{\sqrt{\left(1 - v^2\right)\left(1 - k^2v^2\right)}}dv \tag{10.21}$$

so $a = \mathrm{sn}\left(\sqrt{u_2}z; k\right)$; the Jacobi elliptic sn-function of modulus k^2. Then

$$u(z) = u_1\,\mathrm{sn}^2(\sqrt{u_2}z; k), \quad k = \sqrt{\frac{u_1}{u_2}}, \tag{10.22}$$

with u_1 and u_2 given by (10.17) and (10.18), respectively.

Intensity-based nonlinear length, $L_{\mathrm{NL}} = L_{\mathrm{NL}}^{\mathrm{int}}$

We are now able to give a definition of the nonlinear length scale in the case of general phase mismatch, β. u is the square of the SH amplitude, so the definition of the nonlinear length as *the propagation distance at which the SH reaches half the total intensity*, $u\left(L_{\mathrm{NL}}^{\mathrm{int}}\right) = I/2$, can be found by solving the equation $u_1 > I/2$. From (10.17)–(10.18) we note that we must impose the restraint $|\beta| < \sqrt{2I}$ in order to have real solutions. This corresponds to a minimum degree of nonlocality, σ_{NL}, below which this approach is not valid:

$$\sigma_{\mathrm{NL}}{}^2 = \frac{1}{\sqrt{2I}}. \tag{10.23}$$

For $A = \sqrt{I} = 5$, $\sigma_{\mathrm{NL}} \approx 0.3761$. We note that this choice of threshold value is somewhat arbitrary, as one could use other definitions of the relevant intensity based nonlinear length scale. Now, we simply solve $u = u_1 a^2 = I/2$, which gives us $a = \sqrt{\frac{I}{2u_1}}$ as the upper limit in the integral (10.21). Thus

$$\boxed{L_{\mathrm{NL}}^{\mathrm{int}} = \tfrac{1}{u_2} \int_0^{\sqrt{\frac{I}{2u_1}}} \frac{1}{\sqrt{(1-v^2)\left(1-k^2v^2\right)}} dv,} \tag{10.24}$$

with $u_{1,2}$ given by (10.17)–(10.18). We note that in the strongly nonlocal limit, $\sigma \to \infty$, $u_{1,2} \to I$, and k tends to unity, and the expression (10.13) is reencountered. Away from phase matching, $\sigma < \sigma_{\mathrm{NL}}$, the SH intensity does not reach half the total intensity and $L_{\mathrm{NL}}^{\mathrm{int}}$ is therefore undefined.

Phase shift-based nonlinear length, $L_{\mathrm{NL}} = L_{\mathrm{NL}}^{\mathrm{phase}}$

The expression (10.24) is not the only choice of a L_{NL} definition. From the relationships in (10.16), we see that the phase change of the FW now can be written (we still have $\mathcal{H} = 0$)

$$\frac{d\phi_1}{dz} = A_2 \cos\theta = A_2 \frac{\mathcal{H} - \beta u}{2(I-u)} = \frac{\beta}{2}\frac{u}{I-u} = \frac{\beta}{2}\left|\frac{E_2}{E_1}\right|^2, \tag{10.25}$$

with u given by (10.22) and $u_{1,2}$ by (10.17) and (10.18). We note that this is an oscillatory function.

Here, we can reuse the nonlinear length definition from the NLS case (10.11) on page 82: The *propagation distance that corresponds to a phase shift of π for the FW*,

$$\boxed{\left|\phi_1\left(L_{\mathrm{NL}}^{\mathrm{phase}}\right)\right| = \pi = \frac{\beta}{2}\int_0^{L_{\mathrm{NL}}^{\mathrm{phase}}} \frac{u}{I-u}.} \tag{10.26}$$

Then we can numerically integrate Eq. (10.25) to sample values of z, until the outcome π is found.

To summarize, we have the linear dispersion/diffraction length from (10.7), L_{D}, the nonlinear length defined from phase variation from (10.26), $L_{\mathrm{NL}} = L_{\mathrm{NL}}^{\mathrm{phase}}$, the nonlinear length defined from intensity variation from (10.24), $L_{\mathrm{NL}} = L_{\mathrm{NL}}^{\mathrm{int}}$, with the limiting value $L_{\mathrm{NL}} = L_{\mathrm{NL}}^{\mathrm{int}}\big|_{\beta=0}$ from (10.13) and finally the amplitude depending limiting value in the cascading NLS case $L_{\mathrm{NL}} = L_{\mathrm{NL}}^{\mathrm{NLS}}$ from (10.11). All are shown in Fig. 10.2.

For $\sigma > \sigma_{\mathrm{NL}}$ the nonlinear length is determined by the intensity variation, $L_{\mathrm{NL}} = L_{\mathrm{NL}}^{\mathrm{int}}$. For $\sigma < \sigma_{\mathrm{NL}}$ the nonlinear length is determined by the phase, $L_{\mathrm{NL}} = L_{\mathrm{NL}}^{\mathrm{phase}}$. Thus, in our simulations the nonlinear length is approximately $L_{\mathrm{NL}} = 0.18$ for $\sigma > 0.38$ and $L_{\mathrm{NL}} = L_{\mathrm{NL}}^{\mathrm{phase}} > 2.0$ for $\sigma < 0.38$.

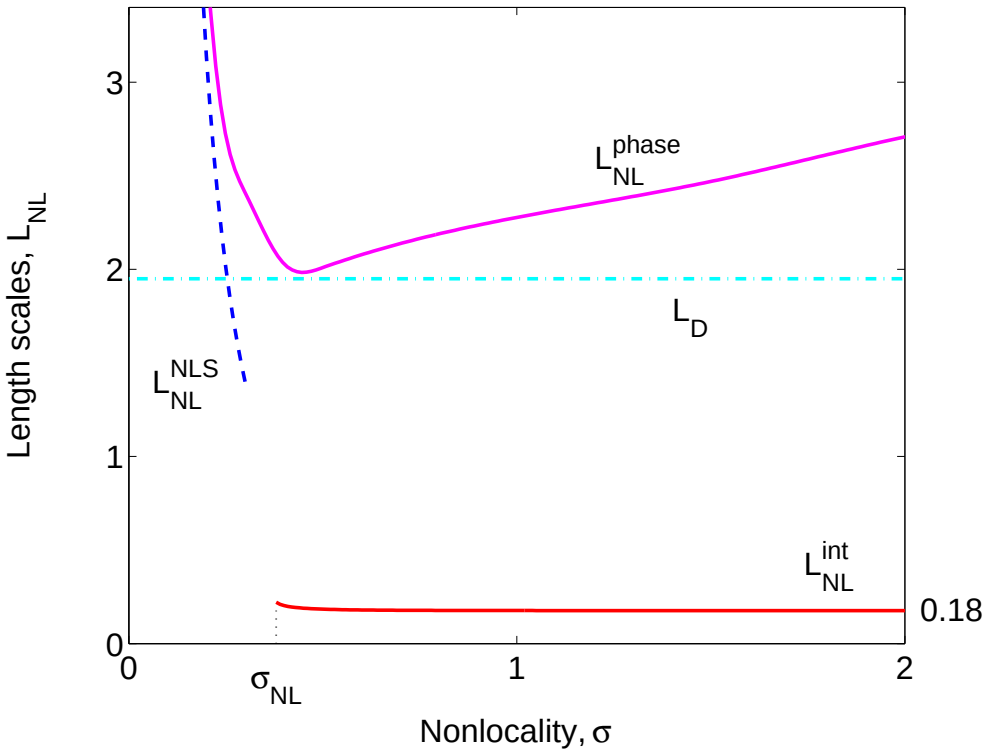

Figure 10.2: *The dependence of the nonlinear length on σ. Based on the intensity variation, the NLS approximation (10.11) is valid in the local case, for $\sigma > \sigma_{\rm NL} \approx 0.38$ (with $A = 5$), we have the expression (10.24). Based on phase modulation, one should use (10.26) which is valid for all degrees of nonlocality.*

Physically, one does not experience such an abrupt jump; rather it implies that the other measures of $L_{\rm NL}$ becomes important as well. Interestingly, we find that the nonlinear length related to the phase modulation is always longer than the linear diffraction length. For $\sigma < 0.2$, $L_{\rm NL}^{\rm NLS}$ is a good approximation of the nonlinear length $L_{\rm NL}^{\rm phase}$. At phase matching, $\beta = 0$, the exact solution to Eq. (10.25) has no phase variation and correspondingly the nonlinear length $L_{\rm NL}^{\rm phase}$ must go to infinity for $\sigma \to \infty$, which is confirmed in Fig. 10.2.

The propagation length should always be viewed relative to these length scales, e.g. stationary states can only be said to be achieved for propagation lengths longer than both. For our parameter values we have $L_D \approx 1.95$ and for $\sigma = 0.2$ [$\sigma = 0.5$] we have $L_{\rm NL}^{\rm phase}(0.2) \approx 3.14$ [$L_{\rm NL}^{\rm phase}(0.5) \approx 0.50$].

11

Accessible nonlocal (2+1)D solitons, anomalous SH dispersion

In the case of anomalous SH dispersion, $d_2 > 0$, the Fourier transformed response function (9.34) is positive definite (since we consider $s_\beta = +1$) and the response function in real space is found by computing the integral (11.1)

$$R_+(x,t) = \frac{1}{4\pi^2}\int_{-\infty}^{\infty}\int_{-\infty}^{\infty}\frac{1}{1+\sigma^2\left(k^2+\omega^2\right)}e^{-ik\sigma\bar{x}}e^{-i\omega\sigma\bar{t}}dkd\omega, \tag{11.1}$$

with $\beta = 1/\sigma^2$, $\bar{t} = t/\sigma$ and $\bar{x} = x/\sigma$. We first solve the inner integral:

$$I_k = \int_{-\infty}^{\infty}\frac{1}{1+\sigma^2\left(k^2+\omega^2\right)}e^{-ik\sigma\bar{x}}dk. \tag{11.2}$$

The integral in Eq. (11.2) is simplified using the definition of the complex exponential function and that the integral over the odd function $\sin(\bar{x}k)$ is zero. Also, due to the parity of the cosine function, the sign of $\bar{x}$ cannot have any effect and we must therefore use its absolute value. Symmetry and substitution $u = \sigma k$ then give us

$$I_k = \frac{2}{\sigma}\int_0^{\infty}\frac{\cos(\sigma|\bar{x}|k)}{\sqrt{1+\sigma^2\omega^2}^2+\sigma^2k^2}d\left(\sigma k\right), \tag{11.3}$$

which has the solution [57, Eq. 3.723.2]

$$I_k = \frac{2}{\sigma}\frac{\pi}{2\sqrt{1+\sigma^2\omega^2}}e^{-|\bar{x}|\sqrt{1+\sigma^2\omega^2}}. \tag{11.4}$$

This is now inserted in the outer integral of (11.1), and we also use the parity of the complex exponential function to reduce it to

$$R_+(x,t) = 2\frac{1}{4\pi\sigma^2}\int_0^{\infty}\frac{\cos(|\bar{t}|\sigma\omega)}{\sqrt{1+\sigma^2\omega^2}}e^{-|\bar{x}|\sqrt{1+\sigma^2\omega^2}}d(\sigma\omega), \tag{11.5}$$

where we have used the substitution $v = \sigma\omega$. The result of this integral is found in the literature and has the solution [57, Eq. 3.961.2]:

$$R_+(x,t) = \frac{1}{2\pi\sigma^2} K_0\left(\frac{1}{\sigma}\sqrt{t^2+x^2}\right), \quad (x,t) \neq (0,0), \tag{11.6}$$

where we have returned to the "un-barred" variables and where K_0 is the modified Bessel function of the second kind, see Fig. 11.1. We note that this solution may also be found through integration in the complex plane.

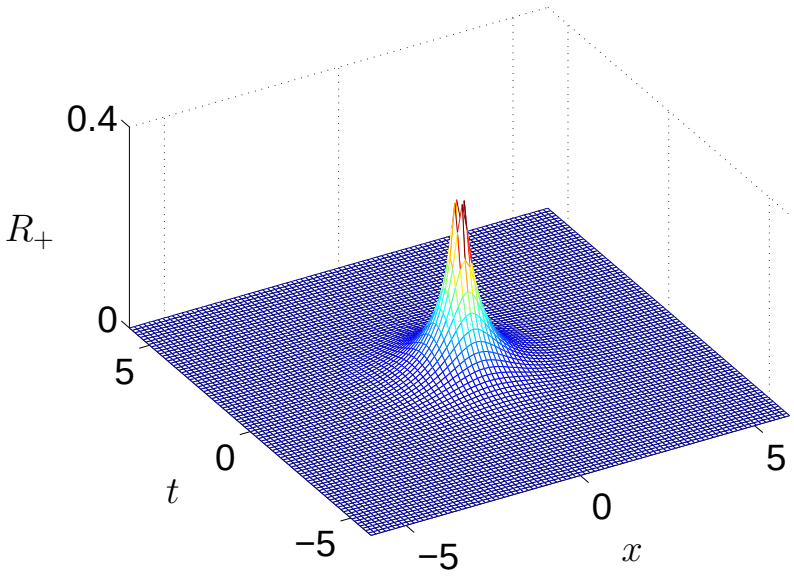

Figure 11.1: *Response function $R_+(x,t)$ for anomalous SH dispersion given by Eq. (11.6). The degree of nonlocality is $\sigma = 1$ in this plot.*

We note how σ governs the degree of nonlocality of the solution (see Fig. 11.3) and also the similarity to the one dimensional response function $R(x) = (2\sigma)^{-1}\exp(-|x|/\sigma)$ (9.27). The term "similarity" is used here in the sense that the shape of the current Bessel $K_0\left(\sqrt{t^2+x^2}\right)$-function somewhat resembles the revolution of the function $\exp(-|x|/\sigma)$ around the axis $x = 0$, except that we now have a singularity at origo.

Note the contour plots in Fig. 11.2, showing the effect of σ on R_+, and compare with the contour plots of the dipole-dipole interaction in Fig. 3.4 on page 21 in Part I. The same 50 equidistant

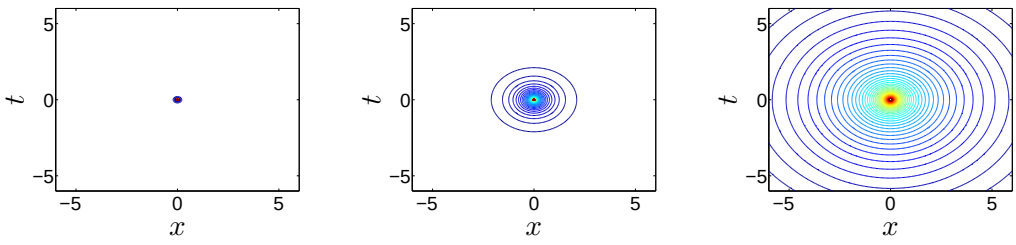

(a) $\sigma = 0.1$ (b) $\sigma = 1$ (c) $\sigma = 10$

Figure 11.2: *Contour plots of the response function $R_+(x,t)$ for different σ. 50 equidistant contours from 0.1 to 5. Compare with Fig. 3.3 on page 20.*

contours are plotted in all cases (a)–(c) of Fig. 11.2, and we see how the effect is very local for $\sigma = 0.1$, but widens to fill the entire window at $\sigma = 10$. It should be apparent how the nonlocality is in play in both cases — in the molecular model, the geometry introduces a new "branch" in the contour plots of the long-range interaction of the DNA model; here, the nonlocality is a radially symmetric effect.

In the strongly nonlocal limit, as $\sigma \to \infty$, the response function broadens to eventually fill the entire $x - t$ plane, see Fig. 11.3. In this limit, Eqs. (9.32)-(9.33) become effectively linear,

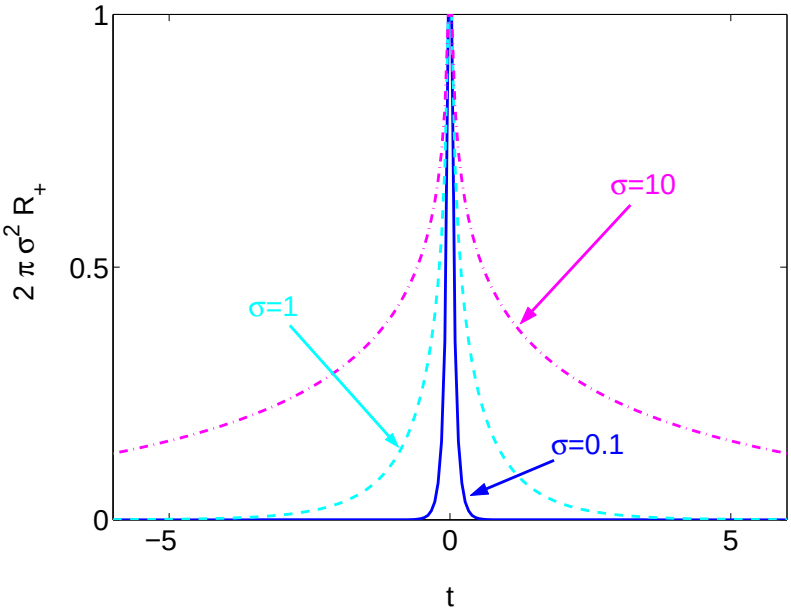

Figure 11.3: *The effect of nonlocality, σ, on the response function $R_+(x,t)$ for anomalous, $d_2 = 1$ SH dispersion. The plot is made for constant $x = 0$.*

as the response function can be approximated by its series expansion and reduced to the form of Eq. (9.40). Thus the so-called *accessible solitons* (see below and Ref. [61]) of the linear system (9.40) also exist in this 2+1D case. In the 1+1D case, the response function was non-differentiable in origo [43], whereas in the 2+1D case we see that it is undefined in origo. Nevertheless, the characteristics of the Bessel K_0-function allows us to normalize the response function and thus find a valid expression of the form (9.40).

Conversely, in the local limit, $\sigma \to 0$, corresponding to the cascading limit, the response function approaches a δ–function, yielding the NLS equation (9.31) for the FW. We note that for large arguments of Bessel K_0-function we have the expansion [57, 8.451.6]

$$K_\nu(z) = \sqrt{\frac{\pi}{2z}} e^{-z} \left[\sum_{k=0}^{n-1} \frac{1}{(2z)^k} \frac{\Gamma\left(\nu + k + \frac{1}{2}\right)}{k!\Gamma\left(\nu - k + \frac{1}{2}\right)} + \theta_3 \frac{\Gamma\left(\nu + n + \frac{1}{2}\right)}{(2z)^n n!\Gamma\left(\nu - n + \frac{1}{2}\right)} \right], \tag{11.7}$$

with some θ_3 depending on the argument of z. For $\nu = 0$ we have the Γ-functions [57, 8.339.2 and

8.339.3][1]

$$\begin{aligned}\Gamma\left(\frac{1}{2}+k\right) &= \frac{\sqrt{\pi}}{2^k}(2n-1)!! \\ \Gamma\left(\frac{1}{2}-k\right) &= (-1)^k\frac{2^k\sqrt{\pi}}{(2n-1)!!}\end{aligned}$$

and thus

$$K_0(z)=\sqrt{\frac{\pi}{2z}}e^{-z}\left[\frac{\Gamma\left(\frac{1}{2}\right)}{\Gamma\left(\frac{1}{2}\right)}+\frac{1}{2z}\frac{\Gamma\left(\frac{3}{2}\right)}{\Gamma\left(-\frac{1}{2}\right)}+\cdots\right]\approx\sqrt{\frac{\pi}{2z}}e^{-z}\left[1-\frac{1}{2z}\frac{\frac{1}{2}\sqrt{\pi}}{-2\sqrt{\pi}}\right].$$

With the argument $\frac{1}{\sigma}\sqrt{t^2+x^2}$ we then get

$$R_+(x,t)=\frac{1}{\sqrt{8\pi}}\frac{1}{\sqrt[4]{t^2+x^2}}\frac{1}{\sigma^{3/2}}e^{-\sqrt{t^2+x^2}/\sigma}\left[1-\frac{1}{8}\frac{\sigma}{\sqrt{t^2+x^2}}+\cdots\right], \tag{11.8}$$

and we see that for $(x,t)\neq(0,0)$, R_+ tends to zero for decreasing σ; only at $(x,t)=(0,0)$ the response function grows to infinity. Also, despite the singularity at origo, the indefinite integral of the modified Bessel function of the second kind, K_0, is convergent with the value 2π. This is most easily seen by converting to polar coordinates.

$$\begin{aligned}\int_{-\infty}^{\infty}\int_{-\infty}^{\infty}R_+(x,t)dxdt &= \int_{-\infty}^{\infty}\int_{-\infty}^{\infty}\frac{1}{2\pi\sigma^2}K_0\left(\frac{1}{\sigma}\sqrt{t^2+x^2}\right)dxdt \\ &= \int_0^{2\pi}\int_0^{\infty}\frac{1}{2\pi\sigma^2}K_0\left(\frac{1}{\sigma}\rho\right)\rho d\rho d\phi \\ &= \int_0^{\infty}\frac{2\pi}{2\pi\sigma^2}K_0\left(\frac{1}{\sigma}\rho\right)\rho d\rho \\ &= 1,\end{aligned} \tag{11.9}$$

since we have [57, Eq. 6.561.16]

$$\int_0^{\infty}x^{\mu}K_{\nu}(ax)=2^{\mu-1}a^{-\mu-1}\Gamma\left(\frac{1+\mu+\nu}{2}\right)\Gamma\left(\frac{1+\mu-\nu}{2}\right)$$

which here gives us

$$\int_0^{\infty}\rho K_0\left(\frac{1}{\sigma}\rho\right)=\frac{1}{\sigma^2}\Gamma(1)^2=\frac{1}{\sigma^2}.$$

This ensures that the normalization condition

$$\int_{-\infty}^{\infty}\int_{-\infty}^{\infty}R_+(x,t)\,dxdt=1 \tag{11.10}$$

is fulfilled, and we have thus shown that R_+ indeed approaches a δ–function in the local limit. In other words, the conventional cascading limit, $e_2=E_1^2/\beta$, applies also in this 2+1D case, yielding the 2+1D NLS Eq. (9.31).

Originally, the term "accessible solitons" was used to describe the strongly nonlocal linear limit (9.40) in the case of anomalous SH dispersion [61]. We are using the term *accessible nonlocal*

[1]With the "double faculty" $n!!=n\cdot(n-2)\cdot(n-4)\cdot\ldots\cdot3\cdot1$.

solitons in a broader sense here, where it refers to $d_2 > 0$ and the whole regime of σ-values, because in this case the response function is simple and simple equations and physical explanations may be obtained in both the local and nonlocal limit. As we shall see in Sec. 12, this is in contrast to the normal SH dispersion case, $d_2 < 0$, where these properties are not present. For normal dispersion we therefore use the term *inaccessible nonlocal solitons*.

Based on the form of the equation for the FW, two separate cases can be considered, namely the FW dispersion being normal or anomalous, while the SH dispersion is $d_2 = +1$. These are discussed in the subsections below.

11.1 Light bullet case, anomalous FW and anomalous SH dispersion

The case of normal dispersion in both fields, $d_1 > 0$ and $d_2 > 0$, is an augmented version of FW light bullets [22, 24]. The FW case was investigated in a nonlocal setting, where the response function was found to be shaped like $\exp(-|x|/\sigma)$ (Eq. 9.27 and [43]); σ being the degree of nonlinearity. This is a good starting point for our investigations, as the FW dynamics is well understood. The present setting is expected to give a somewhat similar response, keeping in mind, of course, that we now have an additional dimension to consider.

11.1.1 Weak nonlocality, $\sigma \ll 1$

As discussed in the beginning of this Chapter, the weakly nonlocal limit can be approximated by the NLS equation, and in this way we have something to compare our results with. In Fig. 11.4, the evolution of the FW is depicted for $\sigma = 0.1$ for propagation lengths $z = 0, 2$ and 4. As a low degree of nonlocality also implies a low degree of nonlinearity, we see a pulse, which spreads in a fashion similar to the on of the linear case. A small degree of nonlocality corresponds to a small width of the response function, σ (here $\sigma = 0.1$), relative to the initial beam width, B (here $B = 3$). With these values, the nonlinear length is about $L_{\mathrm{NL}} = 12.6$ (outside of the range in Fig. 10.2), so not even one third of a nonlinear length has been traversed and no nonlinear effect seen. $z = 4$ corresponds to two linear dispersion lengths, $L_{\mathrm{D}} \approx 1.95$, and the dispersion is apparent in Fig. 11.4.

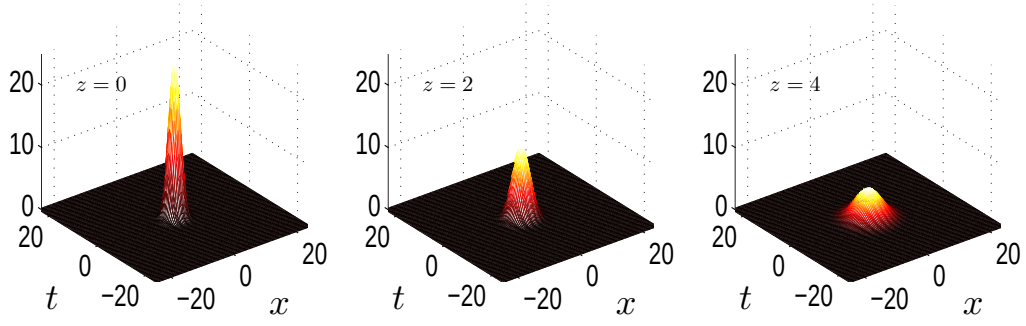

Figure 11.4: *Evolution of the FW intensity in the cascading NLS limit for $\sigma = 0.1$ and shown at propagation distance $z = 4$. $d_1 = 1$, and $d_2 = 1$ for $z = 0, 2, 4$. Parameter values are $A = 5$, $B = 3$.*

In the NLS limit, the SH is slaved to the FW. Thus, the SH dispersion parameter, d_2, should be of no importance for outcome of the simulations. This is confirmed in Fig. 11.5, where the top row depicts the result of a pure NLS equation and the bottom row the outcome of a simulation of

Eqs. (9.29)–(9.30) for $\sigma = 0.1$ at propagation length $z = 4$. We show not only the case $d_1 = d_2 = +1$, but all combinations of the dispersion parameters d_1 and d_2. We use contour plots instead of the surface plot in Fig. 11.4 for easier comparison. Unless stated otherwise, we use logarithmically spaced contour lines as we will be looking for small amplitude phenomena. In Fig 11.5, the lowest contour is at $|E_1|^2 = 10^{-3}$ with 25 contours in total up to the maximum intensity of the plot. Note that the lower right plot in Fig. 11.5 is a contour version of the right surface plot in Fig. 11.4.

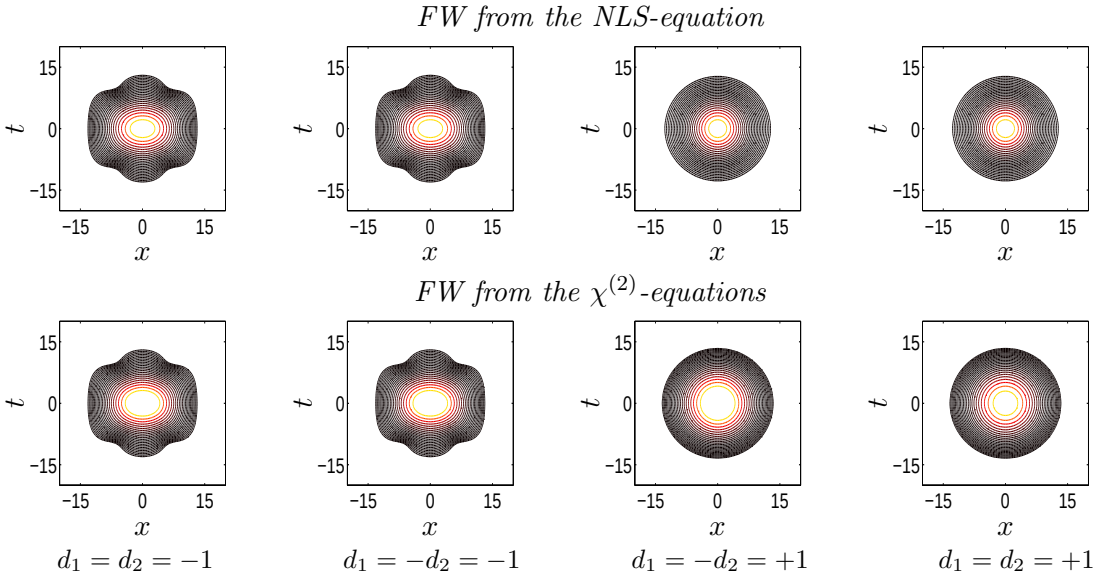

Figure 11.5: *Comparison between the cascading NLS limit (9.31) and the full equations (9.29)–(9.30) solved for $\sigma = 0.1$ and the FW intensity is shown at propagation distance $z = 4$. Top row: NLS. Bottom row: Full equations. $d_1 = 1$, and $d_2 = 1$ for $z = 0$ to $z = 4$. 25 contour lines from 10^{-3} to the maximal intensity. Parameter values are $A = 5$, $B = 3$.*

As expected, the NLS approximation corresponds well to the full solutions, and we see no difference between the NLS cases with different d_2. We stress that the cascading limit is a *local* description of the dynamics; in the cascading limit, the field values at a given point are determined only by its values very close to that point. This is beautifully represented by the δ-limit of the response function, R_+, shown in the previous Section 9.2.

11.1.2 Strong nonlocality, $\sigma \gg 1$

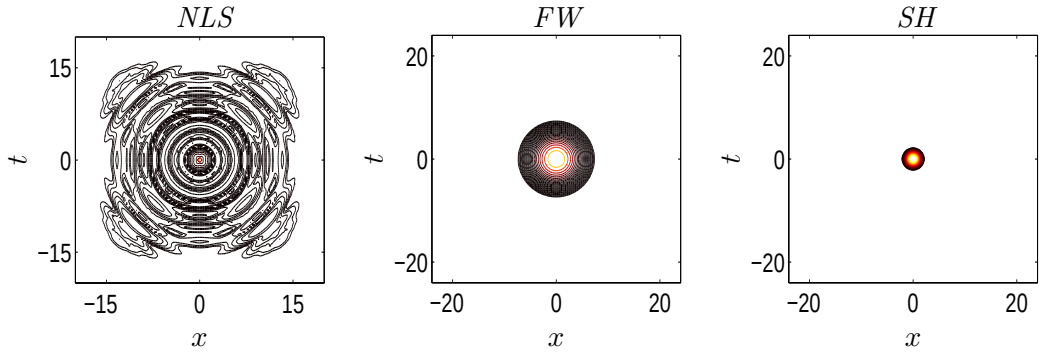

Figure 11.6: *Comparison between the cascading NLS limit (9.31) and the full equations (9.29)–(9.30) for $\sigma = 0.5$ and $z = 1$ in the light bullet case, $d_1 = d_2 = 1$. On the left is the NLS solution, in the middle the FW of the full solution and to the right the SH of the full solution. 25 contour lines from 10^{-3} to the maximal intensity. Parameter values are $A = 5$, $B = 3$.*

For just a slightly larger degree of nonlocality, however, the situation changes drastically; see Fig. 11.6. Here the degree of nonlocality is $\sigma = 0.5$ and we see how the difference between the NLS on the left and the FW calculated from the full $\chi^{(2)}$-equations in the middle is very pronounced, even for this seemingly modest increase of nonlocality. But now the nonlinear length is $L_{\mathrm{NL}} = L_{\mathrm{NL}}^{\mathrm{int}} \approx 0.18$, and already at $z = 1$, 5 nonlinear lengths have been traversed. The simulations are halted here ($z = 1$) to avoid boundary effects. Considering the SH on the right we see that the expression $e_2 = E_1^2/\beta$ is clearly invalid, as the resemblance between the shape of the fields is minimal.

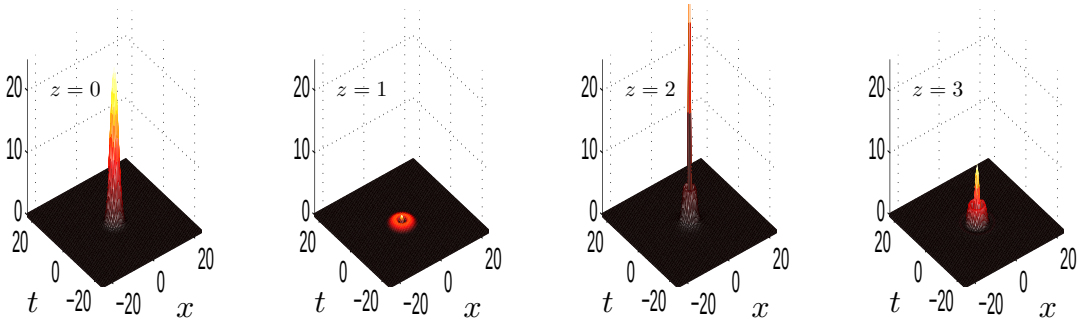

Figure 11.7: *The evolution of the FW profile, $|E_1|^2$, in the strongly nonlocal light bullet case, $\sigma = 10$, $d_1 = 1$, and $d_2 = 1$ for $z = 0$ to $z = 4$. Parameter values are $A = 5$, $B = 3$.*

With a stronger degree of nonlocality and nonlinearity, $\sigma = 10$, we abandon the NLS limit and consider now the outcome of simulations with the full equations (9.29)–(9.30). For this degree of nonlocality, the nonlinear length calculated from the intensity becomes $L_{\mathrm{NL}}^{\mathrm{int}} \approx 0.18$, while both the linear length, L_{D}, and the nonlinear phase length are close to 2. The evolution of FW intensity in Fig. 11.7 shows a temporary increase before a stationary state is achieved. We see a strong resemblance with the *ringing* structures found in Ref. [22] for strong nonlinearities. Since both the FW and the SH dispersion are positive, we expect the shape of the corresponding intensities to be similar. This is confirmed in Fig. 11.8.

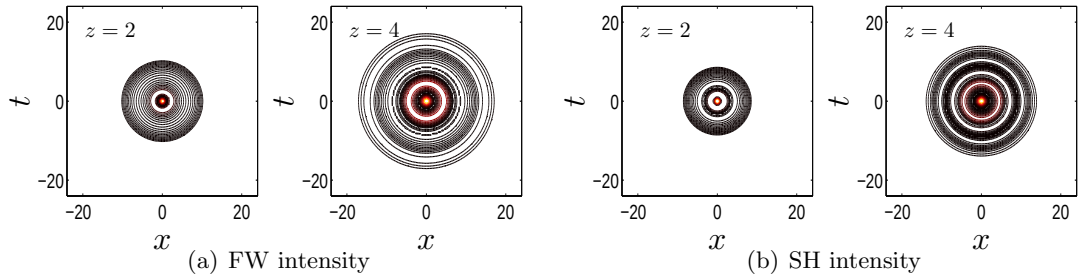

(a) FW intensity (b) SH intensity

Figure 11.8: *The evolution of the FW and SH intensities in the strongly nonlocal light bullet case,* $\sigma = 10$, $d_1 = d_2 = 1$ *for* $z = 2$ *and* $z = 4$. *Parameter values are* $A = 5$, $B = 3$. *Contour plots with 25 logarithmically spaced lines from* 10^{-3} *to the maximal intensity.*

In conclusion, the light bullet case has for shown that the NLS approximation seizes to be valid already at quite small degrees of nonlocality. The simulations with anomalous dispersion in both the FW and SH showed correspondence with previous work on light bullets in the FW regime [22, 64].

11.2 Modified X-wave case, normal FW and anomalous SH dispersion

We now consider a case of *mixed* dispersion effects, in the sense that the FW and SH dispersion parameters have opposite sign. We denote the case of normal FW ($d_1 = -1$) and anomalous SH ($d_2 = +1$) dispersion the *modified X-wave* case because the linear part of the FW equation supports X-waves for $d_1 < 0$ [27, 38, 65] and nothing is suggested otherwise based on the cascading limit. However, we suspect that the inclusion of the SH field will blur this effect somewhat because the SH does not support a linear X-wave for $d_2 > 0$. Hence we have two effects counteracting each other. For example a sufficiently broad response function could make the branches of an X-wave in the FW feel each other and thereby either suppress the X-wave (by blurring it too much) or e.g. alter its cone angle.

11.2.1 Weak nonlocality, $\sigma \ll 1$

We have already shown that the NLS equation of the cascading limit is an invalid approximation of the $\chi^{(2)}$-equations, even for seemingly modest values of σ. Nevertheless, the NLS is known to support X-waves (see e.g. [38]). We therefore perform yet another simulation close to the cascading limit, but this time with $d_1 = -1$.

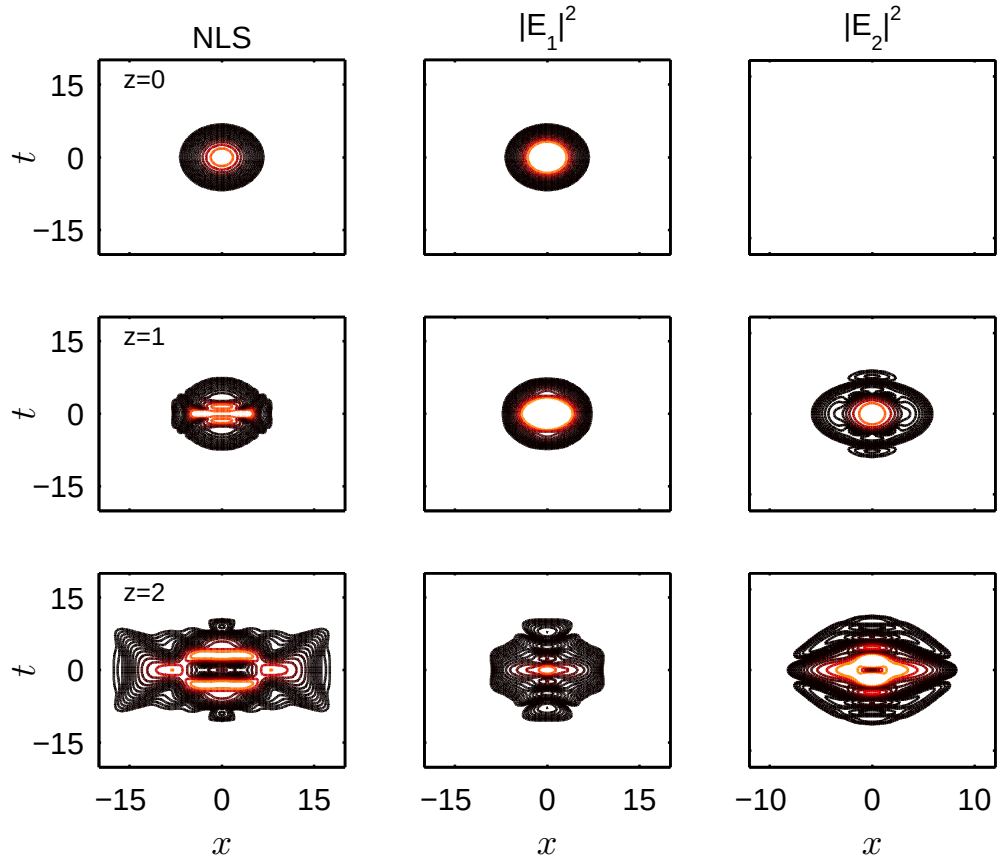

Figure 11.9: *Intensity profiles at different propagation lengths for the modified X-wave case with a modest degree of nonlocality $\sigma = 0.5$. Parameter values are: $A = 5, B = 3$, $d_1 = -1$, and $d_2 = +1$. NLS FW Eq. (9.31) (left). Full equations (9.29)–(9.30) solved for $|E_1(x,t)|^2$ (center) and $|E_2(x,t)|^2$ (right). 15 contour lines from 0.001 logarithmically separated to the maximum intensity.*

In Fig. 11.9 we again compare the full model with the cascading limit NLS equation for $\sigma = 0.5$. Clearly, the cascading limit no longer provides a good approximation as for $\sigma = 0.1$ in Fig. 11.5 (second column from the left in Fig. 11.5 on page 92) and simulations are stopped at $z = 2$. In agreement with Ref. [38] Fig. 11.9 shows that the NLS equations supports X waves. Here it is more clearly formed than in the case $\sigma = 0.1$ in Fig. 11.5, because the nonlinear length for $\sigma = 0.5$ is now $L_{\mathrm{NL}}^{\mathrm{NLS}} = 0.5$, which is much shorter than for $\sigma = 0.1$, where the nonlinear length is as large as $L_{\mathrm{NL}}^{\mathrm{NLS}} = 12.6$. In contrast, no X is observed in the full model for $\sigma = 0.5$ (middle column of Fig. 11.9). This is supported by the appropriate nonlinear phase length $L_{\mathrm{NL}} = L_{\mathrm{NL}}^{\mathrm{phase}} \approx 2.0$ and it is just on the border where the nonlinear intensity length sets in.

11.2.2 Strong nonlocality, $\sigma \gg 1$

The result of the same simulation, $d_1 = -1$ and $d_2 = +1$, but with a strong nonlocality, $\sigma = 10$, is shown in Fig. 11.10. The linear length is as before $L_{\mathrm{D}} = 1.95$, but in this case we should compare the propagation distance to the nonlinear length scale originating from the intensity, $L_{\mathrm{NL}} = L_{\mathrm{NL}}^{\mathrm{int}} \approx 0.2$. At $z = 4$, we have therefore evolved about 20 nonlinear lengths, and it is clear that the nonlinear contributions have had effect, as we observe biconical emission of radiation and that an X-shape is formed.

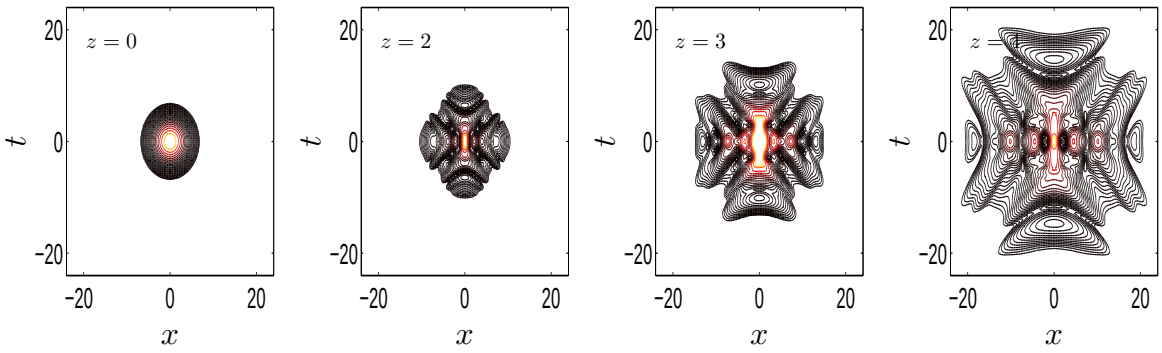

Figure 11.10: *Intensity profile of the FW, $|E_1(x,t)|^2$, at different propagation lengths for the modified X-wave case for $\sigma = 10$. Parameter values are: $A = 5, B = 3$, $d_1 = -1$, and $d_2 = +1$. 25 contour lines from 0.001 logarithmically separated to the maximum intensity.*

From the lengths scales shown in Fig. 10.2 it is apparent that σ should be larger than 1 to obtain a strong nonlinear and nonlocal attractor, with a small nonlinear length determined by the amplitude, $L_{\mathrm{NL}} = L_{\mathrm{NL}}^{\mathrm{int}} \approx 0.2$. In Fig. 11.11 we continue the propagation out to $z = 8$, corresponding to 4 diffraction lengths and 40 nonlinear lengths and we compared to the profile of the SH. In order to avoid problems with radiation reaching the boundaries, this simulation is made on a $-50 < x, t < 50$ grid with 360×360 grid points. An X-shape in the FW is now clearly observed. In contrast, an X is not formed in the SH and thus a stationary state has not yet been reached. For $d_2 = +1$ we note that the response function is *not* X-shaped and so the formation of the X in the FW is counteracted by the lack of X in the SH. For the parameters considered, the FW X prevails. We note that compared to the outcome of a simulation with $d_1 = d_2 = -1$ of Sec. 12.2, this X-shape appears somewhat broader. It seems that the SH response function drives this effect.

The degree of nonlocality, σ, appears in the nonlinear length scale only because it also determines the strength of the nonlinearity, γ, not because it describes the width of the response

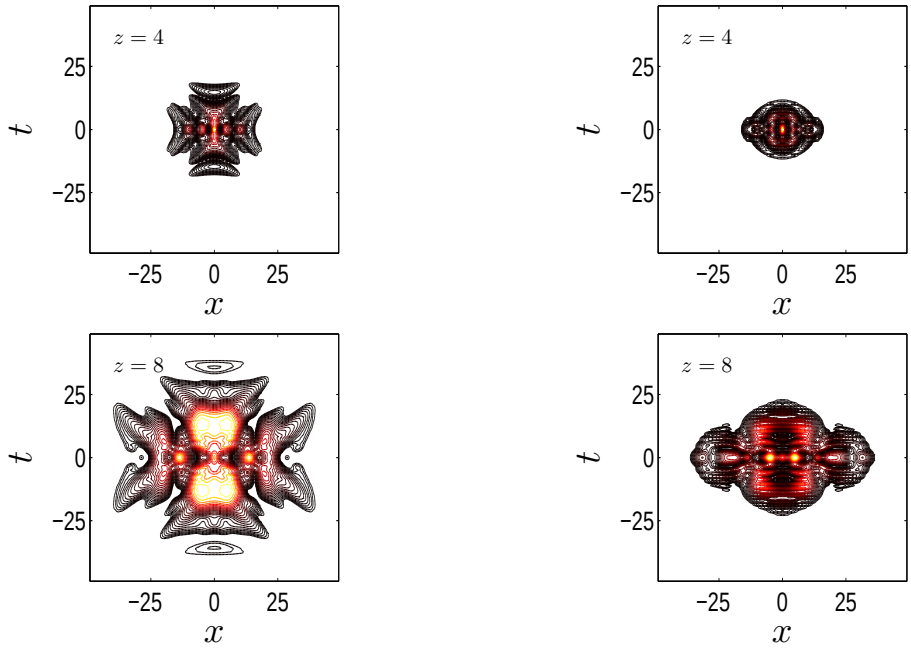

Figure 11.11: *Intensity profiles for the (left) FW, $|E_1|^2$, and (right) SH, $|E_2|^2$, at propagation lengths (top) $z = 4$ and (bottom) $z = 8$. Parameter values are: $A = 5, B = 3$, $d_1 = -1$, $d_2 = +1$, and $\sigma = 10$,* i.e., *strongly nonlocal. 25 contour lines from 0.005 logarithmically separated to the maximum intensity.*

function. However, the width of the response function is clearly important, because it determines the transverse "coupling length" over which parts of the beam can feel each other. Because the nonlinearity depends on σ^2, we expect that σ at least should be larger than 1 to generate X-waves, because then the nonlinearity is at least of the same order of magnitude as the nonlocality. This is also confirmed in the simulations with $\sigma = 0.5$ and 10, presented in Figs. 11.9–11.11.

In any case, the observation of an X-wave for $\sigma = 10$ represents the first observation of X-wave generation in quadratic nonlinear materials with anomalous dispersion at the SH.

The relative magnitudes of the FW and SH can be appreciated in Fig. 11.12. They are of the same order. As is expected, the X wave effect is small compared to the center intensity. It is

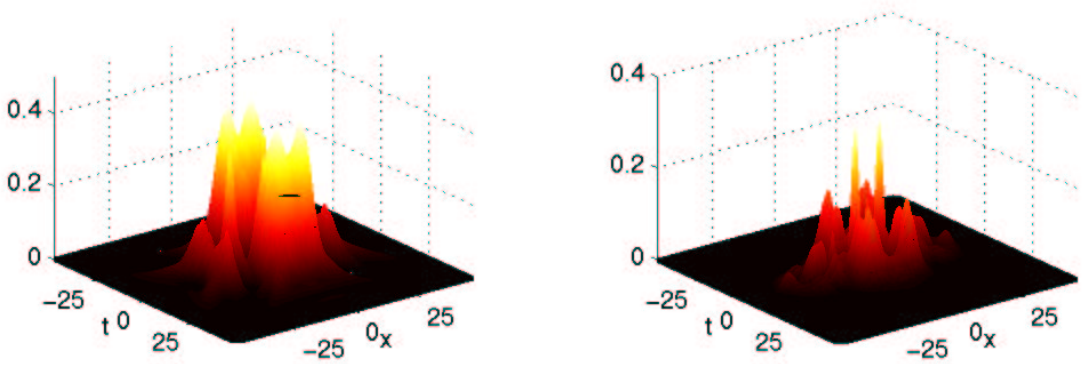

(a) FW intensity,$|E_1|^2$ (b) SH intensity, $|E_2|^2$

Figure 11.12: *The FW and SH profiles,* $|E_1|^2$*, in the strongly nonlocal modified X wave case,* $\sigma = 10$*,* $d_1 = -d_2 = -1$ *at* $z = 8$*. Parameter values are* $A = 5$*,* $B = 3$*.*

somewhat more informative to view a contour plot with logarithmically spaced level curves (as has been done previously). In Fig. 11.13, a contour plot is superimposed on a surface plot as the one in Fig. 11.12(a) and viewed from above.

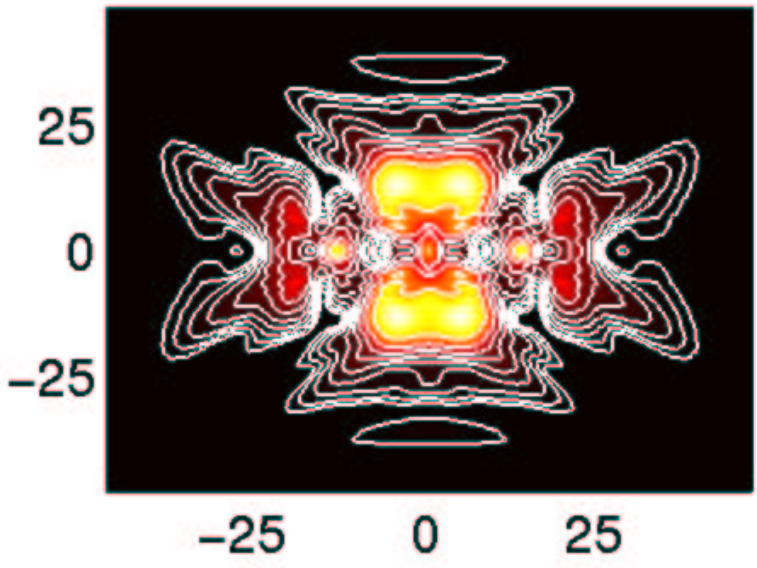

Figure 11.13: *The FW profile,* $|E_1|^2$*, in the strongly nonlocal modified X wave case,* $\sigma = 10$*,* $d_1 = -d_2 = -1$ *at* $z = 8$*. Parameter values are* $A = 5$*,* $B = 3$*. Surface plot viewed from above with a contour plot with 10 logarithmically spaced lines from 0.005 to the maximal intensity.*

12

Inaccessible nonlocal (2+1)D solitons, normal SH dispersion

In the case of normal SH dispersion, $d_2 < 0$, with positive β, the situation is fundamentally different from the anomalous dispersion case discussed in the previous Section 11. The Fourier transformed response function is now ($s_\beta = -d_2 = +1$)

$$\widetilde{R}_{-}(k,\omega) = \frac{1}{1+\sigma^2\left(k^2-\omega^2\right)}. \tag{12.1}$$

Clearly, $\widetilde{R}_{-}$ now has an X-shape, as illustrated in Fig. 12.1.

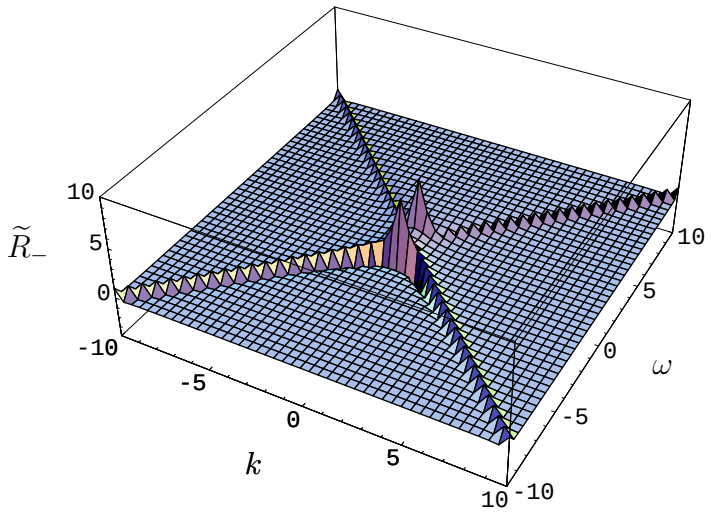

Figure 12.1: *Response function in the Fourier domain, $\widetilde{R}_{-}(k,\omega)$, for $d_2 = -1$, $s_\beta = 1$ and $\sigma = 1$. Note that the function is singular for $\omega\sigma = \pm\sqrt{1+\sigma^2 k^2}$.*

The response function in real space, R_-, is found analogously to R_+ in Sec. 11. In this case, the integration is carried out with respect to ω first, and with [57, Eq. 3.723.9] we get

$$R_-(x,t) = \frac{1}{4\pi\sigma}\int_0^\infty \frac{\sin(|\bar{t}|\sqrt{1+\sigma^2k^2})}{\sqrt{1+\sigma^2k^2}} e^{-|\bar{x}|\sigma^2k^2} dk. \tag{12.2}$$

Through substitution and parity, we see from [57, 3.876.1] that the response function is piecewise

$$R_-(x,t) = \begin{cases} \frac{1}{4\sigma^2} J_0\left(\frac{1}{\sigma}\sqrt{t^2-x^2}\right) & \text{for} \quad |x|<|t| \\ 0 & \text{for} \quad |x|>|t| \end{cases}, \tag{12.3}$$

where J_0 is the Bessel function of the first kind of zeroth order. We see that the response function in the normally dispersive case is oscillatory in nature and with an X-shaped profile (see Fig. 12.2). The X-shape is given by the lines $|x| = |t|$ corresponding to where the Fourier transformed response function, $\widetilde{R}_-$, is singular. The cone angle can be determined by linear analysis [33].

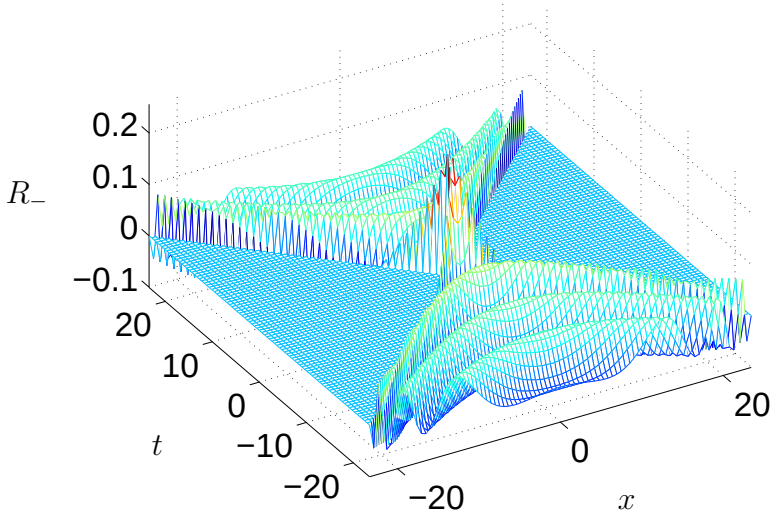

Figure 12.2: *The response function $R_-(x,t)$ [Eq. (12.3)] in the normally dispersive case $d_2 = -1$ for $\sigma = 1$. Compare with Fig. 11.1.*

The effect of σ for normal SH dispersion is depicted in Fig. 12.3, where R_- is plotted for constant $x = 0$. We see how σ governs the oscillation period of the J_0-function and how for sufficiently large values of σ, the central "hump" broadens to engulf the entire domain of definition for the fields. It is thus apparent how σ also describes the degree of nonlocality in the case of R_- [see Fig. 12.3(b)].

We note from Eq. (12.3) that in the real space the response function is undefined along the lines $|x| = |t|$. Therefore, the response function is *not* sufficiently smooth and subsequently, the approximation one makes to obtain the strongly nonlocal linear limit is not valid here. Thus no accessible solitons are expected, in contrast to the case of anomalous SH dispersion.

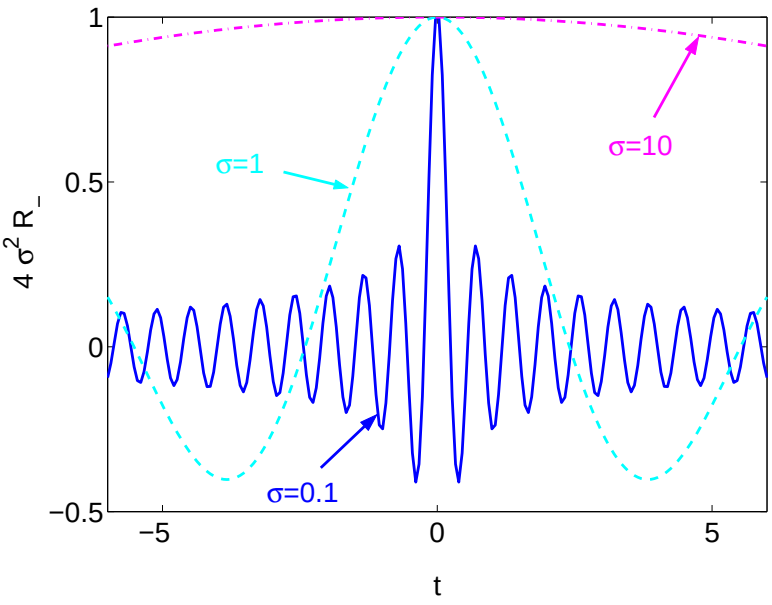

Figure 12.3: *The effect of nonlocality, σ, on the response function $R_-(x,t)$ for normal SH dispersion, $d_2 = -1$. The plot is made for constant $x = 0$.*

For large arguments the zeroth order Bessel function of the first kind can be approximated as [57, 8.451.1]

$$\begin{aligned} J_0(z) &= \sqrt{\frac{2}{\pi z}}\left\{\cos\left(z-\frac{\pi}{4}\right)\sum_{k=0}^{n-1}\frac{(-1)^k}{(2z)^{2k}}\frac{\Gamma\left(2k+\frac{1}{2}\right)}{\Gamma\left(-2k+\frac{1}{2}\right)} - \sin\left(z-\frac{\pi}{4}\right)\sum_{k=0}^{n-1}\frac{(-1)^k}{(2z)^{2k+1}}\frac{\Gamma\left(2k+\frac{3}{2}\right)}{\Gamma\left(-2k-\frac{1}{2}\right)}\right\} \\ &= \sqrt{\frac{2}{\pi z}}\left\{\cos\left(z-\frac{\pi}{4}\right)\left(1-\frac{1}{(2z)^2}\frac{\Gamma\left(\frac{5}{2}\right)}{\Gamma\left(-\frac{3}{2}\right)}+\ldots\right) - \sin\left(z-\frac{\pi}{4}\right)\left(\frac{1}{2z}\frac{\Gamma\left(\frac{3}{2}\right)}{\Gamma\left(-\frac{1}{2}\right)}+\ldots\right)\right\} \end{aligned}$$

With the argument $\frac{1}{\sigma}\sqrt{t^2-x^2}$ and retaining only the lowest order term, we can approximate the response function as

$$R_-(x,t) = \frac{\sigma^{-\frac{3}{2}}}{\sqrt{8\pi}}\frac{1}{\sqrt[4]{t^2-x^2}}\cos\left(\frac{\sqrt{t^2-x^2}}{\sigma}-\frac{\pi}{4}\right). \tag{12.4}$$

For simplicity, consider the case $x = 0$: We see that as $\sigma \to 0$, R_- tends to infinity if t is small. But we also see that for very large t, the response function does not approach zero in this limit. Finally, the singularity at $|x| = |t|$ is another reason why we do not recover a δ–function in the local limit for normal SH dispersion. This means that the cascading limit is not applicable in this case.

More formally, integration over the whole domain may begin with integration at some fixed t_0 with respect to x and

$$\int_{-\infty}^{\infty} R_-(x,t_0)dx = \int_0^{t_0} \frac{1}{4\sigma^2} J_0\left(\frac{1}{\sigma}\sqrt{t_0^2-x^2}\right) dx$$

With the substitutions $x = \sigma y$ and $y_0 = t_0/\sigma$, we get

$$\int_{-\infty}^{\infty} R_-(x,t_0)dx = \frac{1}{2\sigma}\int_0^{t_0} J_0\left(\sqrt{y_0^2-y^2}\right) dy = \frac{1}{2\sigma}\sin\left(\frac{t_0}{\sigma}\right)$$

by [57, Eq. 6.517]. Finally, the full normalization integral becomes

$$\int_{-\infty}^{\infty}\int_{-\infty}^{\infty} R_-(x,t)dxdt = \lim_{t_0\to\infty} 2\int_0^{t_0} \frac{1}{2\sigma}\sin\left(\frac{t}{\sigma}\right)dt = \lim_{t_0\to\infty}\left[1-\cos\left(\frac{t_0}{\sigma}\right)\right], \tag{12.5}$$

and we see that as t_0 goes to infinity, the value of the normalization integral oscillates between 0 and 2 for fixed σ; hence X-wave spatiotemporal beams are not normalizable [38].

Thus, normal SH dispersion is fundamentally different from the anomalous case, since the response function does not have a δ-function limit for $\sigma \to 0$, nor is it smooth enough to formally allow for a strongly nonlocal linear limit, $\sigma \to \infty$, and nor is it normalizable. We therefore use the term *inaccessible nonlocal solitons* for the localized wave solutions with normal SH dispersion.

12.1 Spectral analysis

In a linear setting, we can derive some insight by considering the dispersion relation, which is obtained by inserting $E_j = A_j \exp\left[j\left(ikx + i\omega t - ik_z z\right)\right], j = 1,2$ into the linearized versions of Eqs. (9.29)-(9.30). Fourier transformation then yield

$$\begin{aligned} -k_z\widetilde{E}_1^2 - 2k^2\widetilde{E}_1^2 - 2d_1\omega^2\widetilde{E}_1^2 &= 0, \\ -2k_z\widetilde{E}_2^2 - 4k^2\widetilde{E}_2^2 - 4d_2\omega^2\widetilde{E}_2^2 &= 0, \end{aligned}$$

and we get for the FW and SH, respectively:

$$k_z/2 = k^2 + d_1\omega^2, \tag{12.6}$$
$$k_z/2 = k^2 + d_2\omega^2. \tag{12.7}$$

Thus, for d_j negative, we find hyperbolas ($k^2 - \omega^2 = k_z/2$); for d_j positive, the curves become circles (Fig. 12.4). So we can have combinations of hyperbolas and circles as dictated by the signs of the dispersion parameters dictate, but we emphasize that in this linear description, no interaction between the FW and SH occurs.

The effect shown in Sec. 11.2 (and that will be shown later in Sec. 12.3), where the shape of the FW is altered by the SH through the response function, is thus purely a nonlinear effect.

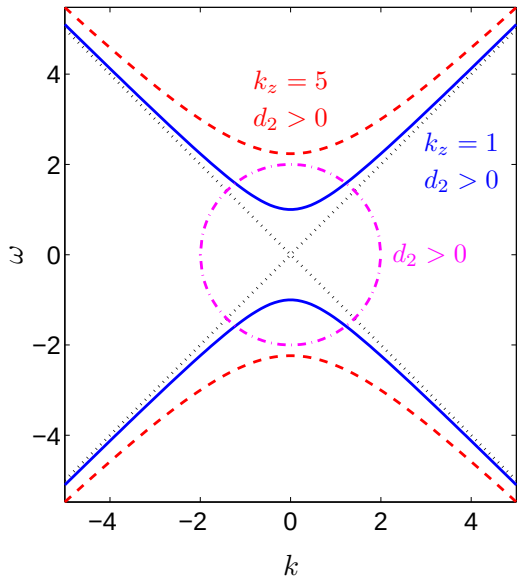

Figure 12.4: *Shape of the linear dispersion relations. We obtain the same circular and hyperbolic shapes as we do for the response functions R_+ and R_-.*

12.2 X-wave case, normal FW and SH dispersion

Here the linear equations for the FW and SH both support X-waves and we know that X-waves in the FW can be generated from a Gaussian input profile [19, 28] . The generation of an X-wave is shown in Fig. 12.5 in the strongly nonlocal regime ($\sigma = 10$). The left (right) column depicts the evolution of the FW (SH) intensity at propagation lengths $z = 0, 2$, and 4. The length scales in question are $L_{\mathrm{D}} = 1.95$ and $L_{\mathrm{NL}} = L_{\mathrm{NL}}^{\mathrm{int}} \approx 0.2$. We see how the input pulse evolves into a clear

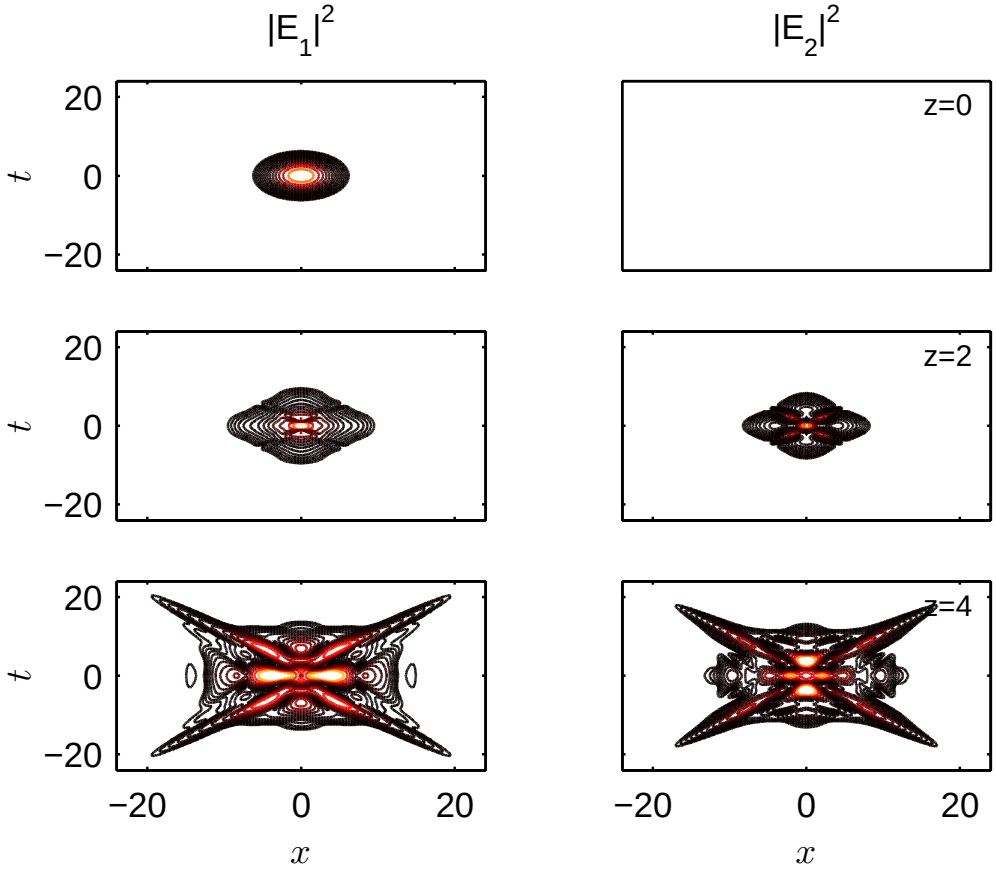

Figure 12.5: *Intensity profile of the strongly nonlocal X-wave case, $\sigma = 10$. The evolution of $|E_1|^2$ (left) and $|E_1|^2$ (right). Parameter values are: $A = 5, B = 3$, and $d_1 = d_2 = -1$. 15 contour lines from 0.005 logarithmically separated to the maximum intensity.*

X-shaped pattern in both the FW and SH fields. Even though $z = 4$ is only about two diffraction lengths it corresponds to about twenty nonlinear lengths, and with a good degree of certainty we say that a stationary two-color X-wave can be obtained in this case. By "two-color" we refer to that the X appears in both the FW and SH. Note that also the spectra evolves into X shapes, see Fig. 12.8.

The effect of decreased nonlocality on X-wave generation is not trivial. Apart from the quadratic dependence on the nonlinearity, γ [from (9.39)], and the consequences on the nonlinear length scales (discussed in Sec. 10.1.2), a smaller degree of nonlinearity increases the dependence on a proper initial condition [38]. This means that formation of X-waves from the initial Gaussian input is significantly slowed down. Due to the periodic boundary conditions inherent in the Fourier split step method applied (see Appendix D), we are not in this case able to evolve the system to the

nonlinear length. We note that this is not a contradiction to the effect that linear equations can *support* X-waves.

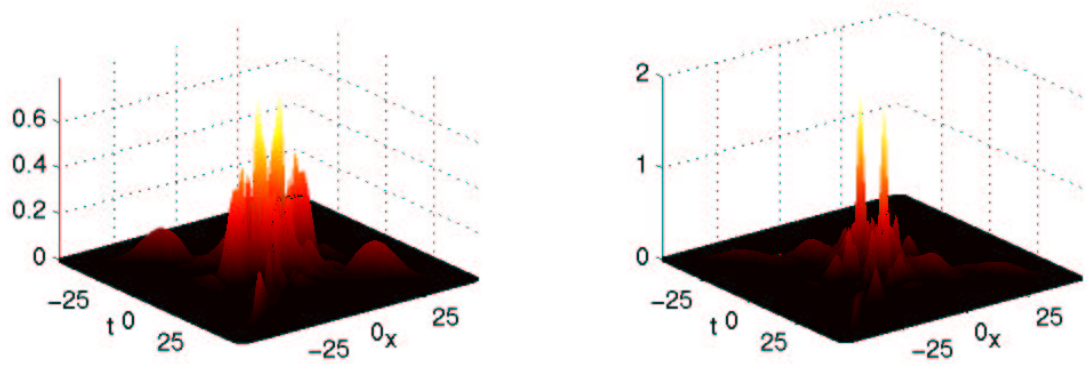

(a) FW intensity,$|E_1|^2$ (b) SH intensity, $|E_2|^2$

Figure 12.6: *The FW and SH profiles,* $|E_1|^2$*, in the strongly nonlocal X wave case,* $\sigma = 10$*,* $d_1 = d_2 = -1$ *at* $z = 8$*. Parameter values are* $A = 5$*,* $B = 3$*.*

Fig. 12.6 shows surface plots of the FW and SH at propagation length $z = 8$, using the $-50 < x, t < 50$ grid with 360×360 grid points as in Fig. 11.12. We note that the magnitude of the SH is roughly equal to that of the FW, except for two peaks of large amplitude.

Fig. 12.7 shows the same plots as Fig. 12.6, but viewed from above and with contour lines.

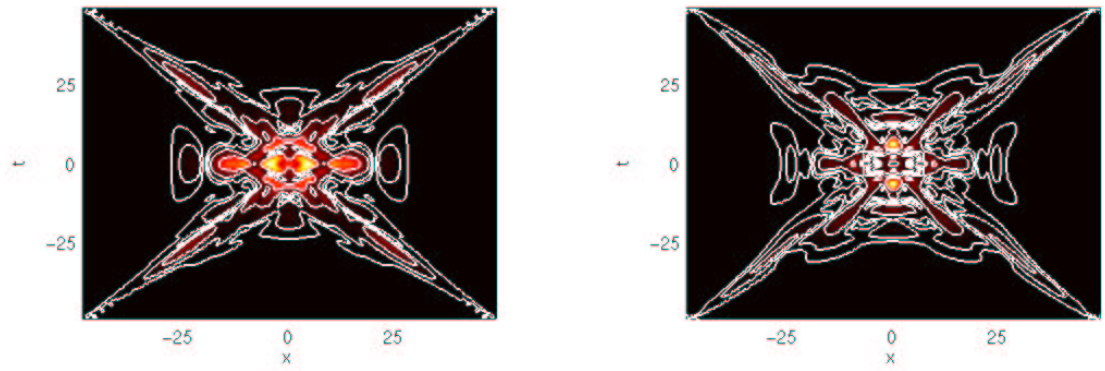

(a) FW intensity,$|E_1|^2$ (b) SH intensity, $|E_2|^2$

Figure 12.7: *The FW and SH profiles in the strongly nonlocal X wave case,* $\sigma = 10$*,* $d_1 = d_2 = -1$ *at* $z = 8$*. Parameter values are* $A = 5$ *and* $B = 3$*. Surface plot viewed from above with a contour plot with 10 logarithmically spaced lines from 0.005 to the maximal intensity.*

12.2.1 Validity of the nonlocal approximation

To investigate the validity of the nonlocal description of X-waves, we use the result of the simulation of the full two-component model (9.29)–(9.30) and obtain $|E_1^2|^2$ and $|E_2|^2$, shown in Fig. 12.5. Our nonlocal theory predicts that we might as well have solved the single component nonlocal equation (9.36) for the fundamental and then found the SH according to the relation (9.34). In other words, the nonlocal model predicts that the FW and SH spectral intensities are linked through the relation $|\widetilde{E_2}|^2 = |\frac{1}{\beta}\ \widetilde{R}\ \widetilde{E_1^2}|^2$.

In Fig. 12.8 we show spectral intensities for the SH, $|\widetilde{E_2}|^2$, at $z = 4$ for $\sigma = 10$, corresponding to the SH at $z = 4$ in Fig. 12.5, and compare it the nonlocal prediction $|\frac{1}{\beta}\ \widetilde{R}\ \widetilde{E_1^2}|^2$. We see that the key features of the X wave are essentially captured, even though the widths differ somewhat. The correspondence might become better after further propagation and evolution towards a stationary state. A cone angle of 90° is expected from both linear and nonlinear theory [38] and confirmed.

We further see that the hyperbola branches of the X obey the nonlocal relation $\omega^2 = \sigma^{-2} + k^2$ and are thus separated by $2\sigma^{-2} = 0.02$ at $k = 0$. It is also seen in Fig. 12.1 for $\sigma = 1$. From standard linear theory and the cascading limit this separation would be equal to twice an undetermined propagation constant, see Sec. 12.1. Our nonlocal model predicts a fixed and predetermined separation of $2\sigma^{-2}$, which our simulations confirm. Correspondingly, the nonlocal model is indeed a reasonable approximation in this strongly nonlocal case with $\sigma = 10$.

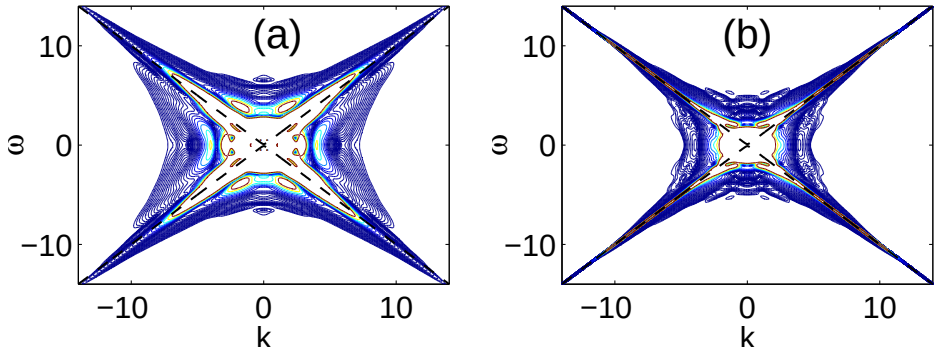

Figure 12.8: *Comparison between* $|\widetilde{E_2}|^2$ *(a) and the nonlocal prediction* $(1/\beta)^2|\widetilde{E_1^2}|^2|\widetilde{R}|^2$ *(b) at* $z = 4$ *with 25 logarithmically spaced contours between 0.0001 and 10. Parameter values are:* $A = 5, B = 3$*, and* $d_1 = d_2 = -1$*.* $\sigma = 10$*,* i.e., *strongly nonlocal. Dashed lines correspond to* $\sigma\omega = \pm\sqrt{1 + \sigma^2 k^2}$*.*

We note that due to the singularities of the response function it is hard to obtain a more precise measure for the validity of the nonlocal model. The contour plots of Fig. 12.8 are a simple way of establishing the validity.

12.3 Modified light bullet case, anomalous FW and normal SH dispersion

In analogy with Sec. 11.2, we denote this case the modified light bullet case, because the linear part of the FW equation supports light bullet generation, not X-waves. In contrast, the X-shaped response function of the nonlocal model for $d_2 = -1$ predicts the whole new possibility of generation of a two-color X-wave, despite the anomalous FW dispersion. We stress that this X-wave in the FW is not predicted by linear theory, nor by the cascading limit. Furthermore, X-wave generation would occur despite the FW being initially Gaussian and the SH being unseeded, thus only through the nonlocal nonlinear attractor, which prevails the FW linear properties.

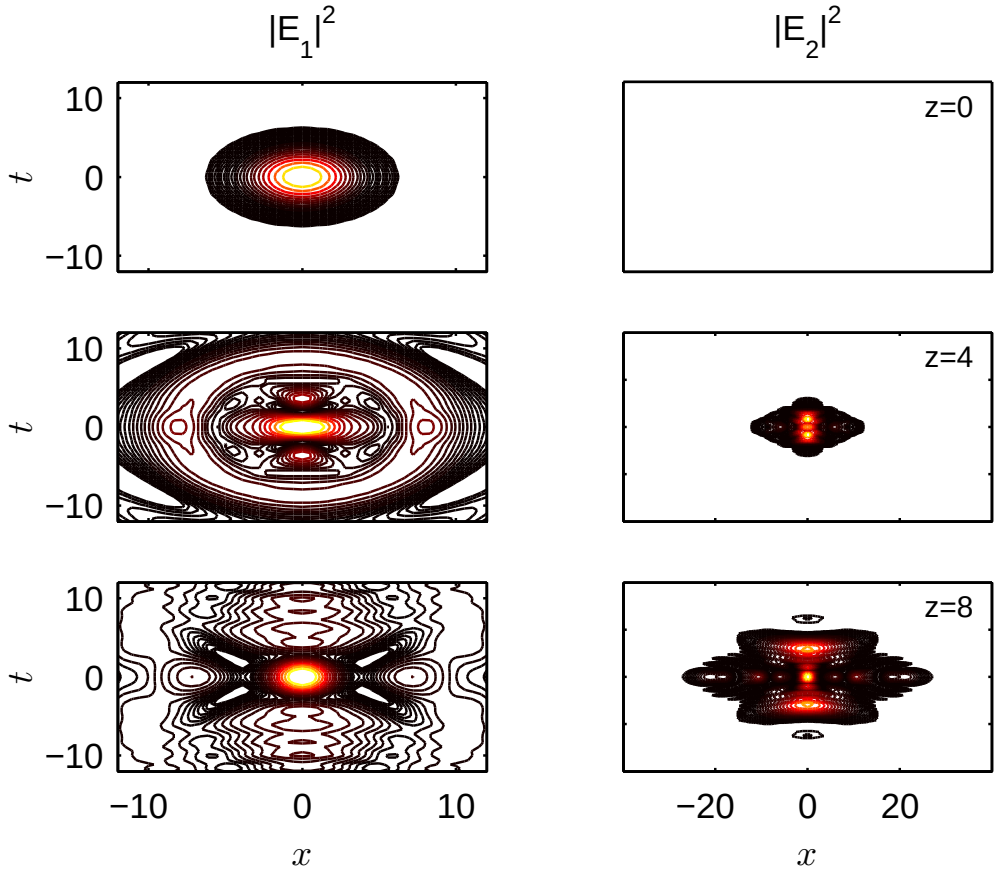

Figure 12.9: *FW and SH intensity profiles* $|E_1|^2$ *(left) and* $|E_2|^2$ *(right) at propagation lengths* $z = 0, 4,$ *and* 8. *Parameter values are:* $A = 5, B = 3,$ *and* $d_1 = -d_2 = 1$. *Strongly nonlocal case,* $\sigma = 10$. *25 contour lines from 0.005 logarithmically separated to the maximum intensity. The mesh size is* 360 *on a* $-50 < x, t < 50$ *domain.*

We consider again the strongly nonlocal case with $\sigma = 10$. In Fig. 12.9 we show the results of a simulation of the full model out to $z = 8$, corresponding to about 4 diffraction lengths and 40 nonlinear lengths. We have used a larger computational box ($-50 < x, t < 50$) in order to be able to simulate for longer distances, because the generation of a X-wave requires the built up of the unseeded SH and is thus expected to be slow. We use 360×360 discretization points to maintain a reasonable resolution. From the figure we see a lot of radiation in the FW during the built up of the SH which at $z = 8$ has grown sufficiently strong to indeed generate an X-shape in the FW

despite its dispersion being anomalous.

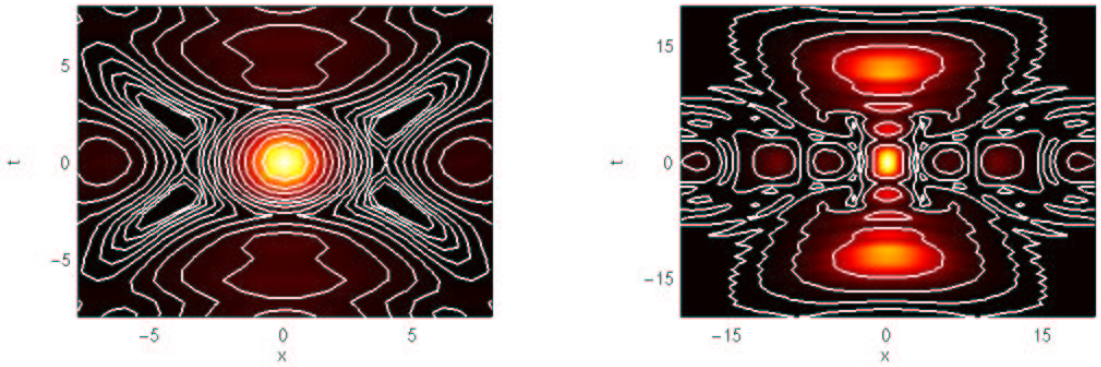

(a) FW intensity,$|E_1|^2$ (b) SH intensity, $|E_2|^2$

Figure 12.10: *The FW and SH profiles in the strongly nonlocal X wave case, $\sigma = 10$, $d_1 = d_2 = -1$ at $z = 8$. Parameter values are $A = 5$ and $B = 3$. Surface plot viewed from above with a contour plot with 10 logarithmically spaced lines from 0.005 to the maximal intensity.*

Compared to the right column plots in Figs. 12.6–12.7 (showing the SH profile of the "full" X-wave case), the SH X-shape in Figs. 12.9–12.10 more resembles the shape of an hourglass more than the SH in the case $d_1 = d_2 = -1$. We note that this corresponds to convolution with the response function, $R_-(x,t)$ (Fig. 12.2), which is different from zero in a similar region. Furthermore, just as the shape of the SH affects the FW, the shape of the FW affects the SH, was was also seen in Sec. 11.2. In Secs. 11.1 and 12.2, the shapes of the linear dispersion relations are the same for both the FW and the SH (see Sec. 12.1), so no competing is noted due to the nonlocality.

13 Conclusion

We have developed a nonlocal description of 2+1 dimensional spatio-temporal waves in quadratic nonlinear materials. The model predicts that the interaction between the FW and SH is described by a response function which takes into account the linear properties of the SH. The nonlocal model is therefore more accurate than the cascading limit NLS equation, which neglects all linear properties of the SH and assumes that the SH is simply slaved to the FW.

Depending on the linear properties of the SH, the response function can take on 3 fundamentally different shapes, characterized by having singularities either in origo, along hyperbolas, or along circles in the spectral domain. In this work we have limited ourselves to a positive phase mismatch, which excludes the type of response function with a circular singularity.

With a positive phase mismatch and anomalous SH dispersion the response function of the nonlocal model has nice physical properties: it is normalizable and it has both a simple local (cascading) and strongly nonlocal linear limit. We therefore denote the localized wave solutions of this case as *accessible nonlocal solitons*.

In contrast, for normal SH dispersion, we have shown that the response function is not normalizable and that it neither has a cascading, nor a strongly nonlocal linear limit. We therefore denote the localized wave solutions of this case as *inaccessible nonlocal solitons*. Our nonlocal model predicts the general tendency of X-waves to form in this case, even for anomalous FW dispersion; an effect that is never predicted by the cascading limit, which only predicts light bullets.

We have calculated the linear and nonlinear length scales and shown how they vary with the degree of nonlocality. We have shown the existence of two nonlinear lengths defined from the nonlinear phase and intensity variations, respectively. For a small degree of nonlocality the phase change determines the nonlinear length and for strong nonlocality the intensity variation determines the nonlinear length. A threshold between the two regimes has been found.

We have conducted numerical simulations with an unseeded SH and a Gaussian FW input. The simulations show that the nonlocal model provides a reasonable description of the dynamics in a broad range of parameter values.

We have shown that accessible nonlocal X-waves can be generated for normal FW dispersion and anomalous SH dispersion. For normal SH dispersion we have shown that inaccessible nonlocal X-waves can be generated both for normal (conventional X-waves) and for anomalous FW dispersion.

The generation of two-color X waves in quadratic nonlinear materials with anomalous dispersion either in the FW or SH has never been observed before. The inaccessible nonlocal X-wave found here for the first time with anomalous FW dispersion is neither predicted by linear theory nor by the cascading limit. However, both these novel types of X-waves arise naturally in the framework of the nonlocal model.

A nonlocal epilogue

By using a nonlocal model of dipole-dipole interaction in the modeling of biomolecules, we were able to introduce geometrical features — curvature and twist — in the description of the DNA molecule. These were shown to generate localization of energy, a feature which is also generated by the introduction of inhomogeneities, but the applied model is intrinsically homogeneous.

Energy localization is important in connection with the opening of the DNA molecule. The opening is crucial for protein synthesis and cell reproduction and thus for life itself and the understanding of the underlying prosesses is important for e.g., future drug design.

There are several ways to improve our model. First of all, our model DNA chain is *rigid* and it therefore has no way of adjusting to the changes made by the dynamics. One idea — which has already been touched upon [66] — is to use a semi-flexible chain, that is, a chain that dynamically changes its geometry based on lowest energy state. Our model only describes a precursor of DNA denaturation as thus features no description of how the DNa molecule *closes* itself after denaturation. This is referred to as the *zipping/unzipping*-phenomenon and it would be a tremendous achievement to implement this in a mathematical model.

New experiments with DNA molecules are always interesting, both to validate the model predictions, but also to improve parameter accuracy. In the longer perspective even tertiary structures may be included and this would probably necessitate a three dimensional description of the molecule.

We have also studied a localized optical quantity — the X-wave — in quadratically nonlinear materials. The X-wave has been observed only in materials with normal diffusion. By using a nonlocal description we were able to predict the existence of X-shaped waves in materials also with anomalous diffusion, this being diffusion in either the fundamental wave, the second harmonic field, or both.

Localized optical structures are important candidates as carriers of information in future all-optical signal processing circuits - and already today as carriers on information in optical fibers.

The nonlocal description of quadratically optical materials in this Thesis suffers somewhat from not being able to clearly separate the effect of the nonlocality from the nonlinearity, as the latter is the square of the former. When investigating the nonlocality, this is not ideal, so one might benefit from the investigation of other physical systems. For the $\chi^{(2)}$-materials, however, the case of negative phase mismatch is an obvious extension to the present work. Ongoing work is simulating the nonlocal equations to begin with, rather than comparing the simulation outcome with an analytic result.

Experimental observation of X-waves in a medium with anomalous dispersion is another obvious goal.

It is worth noting the similarities between the modeling of two physical systems as far from each other, as biomolecular dynamics and light propagation in optical crystals might seem.

One important difference is that the natural setting for protein dynamics is a discrete model, and the augmented Peyrard-Bishop we investigate is no exception to this. Conversely, optical crystals are better described using continuous models. Nevertheles, both cases have used initial conditions with Gaussian profiles. This proves the diversity of this pulse, but it also suggests the generality of the models considered. Both models support the existence of localized structures.

Furthermore, both models reduce to a version of the Nonlinear Schrödinger Equation, underlining its already huge importance in nonlinear science.

Thirdly — and most importantly in the context of this Thesis — we have shown that in both cases the notion of nonlocality reveals new insight and a more accurate description of the dynamics.

Just as the focus shifted from linear to nonlinear models a number of years ago, it seems probable that nonlocal models will expand to other areas of research in the future.

Bibliography

[1] F. Wise and P. Di Trapani. Spatiotemporal solitons - the hunt for light bullets. *Opt. Photonics News*, 13(2):28, February 2002.

[2] Paul Michael Petersen and Torben Skettrup. *Ulineær Optik (In Danish)*. Polyteknisk Forlag, Lyngby, Denmark, 1994.

[3] Alexander V. Buryak, Paolo Di Trapani, Dmitry V. Skryabin, and Stefano Trillo. Optical solitons due to quadratic nonlinearities: from basic physics to futuristic applications. *Physics Reports*, 370(2):63–235, July 2002.

[4] G. Assanto and G.I. Stegeman. Simple physics of quadratic spatial solitons. *Opt. Express*, 10(9):388–396, May 2002.

[5] William E. Torruellas, Zuo Wang, David J. Hagan, Eric W. VanStryland, George I. Stegeman, Lluís Torner, and Curtis R. Menyuk. Observation of two-dimensional spatial solitary waves in a quadratic medium. *Physical Review Letters*, 74(25):5036–5039, June 1995.

[6] William E. Torruellas, Zuo Wang, Lluis Torner, and George I. Stegeman. Observation of mutual trapping and dragging of two-dimensional spatial solitary waves in a quadratic medium. *Optics Letters*, 20(19):1949–1951, October 1995.

[7] Roland Schiek, Yongsoon Baek, and George I. Stegeman. One-dimensional spatial solitary waves due to cascaded second-order nonlinearities in planar waveguides. *Physical Review E*, 53(1):1138–1141, January 1996.

[8] P. Di Trapani, D. Caironi, G. Valiulis, A. Dubietis, Danielius, and A. Piskarskas. Observation of temporal solitons in second-harmonic generation with tilted pulses. *Physical Review Letters*, 81(3):570–573, July 1998.

[9] Yu.N. Karamzin and A.P. Sukhorukov. Nonlinear interaction of diffracting beams of light in a medium of quadratic nonlinearity, mutual focusing of beams and restriction of optical frequency convertor efficiency. *Zhurnal Eksperimental'noi i Teoreticheskoi Fiziki, Pis'ma v Redaktsiyu*, 20(11):734–9, 1974.

[10] Yu.N. Karamzin and A.P. Sukhorukov. On mutual focusing of intense light beams in media with quadratic nonlinearity. *Zhurnal Eksperimental'noi i Teoreticheskoi Fiziki*, 68(3):834–47, 1975.

[11] Lluis Torner, Curtis R. Menyuk, and George I. Stegeman. Excitation of solitons with cascaded $\chi^{(2)}$ nonlinearities. *Optics Letters*, 19(20):1615–1617, October 1994.

[12] Lluis Torner, Curtis R. Menyuk, William E. Torruellas, and George I. Stegeman. Two-dimensional solitons with second-order nonlinearities. *Optics Letters*, 20(1):13–15, January 1995.

[13] L. Torner, C. R. Menyuk, and G. I. Stegeman. Bright solitons with second-order nonlinearities. *Journal of the Optical Society of America B*, 12(5):889–897, 1995.

[14] Alexander V. Buryak and Yuri S. Kivshar. Spatial optical solitons governed by quadratic nonlinearity. *Optics Letters*, 19(20):1612–1614, October 1994.

[15] Lluis Torner. Stationary solitary waves with second-order nonlinearities. *Optics Communications*, 114(1-2):136–140, 1995.

[16] Alexander V. Buryak and Yuri S. Kivshar. Solitons due to second harmonic generation. *Physics Letters A*, 197(5-6):407–412, February 1995.

[17] L. Bergé, V.K. Mezentsev, J.J. Rasmussen, and J. Wyller. Formation of stable solitons in quadratic nonlinear media. *Physical Review A*, 52(1):R28–R31, July 1995.

[18] Stationary trapping of light beams in bulk second-order nonlinear media. L. torner and d. mihalache and d. mazilu and e. m. wright and w. e. torruellas and g. i. stegeman. *Optics Communications*, 121(4-6):149–155, 1995.

[19] P. Di Trapani, G. Valiulis, A. Piskarskas, O. Jedrkiewicz, J. Trull, C. Conti, and S. Trillo. Spontaneously generated x-shaped light bullets. *Physical Review Letters*, 91:093904, August 2004.

[20] X. Liu, L. J. Qian, and F. W. Wise. Generation of optical spatiotemporal solitons. *Physical Review Letters*, 82(23):4631–4634, June 1999.

[21] H. S. Heisenberg, R. Morandotti, Y. Silberberg, S. Bar-Ad, D. Ross, and J. S. Aitchison. Kerr spatiotemporal self-focusing in a planar glass waveguide. *Physical Review Letters*, 87(4):043902, July 2001.

[22] D. E. Edmundson and R. H. Enns. Robust bistable light bullets. *Optics Letters*, 17(8):586–588, April 1992.

[23] R. H. Enns and D. E. Edmundson. Guide to fabricating bistable-soliton-supporting media. *Physical Review A*, 47(5):4524–4527, May 1993.

[24] D. E. Edmundson and R. H. Enns. Particlelike nature of colliding three-dimensional optical solitons. *Physical Review A*, 51(3):2491–2498, March 1995.

[25] J. K. Ranka, R. W. Schirmer, and A. L. Gaeta. Observation of pulse splitting in nonlinear dispersive media. *Physical Review Letters*, 77(18):3783–3786, October 1996.

[26] A. A. Zozulya, S. A. Diddams, A. G. Van Engen, and T. S. Clement. Propagation dynamics of intense femtosecond pulses: Multiple splittings, coalescence, and continuum generation. *Physical Review Letters*, 82(7):1430–1433, February 1999.

[27] J. Lu and J. F. Greenleaf. Experimental verification of nondiffracting x waves. *IEEE Trans. Ultrason. Ferroelectr. Freq. Control*, 39(3):441–446, May 1992.

[28] C. Conti, S. Trillo, P. Di Trapani, G.Valiulis, A. Piskarskas, O. Jedrkiewicz, and J. Trull. Nonlinear electromagnetic x waves. *Physical Review Letters*, 90:170406, May 2003.

[29] D. Mugnai, A. Ranfagni, and R. Ruggeri. Observation of superluminal behaviors in wave propagation. *Physical Review Letters*, 84(21):4830–4833, May 2000.

[30] H. Sõnajalg, M. Rätsep, and P. Saari. Demonstration of the bessel-x pulse propagating with strong lateral and longitudinal localization in a dispersive medium. *Optics Letters*, 22(5):310–312, March 1997.

[31] P. Saari and K. Reivelt. Evidence of x-shaped propagation-invariant localized light waves. *Physical Review Letters*, 79(21):4135–4138, November 1997.

[32] J. Durnin, Jr. J. J. Miceli, and J. H. Eberly. Diffraction-free beams. *Physical Review Letters*, 58(15):1499–1501, April 1987.

[33] M. A. Porras, S. Trillo, C. Conti, and P. Di Trapani. Paraxial envelope x waves. *Optics Letters*, 28(13):1090–1092, July 2003.

[34] Miguel A. Porras and Paolo Di Trapani. Localized and stationary light wave modes in dispersive media. *Physical Review E*, 69(6):066606–1–066606–10, 2004.

[35] O. Jedrkiewicz, J. Trull, G. Valiulis, A. Piskarskas, C. Conti, S. Trillo, and P. Di Trapani. Nonlinear x waves in second-harmonic generation: Experimental results. *Physical Review E*, 68:026610, August 2003.

[36] M. Kolesik, E.M. Wright, and J.V. Moloney. Dynamic nonlinear x waves for femtosecond pulse propagation in water. *Physical Review Letters*, 92(25):253901–1–253901–4, 2004.

[37] Audrius Dubietis, Eugenijus Gaizauskas, Gintaras Tamosauskas, and Paolo Di Trapani. Light filaments without self-channeling. *Physical Review Letters*, 92(25):253903–1–253903–4, 2004.

[38] Claudio Conti. Generation and nonlinear dynamics of x waves of the schrödinger equation. *Physical Review E*, 70:046613, October 2004.

[39] Sotiris Droulias, Kyriakos Hizanidis, Joachim Meier, and Demetrios N. Christodoulides. X - waves in nonlinear normally dispersive waveguide arrays. *Optics Express*, 13(6):1827–1832, 2005.

[40] L. Khaykovich, F. Schreck, G. Ferrari, T. Bourdel, J. Cubizolles, L. D. Carr, Y. Castin, and C. Salomon. Formation of a matter-wave bright soliton. *Science*, 296:1290–1293, May 2002.

[41] K. E. Strecker, G. B. Partridge, A. G. Truscott, and R. G. Hulet. Formation and propagation of matter-wave soliton trains. *Nature*, 417:150–153, May 2002.

[42] Claudio Conti and Stefano Trillo. Nonspreading wave packets in three dimensions formed by an ultracold bose gas in an optical lattice. *Physical Review Letters*, 92:120404, March 2004.

[43] N. I. Nikolov, D. Neshev, O. Bang, and W. Z. Królikowski. Quadratic solitons as nonlocal solitons. *Physical Review E*, 68:036614, September 2003.

[44] I. V. Shadrivov and A. A. Zharov. Dynamics of optical spatial solitons near the interface between two quadratically nonlinear media. *Journal of the Optical Society of America B*, 19(3):596–602, 2002.

[45] Claudio Conti, Marco Peccianti, and Gaetano Assanto. Route to nonlocality and observation of accessible solitons. *Physical Review Letters*, 91:073901, June 2003.

[46] W. Krolikowski, O. Bang, N. I. Nikolov, D. Neshev, J. Wyller, J. J. Rasmussen, and D Edmundson. Modulational instability, solitons and beam propagation in spatially nonlocal nonlinear media. *Journal of Optics B: Quantum and Semiclassical Optics*, 6(5):S288–S294, May 2004.

[47] W. Krolikowski, O. Bang, J. Wyller, and J. J. Rasmussen. Optical beams in nonlocal nonlinear media. *Acta Physica Polonica - Series A General Physics*, 103(2-3):133–148, 2003.

[48] Demetrios N. Christodoulides, Nikolaos K. Efremidis, Paolo Di Trapani, and Boris A. Malomed. Bessel x waves in two- and three-dimensional bidispersive optical systems. *Optics Letters*, 29(13):1446–1448, 2004.

[49] Alessandro Ciattoni and Paolo Di Porto. One-dimensional nondiffracting pulses. *Physical Review E*, 69(5):056611–1–056611–6, 2004.

[50] C. R. Menyuk, R. Schiek, and L. Torner. Solitary waves due to x(2):x(2) cascading. *Journal of the Optical Society of America B*, 11(12):2434, December 1994.

[51] Ole Bang. Dynamical equations for wave packets in materials with both quadratic and cubic response. *Journal of the Optical Society of America B*, 14(1):51–61, January 1997.

[52] Sumiyoshi Abe and Akihiro Ogura. Solitary waves and their critical behavior in a nonlinear nonlocal medium with power-law response. *Physical Review E*, 57(5):6066–6070, May 1998.

[53] O. Bang and W. Z. Królikowski. Solitons in nonlocal nonlinear media: Exact solutions. *Physical Review E*, 63(1):016610, January 2000.

[54] D. J. Mitchell and A. W. Snyder. Soliton dynamics in a nonlocal medium. *Journal of the Optical Society of America B*, 16(2):236–239, 1999.

[55] P. Chernev and V. Petrov. Self-focusing of light pulses in the presence of normal group-velocity dispersion. *Optics Letters*, 17(3):172–174, 1992.

[56] John Wyller, Wieslaw Krolikowski, Ole Bang, and Jens Juul Rasmussen. Generic features of modulational instability in nonlocal kerr media. *Physical Review E - Statistical Physics, Plasmas, Fluids, and Related Interdisciplinary Topics*, 66(6):066615/1–066615/13, 2002.

[57] I.S. Gradshteyn and I.M. Ryzhik. *Table of Integrals, Series, and Products*. Academic, 1980.

[58] P. V. Larsen, O. Bang, M. P. Sørensen, W. Z. Krolikowki, and S. Trillo. Nonlocal description of x-waves in quadratic nonlinear materials. *submitted to Phys. Rev. E*, 2005. nlin.PS/0512XX.

[59] Yu.S. Kivshar and D.E. Pelinovsky. Self-focusing and transverse instabilities of solitary waves. *Physics Reports*, 331(4):117–195, June 2000.

[60] L. Bergé, O. Bang, J.J. Rasmussen, and V.K. Mezentsev. Self-focusing and solitonlike structures in materials with competing quadratic and cubic nonlinearities. *Physical Review E*, 55(3):3555–3570, March 1997.

[61] A. W. Snyder and D. J. Mitchell. Accessible solitons. *Science*, 276(5318):1538–1541, 1997.

[62] Govind P. Agrawal. *Nonlinear Fiber Optics*. Academic Press, San Diego, California, 2001.

[63] A. Kobyakov, F. Lederer, O. Bang, and Y.S. Kivshar. Nonlinear phase shift and all-optical switching in quasi-phase-matched quadratic media. *Optics Letters*, 23(7):506–8, 1998.

[64] D. E. Edmundson and R. H. Enns. Fully three-dimensional collisions of bistable light bullets. *Optics Letters*, 18(19):1609–1611, October 1993.

[65] Stefano Longhi. Parametric amplification of spatiotemporal localized envelope waves. *Physical Review E*, 69:016606, 2004.

[66] S. F. Mingaleev, Yu. B. Gaididei, P. L. Christiansen, and Yu. S. Kivshar. Nonlinearity-induced conformational instability and dynamics of biopolymers. *Europhysics Letters*, 59(3):403–409, 2002.

[67] Peter Vingaard Larsen. Energy funnelling in a DNA model. Master's thesis, Technical University of Denmark, 2002. IMM-THESIS-2002-32.

[68] Serge F. Mingaleev, Yuri B. Gaididei, and Franz G. Mertens. Solitons in anharmonic chains with power-law long-range interactions. *Physical Review E*, 58(3):3833–3842, September 1998.

[69] Alan C. Newell and Jerome V. Moloney. *Nonlinear Optics*. Addison-Wesley, Redwood City, CA, 1992.

A
Derivation of the equations of motion

To derive the equations of motions we first write some elements of the Hamiltonian to get a better grasp of the terms involved. From Equation (2.10) we get

$$
\begin{aligned}
H &= \mathcal{H}_n \\
&= \frac{1}{2}\dot{u}_{-N}^2 + \frac{C}{4}\left(u_{-N+1}-u_1\right)^2 + \left(e^{-\alpha u_{-N}}-1\right)^2 - \frac{1}{2}\sum_{m=-N+1}^{N} J_{-N,m}u_{-N}u_m \\
&\quad + \frac{1}{2}\dot{u}_2^2 + \frac{C}{4}\left(u_{-N+2}-u_2\right)^2 + \frac{C}{4}\left(u_{-N+1}-u_1\right)^2 + \left(e^{-\alpha u_{-N+1}}-1\right)^2 \\
&\qquad\qquad - \frac{1}{2}\sum_{m\neq -N+1}^{N} J_{-N+1,m}u_{-N+1}u_m \\
&\quad + \qquad\qquad\qquad\qquad \vdots \\
&\quad + \frac{1}{2}\dot{u}_{n-1}^2 + \frac{C}{4}\left(u_n-u_{n-1}\right)^2 + \frac{C}{4}\left(u_{n-1}-u_{n-2}\right)^2 + \left(e^{-\alpha u_{n-1}}-1\right)^2 - \frac{1}{2}\sum_{m\neq n}^{n} J_{n-1,m}u_{n-1}u_m \\
&\quad + \frac{1}{2}\dot{u}_n^2 + \frac{C}{4}\left(u_{n+1}-u_n\right)^2 + \frac{C}{4}\left(u_n-u_{n-1}\right)^2 + \left(e^{-\alpha u_n}-1\right)^2 - \frac{1}{2}\sum_{m\neq n}^{n} J_{nm}u_n u_m \\
&\quad + \frac{1}{2}\dot{u}_{n+1}^2 + \frac{C}{4}\left(u_{n+2}-u_{n+1}\right)^2 + \frac{C}{4}\left(u_{n+1}-u_n\right)^2 + \left(e^{-\alpha u_{n+1}}-1\right)^2 - \frac{1}{2}\sum_{m\neq n}^{n} J_{n+1,m}u_{n+1}u_m \\
&\quad + \qquad\qquad\qquad\qquad \vdots \\
&\quad + \frac{1}{2}\dot{u}_{N-1}^2 + \frac{C}{4}\left(u_N-u_{N-1}\right)^2 + \frac{C}{4}\left(u_{N-1}-u_{N-2}\right)^2 + \left(e^{-\alpha u_{N-1}}-1\right)^2 - \frac{1}{2}\sum_{m\neq N-1}^{N} J_{N-1,m}u_{N-1}u_m \\
&\quad + \frac{1}{2}\dot{u}_N^2 + \frac{C}{4}\left(u_N-u_{N-1}\right)^2 + \left(e^{-\alpha u_N}-1\right)^2 - \frac{1}{2}\sum_{m=1}^{N-1} J_{Nm}u_N u_m.
\end{aligned}
\tag{A.1}
$$

Differentiation of the Hamiltonian (A.1) is now a bit tricky due to this splitting. However, by introducing $p_n = \dot{u}_n$ and $q_n = u_n$, we get (easily):

$$\frac{\partial H}{\partial p_n} = p_n, \qquad n \in [-N, N] \tag{A.2}$$

In the general case, we get, although not quite as easy:

$$\begin{aligned} \frac{\partial H}{\partial q_n} &= \overbrace{\frac{C}{2}\big(u_n - u_{n-1}\big)}^{\bullet 1} + \overbrace{\frac{C}{2}\big(- (u_{n+1} - u_n) + u_n - u_{n-1}\big)}^{\bullet 2} \\ &\quad \underbrace{-\frac{C}{2}\big(u_{n+1} - u_n\big)}_{\bullet 3} - 2e^{-u_n}\left(e^{-u_n} - 1\right) \\ &\quad \underbrace{-\frac{1}{2}\sum_{m\neq n} J_{nm}u_m}_{\bullet 4} \underbrace{-\frac{1}{2}\sum_{m\neq n} J_{nm}u_m}_{\bullet 5}, \qquad n \in [-N+1, N-1], \end{aligned} \tag{A.3}$$

where the first term $\bullet 1$ in the C-parenthesis stems from equation from the previous value of n and $\bullet 3$ from the next. $\bullet 2$ and $\bullet 4$ are from the nth equation, whereas the last summation $\bullet 5$ is a collection of contributions from all the other values of n.

Obtained in the same way, but more accessible is the equations for $n = -N$:

$$\begin{aligned} \frac{\partial H}{\partial q_1} &= -\frac{C}{2}\left(u_{-N+1} - u_1\right) - \frac{C}{2}\left(u_{-N+1} - u_1\right) - 2e^{-u_{-N}}\left(e^{-u_{-N}} - 1\right) \\ &\quad -\frac{1}{2}\sum_{m=-N+1}^{N} J_{-N,m}u_m - \frac{1}{2}\sum_{m\neq -N} J_{-N,m}u_m, \qquad n = -N \end{aligned} \tag{A.4}$$

and $n = N$:

$$\begin{aligned} \frac{\partial H}{\partial q_N} &= \frac{C}{2}\left(u_N - u_{N-1}\right) + \frac{C}{2}\left(u_N - u_{N-1}\right) - 2e^{-u_N}\left(e^{-u_N} - 1\right) \\ &\quad -\frac{1}{2}\sum_{m=1}^{N-1} J_{Nm}u_m - \frac{1}{2}\sum_{m\neq N} J_{Nm}u_m, \qquad n = N, \end{aligned} \tag{A.5}$$

where the summation terms have been added to one.

Collecting terms in (A.3)-(A.5) and inserting, the Hamilton equation:

$$\frac{\partial H}{\partial p_n}\dot{p}_n + \frac{\partial H}{\partial q_n}\dot{q}_n = 0 \tag{A.6}$$

gives us the equations of motion for 3 different cases:

$n = -N$

$$\ddot{u}_{-N} - C\left(u_{-N+1} - u_{-N}\right) - 2e^{-u_{-N}}\left(e^{-u_{-N}} - 1\right) - \sum_{m \neq -N} J_{-N,m}u_m = 0 \tag{A.7}$$

$n \in [-N+1, N-1]$

$$\ddot{u}_n - C\left(u_{n-1} + u_{n+1} - 2u_n\right) - 2e^{-u_n}\left(e^{-u_n} - 1\right) - \sum_{m \neq n} J_{nm}u_m = 0 \tag{A.8}$$

$n = N$

$$\ddot{u}_N + C\left(u_N - u_{N-1}\right) - 2e^{-u_N}\left(e^{-u_N} - 1\right) - \sum_{m \neq N} J_{Nm}u_m = 0 \tag{A.9}$$

B
Multiple Scale Expansion

This Appendix is basically from [67].

Long range interaction

For the present we look at a dipole-dipole interaction on a straight chain with parallel dipoles, which has the following algebraic form

$$J_{nm} = \frac{J_0}{|\mathbf{r}_n - \mathbf{r}_m|^3} \equiv \frac{J_0}{d^3 \cdot |n-m|^3}, \tag{B.1}$$

where $\mathbf{r}_n$ is the distance to the nth base pair and where the last equality holds in the case of a straight chain, *i.e.,* d is used here as the lattice constant (instead of l). We now use Taylor expansions of the u_m-terms. In general, a Taylor expansion can be written in a differential operator form as follows:

$$\begin{aligned} u(x+\Delta x) &= u(x) + \Delta x\ \partial_x u(x) + \ldots + \frac{1}{n!}\Delta x^n\ \partial_x^n u(x) + \ldots \\ &= \left(1 + \Delta x\ \partial_x + \ldots + \frac{1}{n!}\Delta x^n\ \partial_x^n + \ldots\right) u(x) \\ &= e^{\Delta x\, \partial_x} u(x), \end{aligned}$$

recognizing the series expression for the exponential function. Using this, writing u_m as $u_m \equiv u_{n+(m-n)}$ and expanding around m (so $m-n$ can be compared to the Δx above) allow us express the dipole-dipole long range interaction term as

$$\sum_{m\neq n} J_{nm} u_m = \frac{J_0}{d^3} \sum_{m\neq n} \frac{e^{(m-n)\partial_n}}{|n-m|^3} u_n = \frac{J_0}{d^3} P\left(\partial_n\right) u_n, \tag{B.2}$$

Introducing $k \equiv m-n$ we get for the $P\left(\partial_n\right)$-function:

$$\begin{aligned} P\left(\partial_n\right) &= \sum_{k\neq 0} \frac{e^{k\partial_n}}{|k|^3} = \sum_{k=1}^{\infty} \frac{e^{k\partial_n} + e^{-k\partial_n}}{k^3} \\ &= 2\sum_{k=1}^{\infty} \frac{\cosh(k\partial_n)}{k^3} = 2\sum_{k=1}^{\infty} \frac{1}{k^3} - Q(3,\partial_n), \end{aligned} \tag{B.3}$$

with

$$Q(3,\partial_n) = 2\sum_{k=1}^{\infty} \frac{1-\cosh(k\partial_n)}{k^3}$$

as in [68]. In this paper it is justified that

$$Q(3,ik) \approx -k^2 \ln|k| + \frac{3}{2}k^2 + \frac{1}{144}k^4 \tag{B.4}$$

and by letting $k = -i\partial_n$ and only taking into account terms proportional to k^2 we get $Q(3,\partial_n) \approx -\frac{3}{2}\partial_n^2$. This is a rather crude approximation to exclude the logarithmic term, but note that the value of k cannot be smaller than 1. Thus we avoid the singularity for the logarithmic function at $k = 0$ and we are on a bit more solid ground.

Furthermore, the solution of the first part of (B.3) is twice the Riemann ζ-function $\zeta(s) = \sum_{k=1}^{\infty} \frac{1}{k^s}$, with the value $\zeta(3) = 1.20206$. Finally, we end up with the following approximation to the LRI-term (from (B.2)):

$$\sum_{m\neq n} J_{nm}u_m \approx \frac{J_0}{d^3}\left(2\zeta(3) + \frac{3}{2}\partial_n^2\right)u_n \tag{B.5}$$

Perturbation approach

By the continuum limit approximation, we transform the discrete problem to a continuous one [so that $u_n \mapsto u(x)$] and consider for simplicity an infinite chain. The exponential terms can be expanded in terms of a Taylor series and so $2\left(e^{-u}-1\right)e^{-u}$ to the order u^4 becomes $-2u + 3u^2 - \frac{7}{3}u^3 + \mathcal{O}\left(u^4\right)$. The discrete differential operator, ∂_n^2 in (B.5), becomes $d^2\partial_x^2$. Furthermore, using finite difference approximations to identify the second order spatial derivative (with $x = d{\cdot}n$) the equations of motion (2.11) for the infinite chain become:

$$\frac{\partial^2 u}{\partial t^2} - cd^2\frac{\partial^2 u}{\partial x^2} + 2u - 3u^2 + \frac{7}{3}u^3 - \frac{2J_0\zeta(3)}{d^3}u - \frac{3}{2}\frac{J_0}{d}\frac{\partial^2 u}{\partial x^2} = 0 \tag{B.6}$$

By introducing the constants $\alpha = d^2\left(c + \frac{3}{2}\frac{J_0}{d^3}\right)$ and $\beta = 2\left(1 - \frac{J_0}{d^3}\zeta(3)\right)$ we get the following equation of motion:

$$\frac{\partial^2 u}{\partial t^2} - \alpha\frac{\partial^2 u}{\partial x^2} + \beta u - 3u^2 + \frac{7}{3}u^3 = 0 \tag{B.7}$$

We now apply mulitple scale expansion techniques on the equation (B.7). First of all, we assume small oscillations, so we have the perturbations:

$$\begin{aligned} u &= \varepsilon u^{(1)} + \varepsilon^2 u^{(2)} + \varepsilon^3 u^{(3)} + \mathcal{O}(\varepsilon^4) \\ t &= t_0 + \varepsilon t_1 + \varepsilon^2 t_2 + \mathcal{O}(\varepsilon^3) \\ x &= x_0 + \varepsilon x_1 + \varepsilon^2 x_2 + \mathcal{O}(\varepsilon^3) \end{aligned}$$

Note the difference in the notation for the perturbed *function* u and the perturbed *variables* x and t. This makes notation more convenient in future differentiations.
Differentiation with respect to the perturbed variables are of the form

$$\frac{\partial}{\partial t} = \frac{\partial}{\partial t_0} + \varepsilon\frac{\partial}{\partial t_1} + \varepsilon^2\frac{\partial}{\partial t_2} + \mathcal{O}(\varepsilon^3) \tag{B.8}$$

and the double derivatives of the form

$$\frac{\partial^2}{\partial t^2} = \frac{\partial^2}{\partial t_0^2} + 2\varepsilon \frac{\partial^2}{\partial t_0 \partial t_1} + \varepsilon^2 \left(\frac{\partial^2}{\partial t_1^2} + 2\frac{\partial^2}{\partial t_0 \partial t_2} \right) + \mathcal{O}(\varepsilon^3) \tag{B.9}$$

The expressions for the x-variable are similar. We now insert the expressions (B.8), (B.9) and their spatial equivalents in the equation of motion (B.7). This gives us a big expression, from which we extract the coefficients to the various powers of ε. We obtain:

$\mathcal{O}(\varepsilon)$

$$u^{(1)}_{t_0^2} - \alpha u^{(1)}_{x_0^2} + \beta u^{(1)} = 0 \tag{B.10}$$

On the basis of this we introduce the linear differential operator, $\mathcal{L}$:

$$\mathcal{L}\left\{\square\right\} = \frac{\partial^2 \square}{\partial t_0^2} - \alpha \frac{\partial^2 \square}{\partial x_0^2} + \beta \square \tag{B.11}$$

Using this we get for the next order of equations:

$\mathcal{O}(\varepsilon^2)$

$$\mathcal{L}\left\{u^{(2)}\right\} = 2\alpha u^{(1)}_{x_0 x_1} - 2u^{(1)}_{t_0 t_1} + 3(u^{(1)})^2 \tag{B.12}$$

$\mathcal{O}(\varepsilon^3)$

$$\begin{aligned} \mathcal{L}\left\{u^{(3)}\right\} = &-2u^{(2)}_{t_0 t_1} + 2\alpha u^{(2)}_{x_0 x_1} - u^{(1)}_{t_1^2} - 2u^{(1)}_{t_0 t_2} + \alpha u^{(1)}_{x_1^2} \\ &+2\alpha u^{(1)}_{x_0 x_2} - 6u^{(1)}u^{(2)} + \tfrac{7}{3}(u^{(1)})^3, \end{aligned} \tag{B.13}$$

where the subscripts denote differentiation. For the first order equation we seek *rotating wave* solutions, *i.e.,* solutions of the form

$$u^{(1)} = y^{(1)}\left(x_1, t_1; x_2, t_2\right) e^{i(qx_0 - \omega t_0)} + \mathbf{c.c.}, \tag{B.14}$$

where **c.c.** denotes complex conjugate terms. From this point on, the argument in the complex exponential function will be denoted θ_0, *i.e.,* $\theta_0 = (qx_0 - \omega t_0)$. This is inserted in (B.10) and we obtain

$$\left(-\omega^2 + \alpha q^2 + \beta\right) y e^{i\theta_0} + \mathbf{c.c.} = 0,$$

giving us the *dispersion relation*

$$\omega^2 = \alpha q^2 + \beta. \tag{B.15}$$

We note that this is a continuous dispersion relation, which is unbounded as opposed to the proper periodic discrete one. Thus, this approximation is only valid for small wavenumbers, where (B.15) approximates the discrete (which has a trigonometric shape). This is what can be extracted from the first order equation (B.10). From this we get the differentials

$$\begin{aligned} u^{(1)}_{t_0 t_1} &= -i\omega y_{t_1} e^{i\theta_0} + \mathbf{c.c.} \\ u^{(1)}_{x_0 x_1} &= iq y_{x_1} e^{i\theta_0} + \mathbf{c.c.} \end{aligned}$$

and the square of the function

$$\left(u^{(1)}\right)^2 = \left(y e^{i\theta_0} + y^* e^{-i\theta_0}\right)^2 = \ldots = y^2 e^{2i\theta_0} + |y|^2 + \mathbf{c.c.}$$

With this the second order equation (B.12) can be rewritten as:

$$\mathcal{L}\left\{u^{(2)}\right\} = 2i\omega y_{t_1}^{(1)} e^{i\theta_0} + 2i\alpha q y_{x_1}^{(1)} e^{i\theta_0} + 3\left(y^{(1)}\right)^2 e^{2i\theta_0} + 3|y^{(1)}|^2 + \mathbf{c.c.}. \tag{B.16}$$

We note that the left hand side is similar to (B.10) and thus the homogenous solution of (B.16) is of the form

$$u_{\text{Hom}}^{(2)} = y^{(2)} e^{i\theta_0} \tag{B.17}$$

From (B.16) we also detect secular terms (*i.e.,* terms proportional to $e^{i\theta_0}$, which appears in the first order solution) on the right hand side. We must eliminate these and thus demand that

$$\alpha q y_{x_1}^{(2)} + \omega y_{t_1}^{(1)} = 0 \iff y_{x_1} + v y_{t_1} = 0, \tag{B.18}$$

which is the linear wave equation, with $v \equiv \alpha\frac{q}{\omega}$. We therefore convert the problem to a moving frame of reference, *i.e.,* we consider

$$y^{(1)} \equiv \phi^{(1)}\left(\xi_1, \tau_1; x_2, t_2\right), \quad \xi_1 = x_1 - v t_1 \text{ and } \tau_1 = \varepsilon t_1. \tag{B.19}$$

Differentials with respect to the new coordinates are

$$\frac{\partial}{\partial x_1} = \frac{\partial}{\partial \xi_1}, \text{ and } \frac{\partial}{\partial t_1} = -v\frac{\partial}{\partial \xi_1} + \varepsilon\frac{\partial}{\partial \tau_1} \tag{B.20}$$

Note how the last term here comes into play in the next order equation. With (B.20) one can easily verify that Equation (B.18) is fulfilled to order ε. In these moving frame coordinates, the second order equation (B.16) now becomes

$$\mathcal{L}\left\{u^{(2)}\right\} = 3\left(\phi^{(1)}\right)^2 e^{2i\theta_0} + 3|\phi^{(1)}|^2 + 2i\omega\varepsilon\phi_{\tau_1}^{(1)} + \mathbf{c.c.} \tag{B.21}$$

We thus expect a particular solution to be of the form

$$u_{\text{Part}}^{(2)} = \lambda_1\left(\phi^{(1)}\right)^2 e^{2i\theta_0} + \lambda_2|\phi^{(1)}|^2 + \mathbf{c.c.} \tag{B.22}$$

Insertion in the $\mathcal{L}$-operator yields $\lambda_1 = -\frac{1}{\beta}$ and $\lambda_2 = \frac{3}{\beta}$. With the homogeneous solution (B.17), the full solution to the second order equation is

$$u^{(2)} = y^{(2)} e^{i\theta_0} - \frac{1}{\beta}\left(\phi^{(1)}\right)^2 e^{2i\theta_0} + \frac{3}{\beta}|\phi^{(1)}|^2 + \mathbf{c.c.} \tag{B.23}$$

We now turn to the third order equation (B.13). Again, we must eliminate secular terms, *i.e.,* terms proportional to $e^{i\theta_0}$, and from the nonlinear terms (the last two), we get the contributions (the calculations are straightforward, but rather long)

$$\begin{aligned} u^{(1)}u^{(2)}\big|_{\propto e^{i\theta_0}} &= \frac{5}{\beta}y^{(1)}|y^{(1)}|^2, \\ \left(u^{(1)}\right)^3\big|_{\propto e^{i\theta_0}} &= 3y^{(1)}|y^{(1)}|^2, \end{aligned}$$

where $\{\ \cdot\ \}|_{\propto e^{i\theta_0}}$ indicates that only terms proportional to $e^{i\theta_0}$ are included. From the first order solution we have the differentials (to order ε):

$$\begin{aligned} u^{(1)}_{t_1^2} &= y^{(1)}_{t_1^2} e^{i\theta_0} = v^2 \phi^{(1)}_{\xi_1^2} e^{i\theta_0} \\ u^{(1)}_{t_0 t_2} &= -i\omega y^{(1)}_{t_2} e^{i\theta_0} = \phi^{(1)}_{t_2} e^{i\theta_0} \\ u^{(1)}_{x_1^2} &= \phi^{(1)}_{\xi_1^2} e^{i\theta_0} \\ u^{(1)}_{x_0 x_2} &= iq y^{(1)}_{x_2} e^{i\theta_0} = iq\phi^{(1)}_{x_2} e^{i\theta_0} \end{aligned}$$

Inserting in the third order equation (B.13) we get:

$$\begin{aligned} \mathcal{L}\left\{u^{(3)}\right\} = \Big\{ & 2i\omega\phi^{(1)}_{\tau_1} + 2i\omega y^{(2)}_{t_1} + 2i\alpha q y^{(2)}_{x_1} - v^2\phi^{(1)}_{\xi_1^2} + 2i\omega\phi^{(1)}_{t_2} \\ & + \alpha\phi^{(1)}_{\xi_1^2} + 2i\alpha q\phi^{(1)}_{x_2} + \tfrac{30}{\beta}\phi^{(1)}|\phi^{(1)}|^2 + 7\phi^{(1)}|\phi^{(1)}|^2 \Big\} e^{i\theta_0} + \text{other terms} \end{aligned} \tag{B.24}$$

We now extend the frame of moving reference to also count the x_2 and t_2 variables (could also have been done at page 126), *i.e.,* we have

$$y^{(1)} \equiv \phi^{(1)}\left(\xi_1, \tau_1; \xi_2, \tau_2\right), \quad \xi_2 = x_2 - vt_2 \text{ and } \tau_2 = \varepsilon t_2. \tag{B.25}$$

With this, the terms of (B.24) proportional to $e^{i\theta_0}$ can be written

$$\begin{aligned} \mathcal{L}\left\{u^{(3)}\right\}\big|_{\propto e^{i\theta_0}} = {} & 2i\omega\phi^{(1)}_{\tau_1} + 2i\left[\omega y^{(2)}_{t_1} + \alpha q y^{(2)}_{x_1}\right] - v^2\phi^{(1)}_{\xi_1^2} + \alpha\phi^{(1)}_{\xi_1^2} \\ & + 2i\left[v\omega + \alpha q\right]\phi^{(1)}_{\xi_2} + \left(\tfrac{30}{\beta} + 7\right)\phi^{(1)}|\phi^{(1)}|^2 \end{aligned} \tag{B.26}$$

Here, the first square bracket cancels because of (B.18) and the second because $v = \alpha q/\omega$ – both are consequences of the moving frame of reference. Thus what remains is a version of the Nonlinear Schrödinger Equation (NLS)

$$\boxed{2i\omega\phi^{(1)}_{\tau_1} + \left(\alpha - v^2\right)\phi^{(1)}_{\xi_1^2} + \left(\tfrac{30}{\alpha} - 7\right)|\phi^{(1)}|^2\phi^{(1)} = 0.} \tag{B.27}$$

Solution of the Nonlinear Schrödinger Equation

In the prevous section we have established that the $\phi^{(1)}$-function only depends on the variables τ_1 and ξ_1. In this section write $u(x,t)$ instead of $\phi^{(1)}(\xi_1, \tau_1)$ for convenience. The solution of NLS is assumed to be of the breather-like[1] form

$$u(x,t) = A\text{sech}\left(B(x - vt)\right)e^{i(\gamma x - \Lambda t)} \tag{B.28}$$

Using the short hand notation $B(x - vt) = \psi$ and $\gamma x - \Lambda t = \phi$, differentiation of this solution gives

$$u_t = -iA\Lambda e^{i\phi}\text{sech}\psi + ABv\text{sech}\psi\tanh\psi e^{i\phi} \tag{B.29}$$

$$u_{xx} = -Ae^{i\phi}\text{sech}\psi\left\{B^2\text{sech}^2\psi + (\gamma + iB\tanh\psi)^2\right\} \tag{B.30}$$

[1] We notice that the form is not an exact breather, however, the solution exhibits the qualities we want. An exact breather would include all frequencies; here, as (B.36) will show, only 2 are included.

This inserted in (B.27) gives us the equation (using $\tanh^2 x = 1 - \mathrm{sech}^2 x$):

$$\begin{array}{c} 2\omega\Lambda + 2i\omega Bv \tanh\psi \\ -\left(\alpha - v^2\right)\left\{B^2\mathrm{sech}^2\psi + \gamma^2 + 2i\gamma B\tanh\psi - B^2\tanh^2\psi\right\} \\ +\left(\frac{30}{\beta} - 7\right)A^2\mathrm{sech}^2\psi = 0 \end{array} \tag{B.31}$$

We now collect the terms proportional to $\tanh\psi$, $\mathrm{sech}^2\psi$ and constant terms. We get

$$\begin{aligned} \left\{-2B^2\left(\alpha - v^2\right) + \left(\frac{30}{\alpha} - 7\right)A^2\right\}\mathrm{sech}^2\psi &= \\ \left\{2i\omega Bv - 2i\left(\alpha - v^2\right)\gamma B\right\}\tanh\psi &+ \\ \left(2\omega\Lambda - \left(\beta - v^2\right)\gamma^2 + gB^2\right) &= 0 \end{aligned} \tag{B.32}$$

Equation (B.32) gives us then the following (we note that A and B are only constants to the third order of ε, but this is sufficient here)

$$\gamma = \frac{\omega v}{(\alpha - v^2)} \tag{B.33}$$

$$B^2 = \gamma^2 - 2\frac{\omega\Lambda}{(\alpha - v^2)} \tag{B.34}$$

$$A^2 = \frac{2\left(\alpha - v^2\right)B^2}{\frac{30}{\beta} - 7} \tag{B.35}$$

In summary, we have now obtained a solution ansatz as (with A and B given as (B.35))-(B.34) and g and α as noted on page 124):

$$\begin{array}{c} u(x,t) = A\mathrm{sech}\left(B(x - vt)\right)e^{i(\gamma+q)x - i(\omega+\Lambda)t} + \frac{3}{\beta}A^2\mathrm{sech}^2\left(B(x - vt)\right) \\ -\frac{1}{\beta}A^2\mathrm{sech}^2(B(x - vt))\,e^{2i(\gamma+q)x - 2i(\omega+\Lambda)t} + \mathbf{c.c.} \end{array} \tag{B.36}$$

Extracting the real part of this solution gives us, for $t = 0$:

$$\begin{array}{c} u(x) = 2A\mathrm{sech}(Bx)\cos\left(\gamma + q\right)x + \frac{6}{\beta}A^2\mathrm{sech}^2(Bx) \\ -\frac{2}{\beta}A^2\mathrm{sech}^2(Bx)\cos 2(\gamma + q)x \end{array} \tag{B.37}$$

We see that A is the perturbating parameter, so this calculation is only valid for small A. The equations are easily rewritten into discrete form with $u(x,t) = u_n(t)$.

C

Derivation of temporal $\chi^{(2)}$-equations

The starting point in deriving the $\chi^{(2)}$equations is Maxwell's equations in the plane wave approximation (9.12), derived in Sec. 9

$$\frac{\partial^2 \mathbf{E}}{\partial z^2} - \frac{1}{c^2}\frac{\partial^2 \mathbf{E}}{\partial t^2} = 0 \tag{C.1}$$

Here, we do not consider any transverse spatial variation of the electric field. This means that, for the time being, we neglect the x and y variations of the Laplacian operator $\nabla^2 = \frac{\partial^2}{\partial x^2} + \frac{\partial^2}{\partial y^2} + \frac{\partial^2}{\partial z^2}$. We use the *Slowly Varying Envelope Approximation* (SVEA) in which the spectral width of the FW and SH are considered small compared to the spectral width of the wave numbers k_1 and k_2. These can then be approximated by a Taylor expansion. Furthermore, we consider only second order terms, namely

$$\begin{aligned} \mathbf{E} &\approx E_1 e^{ik_1(\omega_0)z - i\omega_0 t}\hat{\mathbf{e}}_\mathbf{1} + E_2 e^{ik_2(2\omega_0)z - 2i\omega_0 t}\hat{\mathbf{e}}_\mathbf{2} + E_1^* e^{-ik_1(\omega_0)z + i\omega_0 t}\hat{\mathbf{e}}_\mathbf{1}^* + E_2^* e^{-ik_2(2\omega_0)z + 2i\omega_0 t}\hat{\mathbf{e}}_\mathbf{2}^* \\ &= E_1 e^{ik_1(\omega_0)z - i\omega_0 t}\hat{\mathbf{e}}_\mathbf{1} + E_2 e^{ik_2(2\omega_0)z - 2i\omega_0 t}\hat{\mathbf{e}}_\mathbf{2} + \mathbf{c.c.}, \end{aligned} \tag{C.2}$$

where $\hat{\mathbf{e}}_\mathbf{j}$ is a unit vector describing the polarization of field component j and where we have introduced the notation **c.c.** for the complex conjugate and not explicitly written the dependencies of $E_j = E_j(z,t), j = 1, 2$, for brevity. Similarly, we have for $\mathbf{D}$

$$\mathbf{D}(z,t) \approx D_1(z,t)e^{ik_1(\omega_0)z - i\omega_0 t}\hat{\mathbf{e}}_\mathbf{1} + D_2(z,t)e^{ik_2(2\omega_0)z - 2i\omega_0 t}\hat{\mathbf{e}}_\mathbf{2} + \mathbf{c.c.}. \tag{C.3}$$

Now, the electric displacement may also be expressed ([3, 69, 51])

$$\mathbf{D} = \varepsilon_0 \mathbf{E} + \int_{-\infty}^{t} \chi^{(1)}(t-\tau_1)\cdot\mathbf{E}(\tau_1)\,d\tau_1 + \int_{-\infty}^{t}\int_{-\infty}^{t} \chi^{(2)}(t-\tau_1, t-\tau_2)\cdot\mathbf{E}(\tau_1)\,\mathbf{E}(\tau_2)\,d\tau_1 d\tau_2. \tag{C.4}$$

We have used integral representations of the polarization in (9.5), in which the $\chi^{(1)}$ term represents the material's linear contribution to the polarization, the $\chi^{(2)}$term the second order nonlinear contribution, and $\mathbf{E}$ is merely the vacuum contribution.

We note that $\chi^{(1)}$ and $\chi^{(2)}$ are *tensors* of second and third rank, respectively.

The integral representation in (C.4) emphasizes the delay in which a nonlinear medium responds to light. Because of the causal nature of such a response:

$$\chi(t-\tau) = 0 \quad \text{for} \quad t-\tau < 0,$$

we can safely allow the upper limits in the integrals of (C.4) to extend to infinity.

The next step is to describe $\mathbf{D}$ in terms of $\mathbf{E}$. We insert (C.2) and (C.3) in (C.4) and collect terms. The ones proportional to D_1 are the ones containing E_1 from the vacuum contribution, $\chi^{(1)}E_1$ from the linear polarization and $\chi^{(2)}D_1^*D_2 + \mathbf{c.c.} = 2\chi^{(2)}D_1^*D_2$ from the second order nonlinear contribution. If we define the vectorial Fourier transform of $\chi^{(1)}(t)$ at frequency ω_j as

$$\widetilde{\chi}_j^{(1)}(\omega) = \frac{1}{\varepsilon_0}\int_{-\infty}^{\infty}\left[\hat{e}_j^* \cdot \chi^{(1)}(t)\cdot\hat{e}_j\right]\exp\left(i\omega_j t\right)dt \tag{C.5}$$

with $j = 1, 2$ in both cases, and of $\chi^{(2)}(t,t')$ as

$$\widetilde{\chi}_1^{(2)}\left(\omega_a,\omega_b\right) = \int_{-\infty}^{\infty}\int_{-\infty}^{\infty}\left[\hat{e}_1^* \cdot \chi^{(2)}(t,t')\cdot\hat{e}_1^*\hat{e}_2\right]\exp\left(i\omega_a t + i\omega_b t'\right)dtdt', \tag{C.6}$$

$$\widetilde{\chi}_2^{(2)}\left(\omega_a,\omega_b\right) = \int_{-\infty}^{\infty}\int_{-\infty}^{\infty}\left[\hat{e}_2^* \cdot \chi^{(2)}(t,t')\cdot\hat{e}_1\hat{e}_1\right]\exp\left(i\omega_a t + i\omega_b t'\right)dtdt'. \tag{C.7}$$

The SVEA approximation allows us to expand Equations (C.5)-(C.7) in terms of their Taylor series:

$$\widetilde{\chi}_j^{(1)}(\omega) \approx \widetilde{\chi}_j^{(1)}(\omega_0) + \left.\frac{\partial\widetilde{\chi}_j^{(1)}(\omega)}{\partial\omega}\right|_{j\omega_0}(\omega - j\omega_0) + \frac{1}{2}\left.\frac{\partial^2\widetilde{\chi}_j^{(1)}(\omega)}{\partial\omega^2}\right|_{j\omega_0}(\omega - j\omega_0)^2 + \ldots \tag{C.8}$$

$$\widetilde{\chi}_1^{(2)}\left(2\omega,-\omega\right) \approx \widetilde{\chi}_1^{(2)}\left(2\omega_0,-\omega_0\right) + \ldots \tag{C.9}$$

$$\widetilde{\chi}_2^{(2)}\left(\omega,\omega\right) \approx \widetilde{\chi}_2^{(2)}\left(\omega_0,\omega_0\right) + \ldots, \tag{C.10}$$

where we have expanded the zeroth order term to second order in ω, but the second order term only to first order in ω.

When we have perfect phase matching, *i.e.,*

$$\Delta k = 2k_1\left(\omega_0\right) - k_2\left(2\omega_0\right), \tag{C.11}$$

we find

$$D_1(z,t) = \varepsilon_0 E_1(z,t) + \varepsilon_0\widetilde{\chi}_1^{(1)}(\omega_0)E_1(z,t) + 2\widetilde{\chi}_1^{(2)}\left(2\omega_0,-\omega_0\right)E_1^*(z,t)E_2(z,t)e^{-i\Delta kz}, \tag{C.12}$$

$$D_2(z,t) = \varepsilon_0 E_2(z,t) + \varepsilon_0\widetilde{\chi}_2^{(1)}(\omega_0)E_2(z,t) + 2\widetilde{\chi}_2^{(2)}\left(\omega_0,\omega_0\right)E_1^2(z,t)e^{i\Delta kz}, \tag{C.13}$$

which by the definition of the relative permittivity

$$\widetilde{\varepsilon}_j = 1 + \widetilde{\chi}_j^{(1)}\left(j\omega_0\right), \quad \widetilde{\varepsilon}_j' = \left.\frac{\partial\widetilde{\chi}_j^{(1)}}{\partial\omega}\right|_{j\omega_0} \quad \text{and} \quad \widetilde{\varepsilon}_j'' = \left.\frac{\partial^2\widetilde{\chi}_j^{(1)}}{\partial\omega^2}\right|_{j\omega_0}$$

and also to second order

$$\widetilde{\varepsilon}_1^{(2)} = \widetilde{\chi}_1^{(2)}\left(2\omega_0,-\omega_0\right) \quad \text{and} \quad \widetilde{\varepsilon}_2^{(2)} = \widetilde{\chi}_2^{(2)}\left(2\omega_0,-\omega_0\right),$$

ensures that (C.12)–(C.13) can be written

$$D_1(z,t) = \widetilde{\varepsilon}_1 E_1(z,t) + i\widetilde{\varepsilon}_1'\partial_t E_1(z,t) - \frac{1}{2}\widetilde{\varepsilon}_1''\partial_t^2 E_1(z,t) + 2\widetilde{\varepsilon}_1^{(2)} E_1^*(z,t)E_2(z,t)e^{-i\Delta kz}, \quad \text{(C.14)}$$

$$D_2(z,t) = \widetilde{\varepsilon}_2 E_2(z,t) + i\widetilde{\varepsilon}_2'\partial_t E_2(z,t) - \frac{1}{2}\widetilde{\varepsilon}_2''\partial_t^2 E_2(z,t) + \widetilde{\varepsilon}_2^{(2)} E_1^2(z,t)e^{i\Delta kz}. \quad \text{(C.15)}$$

At this point, we have expressed $D_{1,2}$ in terms of $E_{1,2}$, and we are ready to insert this in Eq. (C.1). We only retain terms of second order and get

$$\partial_z^2 \mathbf{E}_1 = \left(\partial_z^2 E_1 + 2ik_1\partial_z E_1 - k_1^2\right) e^{ik_1(\omega_0)z - i\omega_0 t} \quad \text{(C.16)}$$

$$\partial_t^2 \mathbf{D}_1 = \left(\partial_t^2 D_1 - 2i\omega_0\partial_t D_1 - \omega_0^2\right) e^{ik_1(\omega_0)z - i\omega_0 t} \quad \text{(C.17)}$$

With D_1 from Eq. (C.14), we get

$$\begin{aligned}\partial_t D_1 &\approx \widetilde{\varepsilon}_1\partial_t E_1 + i\widetilde{\varepsilon}_1'\partial_t^2 E_1 - \frac{1}{2}\widetilde{\varepsilon}_1''\partial_t^3 E_1 + 2\widetilde{\varepsilon}_1^{(2)}\left(E_2\partial_t E_1^* + E_1^*\partial_t E_2\right)e^{-i\Delta kz} \\ &\approx \widetilde{\varepsilon}_1\partial_t E_1 + i\widetilde{\varepsilon}_1'\partial_t^2 E_1 + \ldots \quad \text{(C.18)} \\ \partial_t^2 D_1 &\approx \widetilde{\varepsilon}_1\partial_t^2 E_1 + i\widetilde{\varepsilon}_1'\partial_t^3 E_1 - \frac{1}{2}\widetilde{\varepsilon}_1''\partial_t^4 E_1 + 2\widetilde{\varepsilon}_1^{(2)}\left(E_2\partial_t^2 E_1^* + 2\partial_t E_1^*\partial_t E_1 s^2 + E_1^*\partial_t^2 E_2\right)e^{-i\Delta kz} \\ &\approx \widetilde{\varepsilon}_1\partial_t^2 E_1 + \ldots, \quad \text{(C.19)}\end{aligned}$$

where higher order terms have been neglected. From the SVEA, we have the magnitude assumptions

$$\left|k_1^2 E_1\right| \gg \left|k_1\partial_z E_1\right| \gg \left|\partial_z^2 E_1\right| \quad \text{and} \quad \left|\omega_0^2 E_1\right| \gg \left|\omega_0\partial_t E_1\right| \gg \left|\partial_t^2 E_1\right|$$

Now, Eqs. (C.16)–(C.19) are inserted in (C.1), and we sort by orders of magnitude:

$$\begin{aligned}&\underbrace{-k_1^2 E_1 + \frac{\omega_0^2}{c^2}\widetilde{\varepsilon}_1 E_1}_{\bullet 1A} + \underbrace{2ik_1\partial_z E_1 + \left(i\frac{\omega_0^2}{c^2}\widetilde{\varepsilon}_1' + 2i\frac{\omega_0}{c^2}\widetilde{\varepsilon}_1\right)\partial_t E_1}_{\bullet 2A} + \\ &\underbrace{\partial_z^2 E_1 - \left(\frac{1}{2}\frac{\omega_0^2}{c^2}\widetilde{\varepsilon}_1'' + 2\frac{\omega_0}{c^2}\widetilde{\varepsilon}_1' + \frac{1}{c^2}\widetilde{\varepsilon}_1\right)\partial_t^2 E_1 + 2\frac{\omega_0^2}{c^2}\widetilde{\varepsilon}_1^{(2)} E_1^* E_2 e^{-i\Delta kz}}_{\bullet 3A} = 0.\end{aligned} \quad \text{(C.20)}$$

Here, the $\bullet 1A$-term indicates the dominant zeroth order term. Demanding this to be zero gives us a dispersion relation

$$k_1^2 + \frac{\omega_0^2}{c^2}\widetilde{\varepsilon}_1 = 0 \quad \text{(C.21)}$$

From this relation, we deduce the frequency derivatives of $k_1(\omega)$:

$$2k_1 dk_1 = \frac{1}{c^2}\left(d\left(\omega^2\right)\widetilde{\varepsilon}_1 + \omega^2 d\left(\widetilde{\varepsilon}_1\right)\right) = \frac{2\omega}{c^2}d\omega\ \widetilde{\varepsilon}_1 + \frac{\omega^2}{c^2}\widetilde{\varepsilon}_1' d\omega$$

so

$$k_1' = \left.\frac{dk_1}{d\omega}\right|_{\omega_0} = \frac{\omega_0^2}{2k_1c^2}\widetilde{\varepsilon}_1' + \frac{\omega_0}{k_1c^2}\widetilde{\varepsilon}_1. \quad \text{(C.22)}$$

For future use, we differentiate once more (straightforward, but somewhat tedious) to get

$$k_1'' = \left.\frac{d^2k_1}{d\omega^2}\right|_{\omega_0} = \frac{\omega_0^2}{2k_1c^2}\widetilde{\varepsilon}_1'' + \frac{2\omega_0}{k_1c^2}\widetilde{\varepsilon}_1' + \frac{1}{k_1c^2}\widetilde{\varepsilon}_1 - \frac{\left(k_1'\right)^2}{k_1}. \quad \text{(C.23)}$$

The next order of (C.20), $\bullet 2A$, is now conveniently rewritten using the first derivative of the dispersion relation (C.22)

$$i\partial_z E_1 + ik_1'\partial_t E_1 = 0, \tag{C.24}$$

which can be differentiated again to express the second order *spatial* derivative in terms of the second order *temporal* derivative as

$$\partial_z^2 E_1 = -k_1'\partial_t\left(-k_1'\partial_t E_1\right) = \left(k_1'\right)^2\partial_t^2 E_1 \tag{C.25}$$

This, in turn, is inserted in the second order term, $\bullet 3A$, of (C.20)

$$\left(\left(k_1'\right)^2 - \frac{\omega_0^2}{2c^2}\widetilde{\varepsilon}_1'' - \frac{2\omega_0}{c^2}\widetilde{\varepsilon}_1' - \frac{1}{c^2}\widetilde{\varepsilon}_1\right)\partial_t^2 E_1 + \frac{2\omega_0^2}{c^2}\widetilde{\varepsilon}_1^{(2)} E_1^* E_2 e^{-i\Delta k z}$$

With the constant

$$K_1 = \frac{\omega_0^2}{k_1 c^2}\widetilde{\varepsilon}_1^{(2)}, \tag{C.26}$$

and (C.23), we get

$$-\frac{1}{2}k_1''\partial_t^2 E_1 + K_1 E_1^* E_2 e^{-i\Delta k z} = 0. \tag{C.27}$$

This now gives us

$$\boxed{i\frac{\partial E_1}{\partial z} + ik_1'\frac{\partial E_1}{\partial t} - \frac{1}{2}k_1''\frac{\partial^2 E_1}{\partial t^2} + K_1 E_1^* E_2 e^{-i\Delta k z} = 0} \tag{C.28}$$

This is the equation for E_1 — a identical one exists for the complex conjugate, E_1^*, and a similar one is derived below for the SH field, E_2. Here, the derivatives (C.16)–(C.19) become, where we keep in mind that the SH wave number, k_2, is a function of the double frequency, $k_2 = k_2(2\omega)$.

$$\partial_z^2\mathbf{E}_2 = \left(\partial_z^2 E_2 + 2ik_2\partial_z E_2 - k_2^2\right)e^{ik_2(2\omega_0)z - 2i\omega_0 t}$$

$$\partial_t^2\mathbf{D}_2 = \left(\partial_t^2 D_2 - 4i\omega_0\partial_t D_1 - 4\omega_0^2\right)e^{ik_2(2\omega_0)z - 2i\omega_0 t}$$

With D_2 from Eq. (C.15) we get, analogously to (C.18)–(C.19)

$$\begin{aligned}\partial_t D_1 &= \widetilde{\varepsilon}_2\partial_t E_2 + i\widetilde{\varepsilon}_2'\partial_t^2 E_2 + \ldots\\ \partial_t^2 D_1 &= \widetilde{\varepsilon}_2\partial_t^2 E_2 + \ldots,\end{aligned}$$

We insert in (C.1) and sort by orders

$$\begin{aligned}&\underbrace{-k_2^2 E_2 + \frac{(2\omega_0)^2}{c^2}\widetilde{\varepsilon}_2 E_2}_{\bullet 1B} + \underbrace{2ik_2\partial_z E_2 + \left(i\frac{(2\omega_0)^2}{c^2}\widetilde{\varepsilon}_2 + 2i\frac{2\omega_0}{c^2}\widetilde{\varepsilon}_2'\right)\partial_t E_2}_{\bullet 2B} +\\ &\underbrace{\partial_z^2 E_2 - \left(\frac{1}{2}\frac{(2\omega_0)^2}{c^2}\widetilde{\varepsilon}_2'' + 2\frac{2\omega_0}{c^2}\widetilde{\varepsilon}_2' + \frac{1}{c^2}\widetilde{\varepsilon}_2\right)\partial_t^2 E_2 + \frac{(2\omega_0)^2}{c^2}\widetilde{\varepsilon}_2^{(2)} E_1^2 e^{i\Delta k z}}_{\bullet 3B} = 0.\end{aligned} \tag{C.29}$$

Again, the zeroth order term, $\bullet 1B$, gives us a dispersion relation

$$2k_2 dk_2 = \frac{1}{c^2}\left[d\left(2\omega^2\right)\widetilde{\varepsilon}_2 + (2\omega)^2 d\left(\widetilde{\varepsilon}_1\right)\right] = \frac{1}{c^2}\left[(2\omega)\widetilde{\varepsilon}_2 + \frac{1}{2}(2\omega)^2\widetilde{\varepsilon}_2'\right]d(2\omega)$$

so

$$k_2' = \frac{dk_2}{d(2\omega)} = \left.\frac{dk_2}{d(2\omega)}\right|_{2\omega_0} = \frac{(2\omega_0)^2}{2k_2c^2}\widetilde{\varepsilon}_2' + \frac{2\omega_0}{k_2c^2}\widetilde{\varepsilon}_2. \tag{C.30}$$

A second differentiation is also useful here, which gives

$$\frac{d^2k_2}{d\omega^2} = \ldots = \frac{1}{k_2^2c^2}\left[\left(\frac{1}{2}\omega^2\widetilde{\varepsilon}_2'' + 2\omega\widetilde{\varepsilon}_2' + \widetilde{\varepsilon}_2\right)k_2 - \left(\frac{1}{2}\frac{(\omega)^2}{2k_2c^2}\widetilde{\varepsilon}_2' + \frac{\omega}{k_2c^2}\widetilde{\varepsilon}_2\right)\right].$$

With $\omega = 2\omega_0$, we get

$$k_2'' = \frac{d^2k_2}{d(\omega)^2} = \left.\frac{d^2k_2}{d(2\omega)^2}\right|_{2\omega_0} = \frac{(2\omega)}{2k_2c^2}\widetilde{\varepsilon}_2'' + 2\frac{2\omega_0}{k_2c^2}\widetilde{\varepsilon}_2' + \frac{1}{k_2c^2}\widetilde{\varepsilon}_2 - \frac{(k_2')^2}{k_1}. \tag{C.31}$$

As for the D_1 equation, the first order term of (C.29) gives us apart from the contribution to the differential equation

$$i\partial_z E_2 + ik_2'\partial_t E_2 = 0, \tag{C.32}$$

also the relationship

$$\partial_z^2 E_2 = \left(k_2'\right)^2 \partial_t^2 E_2. \tag{C.33}$$

This, in turn, is inserted in the second order term, $\bullet 3B$, of (C.29), and with the constant

$$K_2 = \frac{2\omega_0^2}{k_2c^2}\widetilde{\varepsilon}_2^{(2)}, \tag{C.34}$$

and (C.31), the second order term becomes

$$-k_2''\partial_t^2 E_2 + K_2E_1^2e^{i\Delta kz} = 0. \tag{C.35}$$

Finally, the SH equation from the Maxwell equation (C.1) is

$$\boxed{i\frac{\partial E_2}{\partial z} + ik_2'\frac{\partial E_2}{\partial t} - \frac{1}{2}k_2''\frac{\partial^2 E_2}{\partial t^2} + K_2E_2e^{i\Delta kz} = 0} \tag{C.36}$$

We see that by introducing the scalings

$$\xi = |k_1''|z, \quad s = t - k_1',$$

we get $\partial_z = |k_1''|\partial_\xi - k_1'\partial_s$ and $\partial_t = \partial_s$, which eliminates the s-differentiations in (C.28) and with the constants

$$\delta = \frac{k_1' - k_2'}{|k_1''|}, \quad \alpha = \frac{k_2''}{|k_1''|}, \quad \beta = \frac{\Delta k}{|k_1''|}, \quad a_1 = \frac{\sqrt{|K_1K_2|}}{|k_1''|}A_1, \quad \text{and} \quad a_2 = \frac{K_1}{|k_1''|}A_2,$$

we arrive at the normalized equations for quadratic nonlinear materials

$$\boxed{i\frac{\partial a_1}{\partial \xi} - \frac{r}{2}\frac{\partial^2 a_1}{\partial s^2} + {a_1}^*a_2e^{-i\beta\xi} = 0} \tag{C.37}$$

$$\boxed{i\frac{\partial a_2}{\partial \xi} - i\delta\frac{\partial a_2}{\partial s} - \frac{\alpha}{2}\frac{\partial^2 a_2}{\partial s^2} + a_1^2e^{i\beta\xi} = 0.} \tag{C.38}$$

Then, by changing the ξ-variable to z, s to t, and the a_j to the corresponding E_j's and denote $-r/2$ by $2d_1$ and $-\alpha/2$ by d_2, we get the temporal $\chi^{(2)}$-equations. In this work, however, we do not consider any first derivative of the spatial variable, so δ from (C.38) is zero. Instead, we include a transverse spatial variation, which can be deduced in a similar way (see [50, 51] for details) and we arrive at the equations (9.29)–(9.30).

D
The Fourier Split Step Method

The Fourier Split-Step (FSS) method is convenient numerical tool for solving the Nonlinear Schrödinger Equation (NLS) or related equations, such as (D.1)–(D.2)

$$i\partial_z E_1 + d_1 \partial_x^2 E_1 + \beta^{-1} N\left(E_1{}^2\right) E_1{}^* = 0, \tag{D.1}$$

$$N\left(E_1{}^2\right) = \int_{-\infty}^{\infty} R\left(x-\xi\right) E_1{}^2\left(\xi, z\right) d\xi. \tag{D.2}$$

Naïve FSS

The idea is that under the assumption $\Delta z \ll 1$, we can consider the linear and nonlinear parts of the equation independent of each other, as their interaction is assumed negligible for this small Δz. More formally, we consider Equations (D.1)–(D.2) as

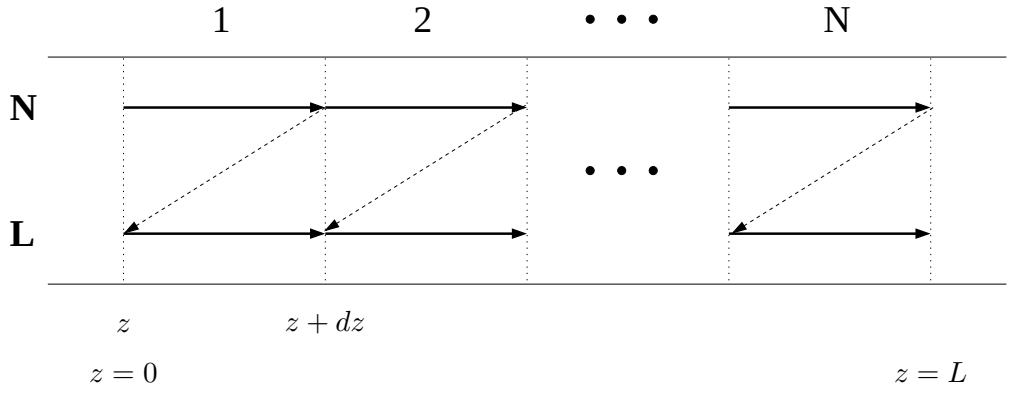

Figure D.1: *The normal FSS scheme.*

$$\partial_z E_1 = \left(\hat{L} + \hat{N}\right) E_1, \tag{D.3}$$

where the operators

$$\hat{L} = i d_1 \frac{\partial^2 \square}{\partial x^2} \tag{D.4}$$

and

$$\hat{N} = i\beta^{-1} N\left(\Box^2\right)\Box^* \tag{D.5}$$

accounts for the linear and nonlinear parts, respectively. With this notation, we first solve the linear part of (D.3) by using $\hat{N} = 0$, and then use $\hat{L} = 0$ to solve the nonlinear part.

A first observation is that assuming the operators $\hat{L}$ and $\hat{N}$ are constant for a small Δz, (D.3) solves to $E_1(z) = e^{\left(\hat{L}+\hat{N}\right)z}$ (disregarding the other variable x for now...). Thus we have

$$E_1(z+\Delta z) = e^{\left(\hat{L}+\hat{N}\right)(z+\Delta z)} = e^{\left(\hat{L}+\hat{N}\right)\Delta z} E_1(z) \tag{D.6}$$

The evaluation of an "exponential operator" $e^{\hat{M}\Delta z}$ can be evaluated by use of the series

$$e^{\hat{M}} = 1 + \hat{M} + \frac{1}{2}\hat{M}^2 + \ldots,$$

keeping in mind that operators need not commute. Thus, we can express the exponential operator in (D.6) to second order accuracy as

$$\begin{aligned} e^{\left(\hat{L}+\hat{N}\right)\Delta z} &= 1 + \Delta z\left(\hat{L}+\hat{N}+\right) + \frac{1}{2}\Delta z^2\left(\hat{L}+\hat{N}\right)^2 + \ldots \\ &= 1 + \Delta z\left(\hat{L}+\hat{N}\right) + \frac{1}{2}\Delta z^2\left(\hat{L}^2 + \hat{L}\hat{N} + \hat{N}\hat{L} + \hat{N}^2\right) + \ldots \end{aligned} \tag{D.7}$$

The FSS, however, approximates this as

$$e^{\hat{L}\Delta z} \cdot e^{\hat{N}\Delta z},$$

which evaluates to

$$\begin{aligned} e^{\Delta z\hat{L}} \cdot e^{\Delta z\hat{N}} &= \left(1 + \Delta z\hat{L} + \frac{1}{2}\Delta z^2\hat{L}^2 + \ldots\right)\cdot\left(1 + \Delta z\hat{N} + \frac{1}{2}\Delta z^2\hat{N}^2 + \ldots\right) \\ &= 1 + \Delta z\hat{N} + \frac{1}{2}\Delta z^2\hat{N}^2 + \ldots + \Delta z\hat{L} + \Delta z^2\hat{L}\hat{N} + \ldots + \frac{1}{2}\Delta z^2\hat{L}^2 + \ldots + \frac{1}{2}\Delta z^2\hat{L}^2 + \ldots \\ &= 1 + \Delta z\left(\hat{L}+\hat{N}\right) + \frac{1}{2}\Delta z^2\left(\hat{L}^2 + 2\hat{L}\hat{N} + \hat{N}^2\right) + \ldots \end{aligned} \tag{D.8}$$

Therefore, the FSS in this formulation is accurate to second order, as the difference between (D.7) and (D.8) is

$$\frac{1}{2}\Delta z^2\left(\hat{L}\hat{N} + \hat{N}\hat{L}\right) - \Delta z^2\hat{N}\hat{L} = \frac{1}{2}\Delta z^2\left[\hat{N},\hat{L}\right] + \mathcal{O}(\Delta z^3)$$

Improved FSS

It turns out that a minor correction to the method improves the accuracy by an order of magnitude! The idea is to split the nonlinear step at $z = \Delta z/2$, compute the linear step throughout the interval to $z = \Delta z$, and return to compute the remainder of the nonlinear part the $z = \Delta z$. The procedure is sketched in Fig. D.2. In this case, the exponential operator becomes to second order

$$\begin{aligned} e^{\left(\frac{1}{2}\hat{N}+\hat{L}+\frac{1}{2}\hat{N}\right)\Delta z} &= 1 + \Delta z\left(\frac{1}{2}\hat{N} + \hat{L} + \frac{1}{2}\hat{N}\right) + \frac{1}{2}\Delta z^2\left(\frac{1}{2}\hat{N} + \hat{L} + \frac{1}{2}\hat{N}\right)^2 + \ldots \\ &= 1 + \Delta z\left(\frac{1}{2}\hat{N} + \hat{L} + \frac{1}{2}\hat{N}\right) + \frac{1}{2}\Delta z^2\left(\frac{1}{4}\hat{N}^2 + \hat{L}^2 + \frac{1}{4}\hat{N}^2 + \hat{N}\hat{L} + \hat{L}\hat{N} + \frac{2}{4}\hat{N}^2\right) + \ldots \\ &= 1 + \Delta z\left(\frac{1}{2}\hat{N} + \hat{L} + \frac{1}{2}\hat{N}\right) + \frac{1}{2}\Delta z^2\left(\hat{N}^2 + \hat{L}^2 + \hat{N}\hat{L} + \hat{L}\hat{N}\right) + \ldots \end{aligned} \tag{D.9}$$

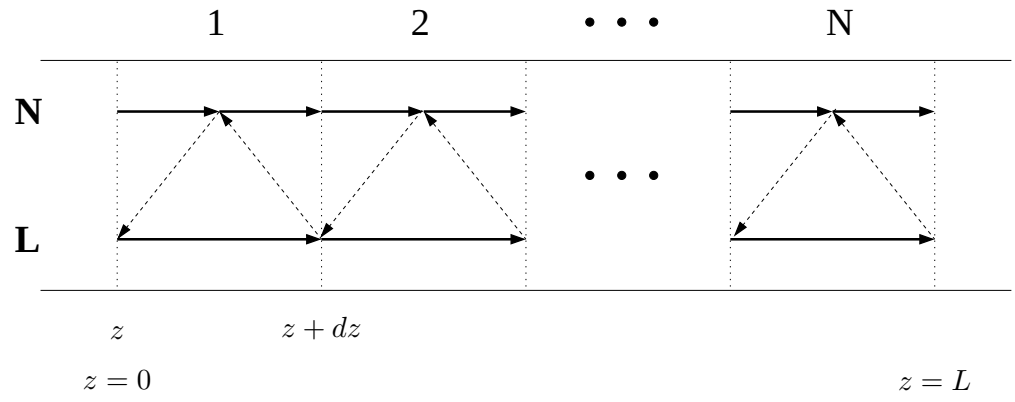

Figure D.2: *The modified FSS scheme.*

As before, we compare this to the accuracy of the numerical scheme, which in this formulation is

$$\begin{aligned} e^{\frac{1}{2}\hat{N}\Delta z}\cdot e^{\hat{L}\Delta z}\cdot e^{\frac{1}{2}\hat{N}\Delta z} &= \left[1+\Delta z\frac{1}{2}\hat{N}+\frac{1}{2}\Delta z^2\left(\frac{1}{2}\hat{N}\right)^2+\ldots\right]\cdot \\ &\quad \left[1+\Delta z\hat{L}+\frac{1}{2}\Delta z^2\hat{L}^2+\ldots\right]\cdot \\ &\quad \left[1+\Delta z\frac{1}{2}\hat{N}+\frac{1}{2}\Delta z^2\left(\frac{1}{2}\hat{N}\right)^2+\ldots\right] \\ &= 1+\frac{1}{2}\Delta z\hat{N}+\frac{1}{8}\Delta z^2\hat{N}^2+\Delta z\hat{L}+\frac{1}{2}\Delta z^2\hat{L}\hat{N}+\frac{1}{2}\Delta z^2\hat{L}^2+ \\ &\quad \frac{1}{2}\Delta z\hat{N}+\frac{1}{4}\Delta z^2\hat{N}^2+\frac{1}{2}\Delta z^2\hat{N}\hat{L}+\frac{1}{8}\Delta z^2\hat{N}^2+\ldots \\ &= 1+\Delta z\left(\hat{N}+\hat{L}\right)+\frac{1}{2}\Delta z^2\left(\hat{L}^2+\hat{L}\hat{N}+\hat{N}\hat{L}+\hat{N}^2\right)+\ldots \end{aligned} \quad \text{(D.10)}$$

Comparing Eqs. (D.9) and (D.10), we see that they are identical to second order; thus the error is at most of the order $\mathcal{O}(\Delta z^3)$ over each Δz-unit. The order of the operators is not important, one could just as well let the linear parts split in "half size steps".

We note that the calculations are most conveniently carried out if one recognizes the possibility of allowing 2 consecutive "half size steps" be computed as one step over the length Δz. In this way, corrections are only necessary at the ends of the z-interval, and the name *split step* is justified. This is depicted in Fig. D.3.

Evaluation of the operators

The linear operator $\hat{L}$

The linear part of the $\chi^{(2)}$ equations (D.1)

$$i\partial_z E_1 + d_1\partial_x^2 E_1 = 0 \quad \text{(D.11)}$$

is easy to solve through a Fourier transform on the x-variable. With the Fourier Transform (FT) pair

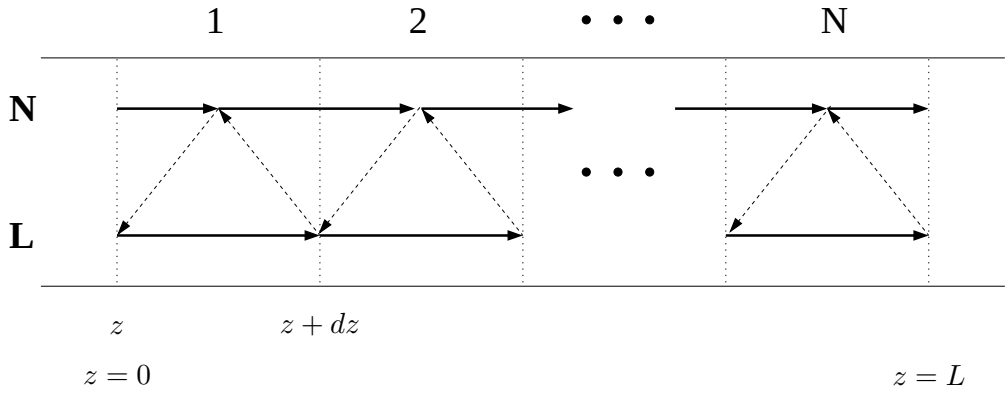

Figure D.3: *The modified FSS scheme with improved stepping.*

Fourier Transform (FT)

$$\mathcal{F}\left\{E_1\left(x,z\right)\right\} = \widetilde{E_1}\left(k,z\right) = \int_{-\infty}^{\infty} E_1\left(x,z\right) e^{-ikx} dx \tag{D.12}$$

Inverse Fourier Transform (IFT)

$$\mathcal{F}^{-1}\left\{\widetilde{E_1}\left(k,z\right)\right\} = E_1\left(x,z\right) = \frac{1}{2\pi}\int_{-\infty}^{\infty} \widetilde{E_1}\left(k,z\right) e^{ikx} dk. \tag{D.13}$$

We note that the tilde ($\widetilde{\ }$) indicates Fourier domain. The FT of a derivative transforms to the factor ik, thus (D.11) transforms to

$$i\partial_z \widetilde{E_1}\left(k,z\right) - \left(ik\right)^2 d_1 \widetilde{E_1} = 0 \quad \Longleftrightarrow \quad \partial_z \widetilde{E_1}\left(k,z\right) = -ik^2 d_1 \widetilde{E_1}, \tag{D.14}$$

which solves to

$$\widetilde{E_1}\left(k,z\right) = A\left(k\right) \cdot e^{-ik^2 d_1 z}. \tag{D.15}$$

In the Fourier domain, the value at the next z-grid point is easily evaluated as

$$\widetilde{E_1}\left(k, z+\Delta z\right) = A\left(k\right) \cdot e^{-ik^2 d_1 z + \Delta z} = \widetilde{E_1}\left(k,z\right) \cdot e^{-ik^2 d_1 \Delta z}, \tag{D.16}$$

which is used in the simulation routines. Finally, an IFT is performed on (D.16) to obtain the result for the linear step.

The nonlinear operator $\hat{N}$

The nonlinear part of the $\chi^{(2)}$ equations (D.1)

$$i\partial_z E_1 + \beta^{-1} N\left({E_1}^2\right) {E_1}^* = 0, \tag{D.17}$$

with

$$N\left({E_1}^2\right) = \int_{-\infty}^{\infty} R\left(x-\xi\right) {E_1}^2\left(\xi,z\right) d\xi \tag{D.18}$$

cannot be solved analytically, but we also employ the FT to obtain a solution.

The Convolution Theorem

Equation (D.18) is an example of a *convolution integral*, which is easily evaluated through FT. This becomes apparent by considering the integral

$$f(x) = \int_{-\infty}^{\infty} g(x-y)h(y)dy \tag{D.19}$$

The FT of this is

$$\begin{aligned} \mathcal{F}\{f(x)\} = \widetilde{f}(k) &= \int_{x=-\infty}^{\infty}\int_{y=-\infty}^{\infty} g(x-y)h(y)e^{-ikx}dydx \\ &= \int_{\xi=-\infty}^{\infty}\int_{\gamma=-\infty}^{\infty} g(\xi)h(\gamma)e^{-ik(\xi+\gamma)}d\gamma d\xi, \end{aligned} \tag{D.20}$$

where the last equality comes from the change of variables $y = \gamma$ and $x = \xi + \gamma$. By separating the variables, one obtains

$$\begin{aligned} \mathcal{F}\{f(x)\} &= \int_{-\infty}^{\infty} g(\xi)e^{-ik\xi}d\xi \cdot \int_{-\infty}^{\infty} h(\gamma)e^{-ik\gamma}d\gamma \\ &= \mathcal{F}\{g(\xi)\} \cdot \mathcal{F}\{h(\gamma)\} \end{aligned} \tag{D.21}$$

This property enables us to solve Equation (D.17) easier by the use of the convolution theorem.

Spectral resolution

A note on the resolution of the initial condition is necessary. One must always be cautious when using Fourier transforms, because a change of the size of the computational grid in, e.g., real space changes the resolution in the spectral domain. Furthermore, we want to eliminate boundary effects as much as possible, because we are using periodic boundary conditions (which is easiest for the FSS method).

As an example, consider the Gaussian function $f(x) = e^{-(x/B)^2}$ (our initial condition (10.2) with $A = 1$ and for $t = 0$) on the domain $L_x/2 \leq x \leq L_x/2$, see Fig. D.4. Looking for a boundary value of 10^{-n}, we solve

$$e^{-(x/B)^2} \leq 10^{-n} \iff x_0 \geq \frac{L_x}{2} = B\sqrt{n\ \ln 10}. \tag{D.22}$$

Eq. (D.22) gives us thus a way to evaluate the spatial domain needed to obtain a given accuracy at a given initial condition at the boundary. Thus, with a initial pulse beam width of $B = 3$ and a boundary value of less than 10^{-6}, one needs a domain of

$$L_x = 2 \times 3 \times \sqrt{6\ \ln 10} \approx 22.3$$

Including the t variable in this derivation, one could switch to polar coordinates and find the same result for the radius. Thus, we can safely expand this bound on the spatial domain, L_x, to the temporal one, L_t, as well.

The Fourier transform of this initial condition is

$$\widetilde{f}\,(k,\omega) = \int_{-\infty}^{\infty}\int_{-\infty}^{\infty} e^{-(x/B)^2}e^{-(t/B)^2}e^{-ikx-i\omega t}dxdt,$$

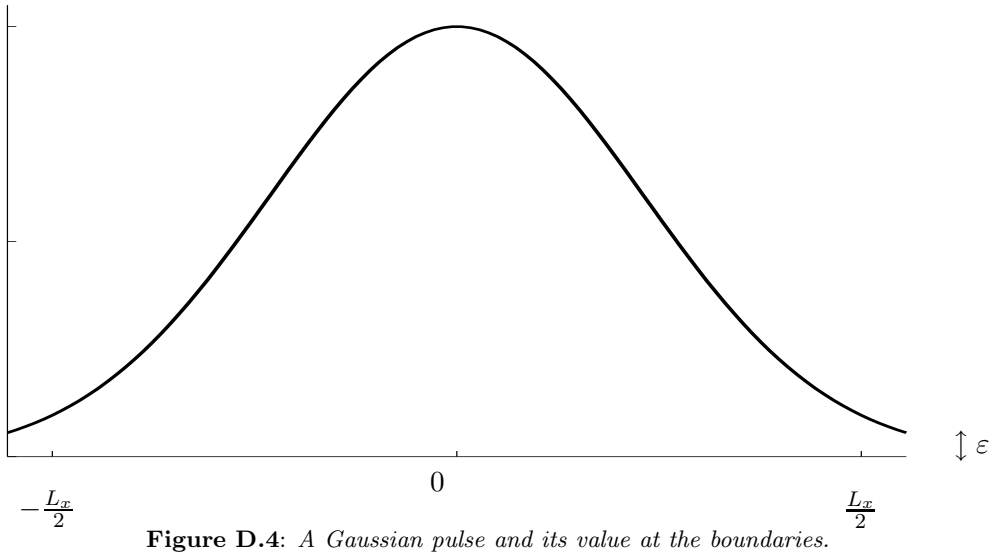

Figure D.4: *A Gaussian pulse and its value at the boundaries.*

which solves to

$$\widetilde{f}\,(k,\omega) = 4\left[\int_0^\infty e^{-(x/B)^2}\cos(kx)\,dx\right]^2 = B\sqrt{\pi}e^{-\frac{1}{2}B^2k^2},$$

since we have [57, 3.896.4]

$$\int_0^\infty e^{-\beta x^2}\cos(bx)\,dx = \frac{1}{2}\sqrt{\frac{\pi}{\beta}}\exp\left(-\frac{b^2}{4\beta}\right).$$

Disregarding the coefficient in front, we find in analogy with (D.22)

$$e^{-\frac{1}{2}B^2k_0^2} \le 10^{-m} \iff k_0 \ge \frac{L_k}{2} = \frac{1}{B}\sqrt{2\ m\ \ln 10}. \tag{D.23}$$

In the same way as before, with a initial pulse beam width of $B = 3$ and a boundary value of less than 10^{-6}, one needs a spectral domain of

$$L_k = \frac{2}{3}\times\sqrt{2\times 6\ \ln 10} \approx 3.5$$

Discrete Fourier Transform parameters

We can only do simulations on a *finite* grid, so we need to employ the *Discrete* Fourier Transform[1]. The difficulty with the discrete version of Fourier transform is that only one of the parameters L_x or L_k from Section D can be chosen independently and the other is then determined by the former.

With N discretization points, we have the relations

$$\Delta x = \frac{L_x}{N} \quad \text{and} \quad L_k = \frac{2\pi}{\Delta x} \tag{D.24}$$

and

$$\Delta k = \frac{L_k}{N} \quad \text{and} \quad L_x = \frac{2\pi}{\Delta k}. \tag{D.25}$$

[1]Actually, an efficient routine known as the *Fast Fourier Transform*, FFT, is used.

N	L_x	Δx	Δk	L_k
256	50	0.1953	0.1257	32.2
360	100	0.2778	0.0628	22.6

Table D.1: *Some accuracy parameters for some common computational values. N and L_x are user defined and Δx, Δk, and L_k computed from the relations (D.24)–(D.25).*

Rearranging (D.24) we find

$$L_k = N\frac{2\pi}{L_x},$$

so we see that expanding for instance L_x, causes L_k to narrow for the same number of discretization points, N. In conclusion, one needs to be aware of the real and spectral resolutions and domains. A small table for some of the parameter values used in the simulations are given in Table D.1. The values given here should be compared to the width of the initial condition, which need to be properly discretized. Typically, we use $B = 3$. The accuracy for the boundary condition, derived in both the real and the spectral domain from (D.22) and (D.23) to

$$n = \left(\frac{L_x}{2B}\right)^2 \frac{1}{\ln 10} \quad \text{and} \quad m = \left(\frac{\pi BN}{L_x}\right)^2 \frac{1}{2\ln 10}$$

evaluates to give boundary values smaller than 10^{-30} for the initial input beam profile. This is not a very important parameter; it is much more interesting to make sure the boundary values remain small throughout the simulations. For the simulations presented in this Thesis, these values are always less than 10^{-12}.